UNIVERSITI TEKNOLOGI MARA

FABRICATION OF AMORPHOUS CARBON THIN FILMS DEPOSITED FROM OYSTER MUSHROOM WASTE EXTRACT USING CHEMICAL VAPOR DEPOSITION (CVD) TECHNIQUE

AMIRAH RADHIANIE BINTI RINING

MSc

June 2026

UNIVERSITI TEKNOLOGI MARA

FABRICATIONS OF AMORPHOUS CARBON THIN FILMS DEPOSITED FROM OYSTER MUSHROOM WASTE EXTRACT USING CHEMICAL VAPOR DEPOSITION (CVD) TECHNIQUE

AMIRAH RADHIANIE BINTI RINING

Thesis submitted in fullfillment
of the requirements for the degree of
Master of Science
(Electrical Engineering)

Faculty of Electrical Engineering

June 2026

CONFIRMATION BY PANEL OF EXAMINERS

I certify that a Panel of Examiners has met on 17 December 2025 to conduct the final examination of Amirah Radhianie Binti Rining on her Masters of Science thesis entitled "Fabrication of Amorphous Carbon Thin Films Deposited from Oyster Mushroom Waste Extract using Chemical Vapor Deposition (CVD) Technique" in accordance with Universiti Teknologi MARA Act 1976 (Akta 173). The Panel of Examiners recommends that the student be awarded the relevant degree. The Panel of Examiners was as follows:

Mohd Hezri Fazalul Rahiman, PhD
Associate Professor
Faculty of Electrical Engineering
Universiti Teknologi MARA
(Chairman)

Sukreen Hana Herman, PhD
Associate Professor
Faculty of Electrical Engineering
Universiti Teknologi MARA
(Internal Examiner)

Zul Ilham Zulkiflee Lubes, PhD
Associate Professor
Faculty of Sciences
Universiti Malaya
(External Examiner)

PROFESSOR DR HJH ZURAEDA IBRAHIM
Dean
Institute of Postgraduates Studies
Universiti Teknologi MARA

Date: 30 June 2026

AUTHOR'S DECLARATION

I declare that the work in this thesis was carried out in accordance with the regulations of Universiti Teknologi MARA. It is original and is the results of my own work, unless otherwise indicated or acknowledged as referenced work. This thesis has not been submitted to any other academic institution or non-academic institution for any degree or qualification.

I, hereby, acknowledge that I have been supplied with the Academic Rules and Regulations for Postgraduate, Universiti Teknologi MARA, regulating the conduct of my study and research.

Name of Student	:	Amirah Radhianie Binti Rining
Student ID. No.	:	2023610758
Programme	:	Master of Science (Electrical Engineering) – CEEE750
Faculty	:	Electrical Engineering
Thesis Title	:	Fabrication of Amorphous Carbon Thin Films Deposited from Oyster Mushroom Waste Extract using Chemical Vapor Deposition (CVD) Technique
Signature of Student	:	……
Date	:	June 2026

ABSTRACT

Amorphous carbon (a-C) gained the researchers' attention due to its unique properties that give a lot of benefits in various fields, especially in electronic devices. Nowadays, the production of a-C thin films has evolved from using the traditionally toxic and explosive carbon precursor to renewable and environmentally friendly precursors, such as palm oil, camphor oil, palmyra sugar, and coconut sap. The fabrication of a-C thin films from a novel oyster mushroom waste extract was performed using the Chemical Vapor Deposition (CVD) technique. The extract of the waste-derived base component of oyster mushrooms was used as the carbon precursor to synthesize a-C, while n-type and p-type silicon served as the substrate. In the initial phase, Soxhlet extraction was performed with n-hexane and ethanol as solvents, followed by characterization of the mushroom waste extract through Thermogravimetric (TGA) and CHNS analysis was carried out. Findings indicate that n-hexane is a more advantageous solvent due to its higher carbon percentage, 70.387%. The ideal decomposition temperature, determined by TGA, is established at 350°C. The next phase involved the deposition of undoped a-C and nitrogen-doped a-C (a-CN) thin films using CVD with different parameters, including the amount of precursor, the deposition temperatures, and the gas flow rate, which affect the properties of a-C thin films. The main objective of this research is to determine the structural and electrical characteristics of the undoped a-C and a-CN. Characterization was done using the UV-Vis Spectroscopy for the optical properties, Raman Spectroscopy, Scanning Electron Microscope (SEM), and Energy Dispersive X-Ray Spectroscopy (EDX) for the structural properties, and Current-Voltage (I-V) Measurement for the electrical properties. The optimum parameters for undoped a-C and a-CN thin films have been identified. Throughout this research, undoped a-C thin films deposited with 2 ml oyster mushroom waste extract at 850°C and 40 sccm, while maintaining a precursor temperature of 350°C and a deposition time of 30 minutes, were found to offer the best electrical properties, achieving a conductivity value of 1.66×10^2 S.cm^{-1}. In contrast, the a-CN thin films that were synthesized at 850°C and 35 sccm are considered the best parameters to obtain an optimum result in electrical properties, with the value of 1.73×10^2 S.cm^{-1}. The findings indicate an enhancement in the electrical conductivity with the introduction of nitrogen dopant into the films. This research presents an excellent opportunity to showcase a new 'green' alternative precursor to produce a-C, along with potential as a material for electronic devices.

ACKNOWLEDGEMENT

Alhamdulillah, all praises to Allah for the strengths and His blessings in completing this thesis

First and foremost, I would like to sincerely thank my main supervisor, Ir. Dr. Nurfadzilah Ahmad, and my co-supervisor, Assoc. Prof. Ts. Dr. Wan Abd Al-Qadr Imad Bin Wan Mohtar for their supervision, guidance, patience, and support. Their guidance helped me throughout the time of research and writing of this thesis. I could not imagine having a better supervisor, advisor, and mentor for my Master's study.

Secondly, I would like to express my appreciation to the staff of Solar Research Institute (SRI), the staff of NANO-ElecTronic Centre (UiTM), and the staff of Omics Lab (UM), especially Mr. Suhaimi, Mr. Norsam, Mr. Asrul, Ms. Fakhirah, and Ms. Asyiqin, for their technical help and support.

A lot of thanks to my senior lab mates, Mrs. Syahirah, Dr. Robaiah, Dr. Dayana, Mrs. Syafiqah, Mr. Danial 'Aizat, Mr. Muthukumaaran, Mrs. Hana, my fellow lab mate, Ms. Alfarina, and my friend, Ain Nadhira, for their friendship, patience, support, and memories.

Last but not least, my deepest gratitude to all my family members. I would like to thank my parents, Mr. Rining Tambaku and for their endless love and support. Their encouragement and doa are my main motivation to keep on going and never give up.

TABLE OF CONTENTS

LIST OF TABLES

LIST OF FIGURES

LIST OF ABBREVIATIONS

Abbreviations

a-C	Amorphous Carbon
a-CN	Nitrogen-Doped Amorphous Carbon
CVD	Chemical Vapor Deposition
CHNS	Carbon, Hydrogen, Nitrogen, and Sulphur
TGA	Thermogravimetric Analyzer
CNT	Carbon Nanotubes
DAC	Diamond-Like Amorphous Carbon
DLC	Diamond-Like Carbon
PLA	Pulsed Laser Ablation
CVA	Cathodic Vacuum Arc
GaAS	Gallium Arsenide
InP	Indium Phosphide
RF-PECVD	Radio Frequency Plasma-Enhanced Chemical Vapor Deposition
WMB	Waste Mushroom Biomass
FBB	Fruiting Body Base
HCl	Hydrochloric Acid
SEM	Scanning Electron Microscope
EDX	Energy Dispersive X-Ray Spectroscopy

CHAPTER 1
INTRODUCTION

1.1 Research Background

Carbon-based materials are increasingly impacting nearly every field, including engineering, biology, chemistry, physics, computer sciences, and material sciences (Choudhary et al., 2024). Over the past few decades, 2D carbon-based materials, especially graphene, have drawn a lot of attention because of their remarkable optical, mechanical, and electronic characteristics, making them highly demanded for the development of electronic devices (Dos Santos et al., 2025; Kim et al., 2021). The discovery of graphene has sparked interest in finding other carbon allotropes, such as fullerenes, graphene, diamond, carbon nanotubes, and amorphous carbon (a-C), with the goal of uncovering novel properties through modifications to the carbon lattice (Dhameliya et al., 2024; Kim et al., 2021; Kothandam et al., 2023; Saputri et al., 2020). Among these, pure and doped a-C has appeared as a promising option due to its distinctive properties that are advantageous across various sectors, particularly in electronics.

Amorphous carbon features a disordered atomic arrangement lacking long-range crystallinity, consisting mainly of a mixture of sp^2 (graphitic) and sp^3 (diamond-like) bonded carbon atoms (Bharadia et al., 2024; Etula et al., 2021; Priyanto et al., 2024). The alterations in the sp^2/sp^3 bonding ratio significantly affects the physical, chemical, electrical, and optical characteristics of the films (Chen et al., 2015). The interplay between these bonding types grants unique attributes to a-C, such as high hardness, low production costs, straightforward fabrication, exceptional chemical resistance, adjustable optical band gaps, and high optical transmittance, making it beneficial across various applications, including coatings, electronics, sensors, and optical devices (Cui et al., 2012; Kang et al., 2023; Roy et al., 2023; Zhang et al., 2022a). Theoretically, a-C in its pure, undoped form is described as exhibiting weak p-type characteristics. This p-type behavior is generally linked to intrinsic defects and localized states found within the material, which limit carrier transport and result in relatively low electrical conductivity (Ishak et al., 2015; Yap et al., 2009). Therefore, it becomes

essential to introduce a chemical dopant to diminish existing defects and simultaneously alter the electronic properties.

Doping a-C films with heteroatoms is a widely used technique to modify their band structure and manage their electrical properties. Various elements have been used as dopants in a-C, such as nitrogen and phosphorus, which are known to act as n-type dopants, while boron and iodine are identified as p-type dopants (Saleemi et al., 2021). In undoped a-C (p-type materials), electrical conduction mainly occurs through holes, which are essentially the absence of electrons in the valence band; given the low carrier concentration and mobility, this results in poor conductivity. Thus, the introduction of dopants can lead to a shift in the position of the Fermi level of a-C, thereby improving its electrical conductivity, a crucial aspect for the electronics industry (Roberts et al., 2025). However, it is well established that the choice of carbon precursors, as well as the deposition methods and their parameters, significantly affect the characteristics and hybridization of a-C films (Dai et al., 2015; Priyanto et al., 2024).

When creating a-C films, one of the most important factors to consider is the choice of precursors or starting materials. Typically, hydrocarbon precursors are selected, primarily composed of carbon, hydrogen, and oxygen molecules. This preference arises from the influence of the carbon compounds in these precursors on the growth of a-C films (Ouyang et al., 2021). In the early stages of identifying the right precursors, the majority of the carbon precursors have a controversial issue regarding the environmental and health issues due to their explosive and toxic nature (He et al., 2023). Consequently, given the rising demand for non-renewable resources and the accompanying concerns about pollution and climate change, researchers are seeking cost-effective, plentiful, and eco-friendly alternatives to traditional precursors (He et al., 2023; Kumar et al., 2016).

Currently, various types of precursors have been explored and utilized to effectively generate a-C films. These precursors consist of carbon-rich fossil hydrocarbons such as methane and coal, alongside naturally occurring carbon hydrocarbons, which come from the biomass of plants and animals, including natural oils like camphor oil and palm oil. Nevertheless, most gaseous and liquid fossil hydrocarbons are harmful to the environment and human health (Kumar et al., 2016). In contrast, natural hydrocarbons represent a renewable resource that can be sourced from several industries, such as livestock farming and agriculture, as well as from urban waste (He et al., 2023). Therefore, to produce a-C films, this research employed a

unique natural oil extracted from the waste component of oyster mushrooms, specifically the base of its fruiting body, as a carbon precursor.

According to Ikon et al. (Ikon et al., 2018), the oyster mushroom (*Pleurotus ostreatus*) is one of the edible fungi with a unique flavor and aroma, as well as having nutritional and medicinal benefits (Zhao et al., 2024). It possesses significant antioxidative, anti-carcinogenic, antibacterial, anti-cholesterolemic, and antiviral characteristics (Ikon et al., 2018). An oyster mushroom is made up of a fruiting body base, a stem, and a cap; however, commercially, the cap and stem are frequently harvested, while the base is commonly thrown away as waste (Wan-Mohtar et al., 2020). Given that the estimated cost to harvest and produce natural precursors is nearly RM 0.00, and considering that there is little risk of stock shortage in the near future, the discarded portion of the mushroom was selected due to an emphasis on low-cost options for synthesizing a-C films while promoting human and environmental health. This choice aligns with the principles of green chemistry, which advocate for the use of renewable feedstocks in industrial processes instead of depleting natural resources (Kumar et al., 2016).

As mentioned before, the structural and electrical properties of a-C films are significantly influenced by the type of carbon precursor used, along with the deposition technique and parameters such as the quantity of precursor, deposition temperature, and gas flow rate. Nonetheless, the growth parameters that might impact the film's properties, especially when employing a novel 'green' natural extract sourced from oyster mushrooms as a carbon precursor, are still not well understood. Therefore, in this work, a-C thin films deposited from oyster mushroom waste extract using the chemical vapor deposition (CVD) technique were studied.

1.2 Problem Statement

i. Problems of utilizing toxic and explosive carbon sources as precursors

It is believed that the choice of precursor affects the development of a-C thin films. A range of carbon precursors have been researched, including the conventional ones sourced from the carbon-based fossil hydrocarbons such as methane (Dadsetan et al., 2023; Das et al., 2025), ethylene (Ghimire et al., 2008), coal (Keller et al., 2016), and copper acetylide (Judai et al., 2016). These conventional precursors are deemed

unsustainable, hazardous, and toxic, leading to adverse effects on environmental and human health. Moreover, these precursors tend to be costly, and their availability has declined over the past few decades due to their non-renewable nature. Consequently, there has been significant research into utilizing carbon from natural resources. The application of carbon-based natural extracts or lipids from plant and animal biomass and biowaste (Fathy et al., 2017), as well as natural oils like camphor oil (Kamaruzaman et al., 2020), palm oil (Ishak et al., 2018), and palmyra sugar (Priyanto et al., 2021), has been explored. The presence of carbon elements in the bio-hydrocarbon precursors allows for the growth of a-C (Ouyang et al., 2021). However, in order to further minimize the cost of natural precursors and promote environmental conservation, it is essential to create precursors derived from natural sources, such as the oyster mushroom waste extract, which also has a high carbon content.

ii. Drawbacks of other synthesis methods for synthesizing amorphous carbon

Numerous approaches have been suggested to determine which methods are best suited for the fabrication of a-C, especially given that merely by the adjustments of their deposition parameters can significantly influence the properties of the resulting material. The mass production of these films has always posed difficulties, necessitating the exploration of a cost-effective method that also ensures the production of high-quality products. Various techniques have been used to deposit the films, including magnetron sputtering (Solovyev et al., 2018), pulsed laser deposition (Kayed, 2024; Wang et al., 2013), cathodic vacuum arc (Minglei et al., 2023), and chemical vapor deposition (CVD) (Toh et al., 2020). Among the various deposition methods, CVD stands out due to its lower cost and ability to produce high-quality a-C. Additionally, it is relatively easy to establish in a laboratory setting, has a long-standing record of successful applications, and can be scaled up for larger production. Other synthesis methods may lead to a high defect concentration and incur significant maintenance costs because of their complex systems.

iii. The low conductivity and mobility of undoped amorphous carbon due to its weak p-type behavior

The primary challenge in utilizing undoped a-C across various fields, particularly in electronics such as diodes, solar cells, and other devices, is its weak p-type nature and the significant density of intrinsic defects (Das et al., 2025; Saleemi et al., 2021). The intricate structure of a-C arises from the coexistence of sp^2 and sp^3 hybridization, which results in robust σ bonds alongside weaker π bonds. The electrical conductivity is heavily influenced by the sp^2/sp^3 carbon bonding ratio; however, due to the disordered nature of its amorphous structure and the presence of defect states, carrier transport is hindered, leading to weak p-type characteristics and poor conductivity (Saleemi et al., 2021; Wang et al., 2013; Yap et al., 2009). Consequently, many initiatives have taken place to improve its electrical properties, one of which is the doping method. By incorporating dopants like nitrogen, phosphorus, sulfur, and boron into a-C, there is a notable enhancement in electrical conductivity achieved through increased carrier density, the reduction of existing defects, and alterations in the band structure. Although extensive research has been conducted on a-C films, the specifics of doping under varying deposition conditions, particularly with the use of a novel natural extract as a carbon source, are not yet fully understood.

1.3 Research objectives

i. To investigate the suitability of oyster mushroom waste extract as a precursor to synthesize amorphous carbon thin films
ii. To examine the Chemical Vapor Deposition (CVD) technique to synthesize undoped and Nitrogen-doped amorphous carbon from oyster mushroom waste extract on a silicon substrate
iii. To determine the electrical properties of undoped and Nitrogen-doped amorphous carbon thin films

1.4 Research Questions

i. How suitable is oyster mushroom waste extract as a carbon precursor for synthesizing amorphous carbon thin films?
ii. What is the most suitable method that can be utilized to deposit undoped and Nitrogen-doped amorphous carbon?

iii. How does doping affect the electrical properties of amorphous carbon thin films compared to undoped films?

1.5 Significance of the study

This research is expected to contribute to the fundamental knowledge and understanding of the synthesis processes for both undoped and nitrogen-doped a-C films, as well as to aid in the selection of appropriate materials, particularly regarding the type of carbon precursors and deposition techniques, along with identifying the chemical dopants that can improve the electrical conductivity, which is assessed throughout the presented study. The findings from this research can also serve as additional knowledge for investigations focused on producing environmentally friendly materials. Using oyster mushroom waste extract as a carbon source facilitates the production of a-C films in an eco-friendly manner, as it reduces reliance on previously harmful and non-renewable materials. This study presents the effect of growth parameters on films deposited from a novel natural extract using the CVD technique, which has not been clearly understood before. The ideal parameters for both undoped and N-doped a-C films that exhibit the best conductivity have been identified.

This research provides crucial insights into the sustainable development of carbon materials across various sectors, especially in electronics, while addressing cost-related challenges and promoting the use of natural, eco-friendly materials in the industry. Moreover, a-C films possess high conductivity, excellent optical transmittance, and a tunable band gap, making them suitable for implementation in sensors, electrodes, coatings, and solar cell applications, thereby aiding in the achievement of the seventh Sustainable Development Goal (SDG 7), which focuses on affordable and clean energy utilization. Hence, this study may generate valuable information for the investigation of new materials for synthesis and for enhancing the properties of a-C in the future.

1.6 Scope and Limitations of Study

This study investigated the production of a-C films on a silicon substrate utilizing a new carbon precursor derived from oyster mushroom waste extract using the CVD technique. The study is divided into three main phases: the extraction of the oyster

mushroom waste extract, the deposition of amorphous carbon from the extract, and the characterization of both undoped and nitrogen-doped a-C.

This research commenced with phase 1, which focused on obtaining the extract from the lower portion of oyster mushrooms (*Pleurotus ostreatus*) via Soxhlet extraction, employing hexane and ethanol as solvents. Although Soxhlet extraction guarantees effective recovery of carbon-rich compounds and is more manageable due to its non-complex equipment, it does not permit the selective extraction of specific molecular fractions, and it also requires a long extraction time, using a large amount of solvents, and operates at high temperature. However, this limitation does not significantly affect this study because the extract used as a carbon precursor, with slight thermal degradation, does not have a negative impact on a-C deposition. The extract was subsequently evaporated using a rotary evaporator to eliminate the excess solvent. The resultant product from the extraction was then characterized using a CHNS analyzer to determine the carbon content in both the biomass and the extracted extract; however, this technique provides only bulk elemental composition and does not reveal the chemical bonding states of carbon. In addition, a thermogravimetric analyzer (TGA) was employed to evaluate the range of its decomposition temperature for CVD.

In phase 2, to produce undoped a-C, varying amounts of extract from oyster mushroom waste were loaded into the first furnace and heated to 350°C, based on the findings from the TGA analysis. Concurrently, the n-type silicon substrate was positioned in the second furnace, where it was heated to different deposition temperatures. Argon gas was allowed to flow through the quartz tube of the CVD system at varying gas flow rates. Each of the samples was synthesized for a duration of 30 mins. For the nitrogen-doped a-C, the same procedure was followed, but instead of using n-type silicon and argon gas, this time, the p-type silicon and nitrogen gas were used.

For the final phase, the samples were characterized using UV-Vis spectroscopy to assess the optical properties, along with Raman spectroscopy, scanning electron microscopy (SEM), and energy dispersive X-ray spectroscopy (EDX) to evaluate the structural properties, and 2-point probe current-voltage measurement for the electrical properties. While Raman spectroscopy is effective in identifying disorder and graphitic ordering in a-C, it provides limited details of the quantitative information on sp^2/sp^3 bonding ratios. SEM and EDX provide information on morphology and elemental

composition, yet the available instruments do not provide higher magnification in the nanoscale and lack the sensitivity required for detecting light elements such as nitrogen.

CHAPTER 2
LITERATURE REVIEW

2.1 Introduction

The literature review of this study is covered in this chapter. The first few sections describe the introduction of carbon, including its allotropes, which primarily concentrate on a-C, as well as their optical, structural, and electrical properties. The doping of the a-C is also reviewed in this chapter. The following section explains the several types of a-C synthesis, with an emphasis on CVD techniques, and the potential of various types of carbon precursors is then introduced, with the oyster mushroom serving as the carbon precursor for this study. Lastly, this chapter also reviewed the possible use of a-C in the industries.

2.2 Properties of Carbon

Carbon is a non-metal element known for its versatility, making it the most abundant element by mass in the Earth, and it ranks second to oxygen in terms of abundance within the human body (Yi et al., 2022; Zoroddu et al., 2019). It exists in various natural sources and living organisms, such as fossil fuels, including coal, natural gas, and oil, the DNA found in all living creatures, and carbon dioxide present in the atmosphere.

2.3 Allotropes of Carbon

There are numerous forms of carbon that exhibit malleability and have varying structures. Because of their valency, they have the ability to produce many allotropes, which are different structural forms of the same element. The carbon allotropes that have been known for a long time include fullerene, carbon nanotubes, carbon nanoribbons, amorphous carbon, graphite, graphene, and diamond (Hoffmann et al., 2016; Rivera et al., 2025). Nevertheless, some allotropes, such as carbyne and graphyne, remain unconfirmed. The various carbon allotropes can be categorized based on the type of chemical bonds and their hybridization, including sp, sp^2, and sp^3. For instance, the linear arrangement of the carbon molecule represents sp hybridization, which is

commonly found in carbyne and graphyne. In contrast, sp^2 hybridization exhibits a trigonal planar structure of carbon molecules, observable in graphite, graphene, carbon nanotubes, and fullerene. The sp^3 hybridization illustrates the tetrahedral structure of carbon molecules, prevalent in diamond. However, with a-C or diamond-like carbon, it primarily consists of a combination of sp^2 and sp^3 hybridization (Gaudiuso, 2023; Torrisi et al., 2024).

Diamond serves as an electrical insulator, showcasing 100% sp^3 hybridization, excellent transparency, and is recognized as the hardest naturally occurring material, attributed to its robust 3D diamond cubic lattice structure, which is incredibly strong and resistant to compression. The carbon atoms within diamonds are arranged in a tetrahedral formation with a carbon-carbon bond length of 1.54 A° (Li et al., 2015; N. Yang et al., 2019). Diamonds have diverse applications in various industries, including crafts and arts, cutting tools, and are predominantly utilized in jewelry (Yi et al., 2022).

In contrast, graphite is among the softest materials found in nature. This softness is attributed to its layered structure, which is maintained by weaker van der Waals forces that enable the layers to glide smoothly over one another. Graphite is an effective electrical conductor, opaque, and possesses significant natural stiffness and strength (Jara et al., 2019). Consequently, graphite is commonly utilized as a lubricant, in pencils where the layers can easily detach, in fuel cells as electrodes, for water purification, and in high-temperature industrial processes because of its high stability and melting point (Ahmed et al., 2023).

Fullerenes represent another category of allotropes, characterized by molecules that create hollow, cage-like structures formed by interconnected carbon atoms in hexagonal and pentagonal arrangements. The most famous fullerene is C60, which consists of 60 carbon atoms and is also referred to as Buckminsterfullerene or the bucky ball (Bhakta & Barthunia, 2020). They were initially discovered by Harold Kroto, Richard Smalley, and Robert Curl (Kroto et al., 1985) in 1985. The primary applications of fullerenes are in the fields of medicine and pharmacology, particularly in the creation of anticancer medications that combine endohedral fullerene compounds with radioisotopes (Bhakta & Barthunia, 2020; Yi et al., 2022). In addition, the tubular variations of fullerenes are known as carbon nanotubes.

Carbon nanotubes (CNTs) are a one-dimensional allotrope of carbon composed of a sp^2 hybridized carbon lattice configured in a cylindrical shape. CNTs can be categorized as single-walled (SWCNTs) or multi-walled (MWCNTs) (Hughes et al.,

2024). The characteristics and structure of CNTs are influenced by their helicity and diameter, typically represented by two Hamada indices (n, m). CNTs exhibit exceptional tensile strength and Young's modulus, significant thermal conductivity, and a low weight. The arrangement of carbon atoms, indicated by the indices (n, m), determines whether the CNT functions as a metal or a semiconductor (Yi et al., 2022).

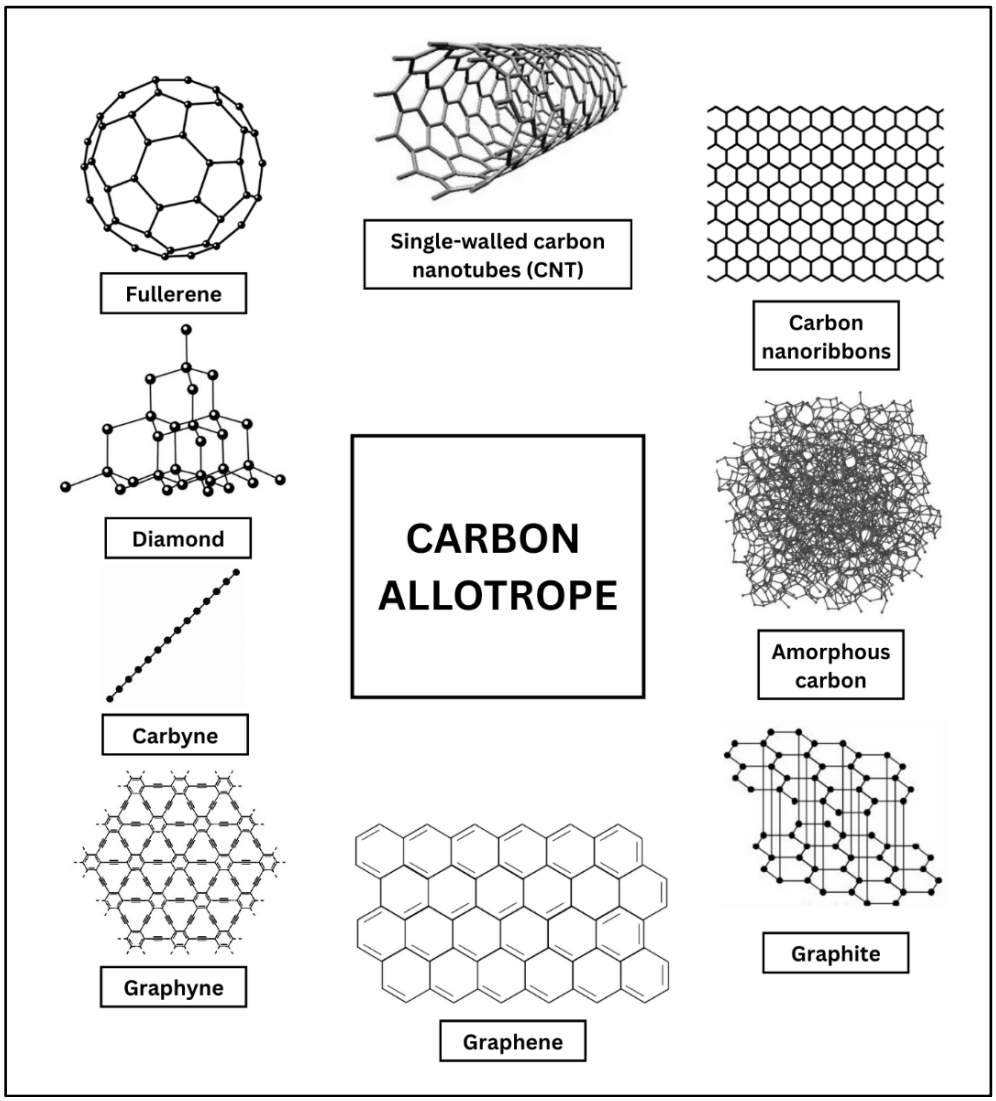

Figure 2.1 Types of Carbon Allotropes

2.3.1 Amorphous Carbon

2.3.1.1 Structure of Amorphous Carbon

Amorphous carbon differs from crystalline diamond and graphite in that it lacks a crystalline arrangement, resulting in irregular bonding between carbon atoms (Yi et

al., 2022). Within a-C, there are areas that resemble diamond-like structures and others that are more akin to graphite, yet there is an absence of long-range order (Honglertkongsakul et al., 2010). Consequently, a-C features both σ and π bonds owing to the combination of sp^2 and sp^3 hybridization present in the carbon framework (Ohtake et al., 2021; Priyanto et al., 2024). Altering the proportion of these hybridizations can influence the material's properties (Chen et al., 2015). Additionally, it possesses a significant amount of dangling π-bonds, which can be stabilized by the introduction of hydrogen. Amorphous carbon is characterized by distinctive properties such as a low friction coefficient, high hardness, impressive wear resistance, excellent biocompatibility, innovative optical and electrical features, and significant chemical inertness (Roy et al., 2023).

The characteristics of these materials are significantly influenced by deposition parameters, including temperature, method, precursor type, and carrier gas flow rate. Various intermediate carbon forms can be encountered, such as diamond-like carbon (DLC), hydrogen-free amorphous carbon (a-C), hydrogenated amorphous carbon (a-CH), tetrahedral hydrogen-free amorphous carbon (ta-C), diamond-like amorphous carbon (DAC), and graphite-like amorphous carbon (GAC). The DAC or DLC was initially created by Aisenberg and Chabot (Aisenberg & Chabot, 1971) in 1971 through ion-beam deposition. If a material exhibits a high sp^3 content, it is classified as DAC, which is dense, hard, possesses diamond-like optical properties, and has applications in electronic devices (Salek et al., 2023; Yi et al., 2022). Conversely, materials with a high sp^2 content is softer, more conductive, and displays a graphitic-like a-C structure.

2.3.1.2 Optical Properties

The optical characteristics of a-C have been examined to assess their suitability for use in optical systems and to uncover information regarding the films' microstructure and bonding arrangements. The dominant optical features of a-C films are attributed to π-π* and σ-σ* interband transitions. The π and π* states arise solely from the sp^2 carbon atoms and are responsible for the transitions of π-bonded electrons (p_z orbitals) to π* antibonding states. Conversely, the σ-σ* transition is associated with the σ-bonded electrons involved in the covalent bonds of both sp^2 and sp^3 carbon atoms (Patsalas, 2011). As previously noted, depending on the synthesis method and conditions used for the carbon layers, the resulting material typically comprises carbon atoms with sp^2 and

sp^3 hybridization, and its characteristics are heavily influenced by the bonding among the carbon atoms. In the case of a diamond, which features sp^3 hybridization, only σ bonds are present. In contrast, materials containing carbon atoms with both sp^2 and sp^3 hybridization forms additional π bonds, creating localized conduction states (Skowronski et al., 2023).

The widening of the optical band gap is attributed to the rise in sp^3 contents. For instance, a diamond, which consists solely of σ bonds, possesses a significant energy gap of 5.5 eV due to σ → σ* transitions. The increased presence of sp^2 bonds among carbon atoms lead to the development of highly localized π states, which enhance the chances of π → π* transitions and consequently reduce band gap energy (Skowronski et al., 2023). Therefore, it can be anticipated that with fewer π states, there will be a greater spectral separation between π and π*, resulting in a higher band gap (Patsalas, 2011).

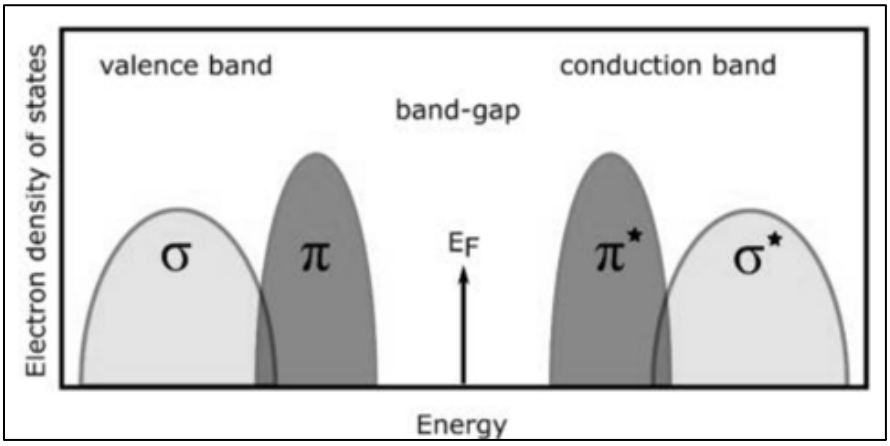

Figure 2.2 Schematic Diagram of the Density of States of a-C

2.3.1.3 Structural Properties

The structural attributes of a-C films are intriguing, complemented by their outstanding electrical and optical characteristics. Due to their amorphous nature, the structure of a-C is complex, comprising both π and σ bonding states. Raman spectroscopy serves as an effective nondestructive method for assessing the structural properties of carbon materials, encompassing a range from graphitic carbon to a-C films (Yuan et al., 2025). Raman bands or peaks are utilized to distinguish different carbon allotropes in carbon-based nanostructured materials (Roy et al., 2021). In carbon

materials, three prominent peaks can be observed: the D, G, and 2D Raman peaks. The D peak appears in the range of 1310-1390 cm^{-1}, the G peak is found between 1575-1600 cm^{-1}, and the 2D peak is present around 2690-2700 cm^{-1} (Li et al., 2013). However, in the Raman spectrum of a-C films, only the D and G peaks are detectable, with the 2D peak being absent (Mitra et al., 2024).

The presence of these two peaks suggests the existence of sp^2 and sp^3 carbon bonding (Yuan et al., 2025). The G peaks are produced by the E_{2g} symmetry mode of the hexagonal carbon lattice, which is characteristic of all sp^2 carbon, indicating the stretching of in-plane carbon bonds. On the other hand, the D peaks arise from the vibrations of sp^2 carbon atoms with A_{1g} symmetry, which only become active in the presence of disorder. However, this D peak is only observable in disordered graphite or a-C and is not permitted in ideal graphite, which is expected to have more orderly carbon arrangements (Moseenkov et al., 2023). Information about the structure related to sp^2 clustering and disorder can be derived from the positions, intensities, and widths of the peaks, with the intensity ratio (I_D/I_G) reflecting the ordering of the sp^2 phase (Yuan et al., 2025). An increase in the I_D/I_G ratio may result from a reduction in sp^3 content within the a-C (Gabhi et al., 2020).

2.3.1.4 Electrical Properties

Amorphous materials can function as conductors, semiconductors, and silicon (Purwandari et al., 2025). As previously noted, the electrical characteristics rely on the variation in the ratio of sp^2 and sp^3 hybridization of carbon present in a-C. This is attributed to the presence of π electrons in the sp^2 carbon, which facilitates electrical conductivity (Gabhi et al., 2020). This phenomenon can be connected to the positioning of the π states in sp^2 carbon, as they are closest to the Fermi level when compared to the σ states. It is evident that the π states create tail states associated with the edges of the valence and conduction bands, contributing to the density of localized states within the gap (Koós et al., 1999). Therefore, electrical conductivity is influenced by the quantity and arrangement of sp^2 sites, whether consisting of larger or smaller sp^2 clusters within the materials (Gabhi et al., 2020).

Amorphous carbon can demonstrate weak p-type semiconducting characteristics, marked by a high density of defects that influence its electrical

properties (Das et al., 2025; Saleemi et al., 2021). These materials feature more robust σ bonds and weaker π bonds, resulting from the presence of both sp^2 and sp^3 hybridization. It has been noted that the disordered nature of a-C, along with the existence of defects, obstructs carrier transport, leading to weak p-type behavior and low conductivity (Saleemi et al., 2021; Wang et al., 2013; Yap et al., 2009). Therefore, the introduction of dopants was applied to adjust the Fermi level position in a-C films, enhancing the electrical conductivity by increasing carrier density and decreasing defects (Roberts et al., 2025). Additionally, it has been reported that incorporating dopants reduces the compressive stress within the a-C films (Tali et al., 2017).

2.4 Doping of Amorphous Carbon

Amorphous carbon typically exhibits mild p-type characteristics and has lower electrical conductivity than crystalline semiconductors, but this can be adjusted by adding dopants to the films. The conductivity of a-C is affected by the Fermi level's position and the doping process. Various elements can serve as dopants, including nitrogen and phosphorus, which act as n-type dopants, whereas boron and iodine function as p-type dopants (Saleemi et al., 2021). The introduction of these elements leads to an increase in the film's sp^2 content, which results in a reduction of the optical band gap, a shift in the Fermi level's position, a decrease in energy gap states, and an enhancement in conductivity (Roberts et al., 2025).

Numerous studies have successfully examined the influence of doping on the electrical characteristics of a-C films. In a research conducted by Podder et al. (Podder et al., 2005), boron was doped into hydrogenated a-C using the RF-PCVD method, employing pure methane as the carbon source and hydrogen as the carrier gas. The investigation revealed that the properties of the films were influenced by the presence of the boron dopant. The findings indicate that the optical band gap decreases from 2.60 eV to 1.58 eV as the partial pressure of the methane/hydrogen gas is lowered.

A comparable investigation utilizing boron as a doping agent was conducted by Rui Zhu et al. (Zhu et al., 2019) in which they applied boron-doped a-C onto a glass substrate via magnetron sputtering using argon gas as the processing gas. It was observed that as both boron and carbon target power were increased, the sp^2 content rose and the optical band gap reduced from 3.19 eV to 2.78 eV. The reduction in the optical band gap was determined to be due to boron atoms facilitating the development

of sp^2 clusters at lower energy levels in conjunction with carbon. Furthermore, boron atoms tend to interact with carbon σ bonds in the sp^3 hybridization by establishing B-C bonds with elevated energy, thereby promoting the transition from sp^3 hybridization to sp^2 hybridization.

Priyanto et al. (Priyanto et al., 2021) examined how the introduction of boron and nitrogen dopants affects the structural, electrical, and optical properties of a-C that was deposited from palmyra liquid sugar using the nano-spraying technique. Their findings revealed that the occurrence of B-C bonding indicates that boron effectively reduces the sp^3 bonds to sp^2 bonds by integrating with carbon and substituting for it. In contrast, the nitrogen dopants present in the a-C are encircled by carbon atoms that possess a π bond, which allows nitrogen to easily replace carbon atoms within a network of double bonds, requiring less energy for substitution, thereby leading to an increase in the sp^2 content in the films. Regarding electrical and optical properties, the nitrogen-doped material exhibited an increase in conductivity from 0.54 to 0.59 $\Omega^{-1}cm^{-1}$ while the optical band gap decreased from 0.113 to 0.060 eV, when compared to the undoped a-C. Additionally, the boron-doped a-C also showed an increase in conductivity from 0.54 to 0.56 $\Omega^{-1}cm^{-1}$ and a decrease in the optical band gap from 0.113 to 0.090 eV. Nevertheless, the results indicated that nitrogen doping is more efficient than boron doping for achieving higher conductivity and a lower band gap.

In a subsequent study, Sekhar Ray et al. (Ray et al., 2014) showed that the electrical characteristics of nitrogen-doped a-C deposited on a silicon substrate using methane and nitrogen as source gases through the pulsed laser deposition method undergo changes. It is observed that the intensity ratio of the D and G peaks rises with the nitrogen concentration, suggesting the formation of sp^2 clusters that contribute to the conductivity of the films, along with an enhancement in current density compared to the undoped films. The introduction of nitrogen doping appears to enhance the conductivity and reduce the resistance of the films through the development of sp^2 clusters, which leads to an increase in localized hopping states.

2.5 Synthesis of Amorphous Carbon

Numerous methods have been suggested to identify the most effective techniques for producing a-C based on the manufacturer's goals. This is due to the fact that minor changes in deposition parameters can greatly affect the properties of the

materials. The challenges associated with the mass production of these materials necessitate the exploration of cost-effective strategies while ensuring the delivery of high-quality a-C. A variety of techniques have been created to produce a-C, which can be classified into two primary categories: top-down and bottom-up approaches. However, prior research indicates that the majority of synthesis methods employed tend to fall within the bottom-up category. Although top-down methods are less frequently used for the synthesis of a-C, they are employed for shaping or reducing carbon materials into a-C structures (Abid et al., 2022).

The methods for synthesizing a-C films can be divided into bottom-up and top-down strategies; however, the majority of commonly used synthesis techniques belong to the bottom-up category. The top-down strategy includes methods such as pulsed laser ablation (PLA) and ion beam sputtering, while the bottom-up strategy encompasses techniques like magnetron sputtering, cathodic vacuum arc (CVA), pulsed laser deposition (PLD), and chemical vapor deposition (CVD) (Roy et al., 2023). In the top-down approach, bulk materials like graphite are transformed by breaking them down into smaller nanoparticles. This method decreases the size of the original material to produce a-C structures (Abid et al., 2022). On the other hand, the bottom-up approach utilizes a variety of carbon sources other than graphite as precursors to form a-C and different carbon allotropes. Unlike the top-down method, where graphite is fragmented into tiny pieces, these techniques build the films from the precursors. Overall, the bottom-up approach typically results in higher-quality a-C, as it allows for more precise control over growth parameters, which is crucial since these parameters affect the films' properties.

Table 2.1
Comparison of Top-Down and Bottom-Up Approaches for a-C Synthesis

Approach	Description	Advantages	Disadvantages	Example	Ref.
Top-down	Breaking down bulk carbon (graphite) into a smaller size (amorphous carbon)	Precise thinning and patterning	Defect introduction, poor thickness, and limited scalability	PLA, ion beam sputtering	(Abid et al., 2022; Angelucci et al., 2002; Roy et al., 2023; Sportelli et al., 2018)
Bottom-up	Building amorphous carbon films from carbon precursors	Controls film growth and properties	Some of the methods that use a vacuum are expensive	Magnetron sputtering, CVA, CVD	(Solovyev et al., 2018; Tu et al., 2025)

2.5.1 Chemical Vapor Deposition (CVD)

Chemical Vapor Deposition (CVD) is among the most popular bottom-up techniques for carbon synthesis. It is favored over other methods due to its cost-effectiveness, simplicity, and the ability to control film characteristics via process parameters and precursor selection. Additionally, it is easy to set up in research labs, has a proven track record for long-term industrial use, and can be scaled up for production (Saeed et al., 2020; Y. Yang et al., 2019). Unlike other methods that require a vacuum or low-pressure environment and long synthesis times, which demand advanced technology and equipment, CVD minimizes these challenges while keeping costs low (Zhu et al., 2018). Therefore, considering ecological and economic aspects, the CVD method is ideal for producing a-C. Furthermore, it is classified as a bottom-up approach since it utilizes organic compounds, primarily hydrocarbons, as precursors for synthesizing a-C. This method is particularly effective for deposition on large and complex substrates, producing high-purity and high-performance thin films due to the uniform decomposition of vaporized carbon sources at elevated temperatures, resulting in fewer defects and enhanced graphitization (Kamaruzaman et al., 2012; Y. Yang et al., 2019).

The CVD method entails a chemical reaction where carbon from gaseous carbonaceous precursor molecules is thermally deposited onto a substrate at elevated temperatures. Subsequently, the substrate is allowed to cool, which decreases carbon solubility on the substrate and triggers surface nucleation, resulting in the formation of one or more layers of carbon (Ismail et al., 2019; Yan et al., 2020). As previously stated, the variety and quality of the final products are influenced by a range of manufacturing parameters, such as the types of catalysts used, the substrates and precursors chosen, gas flow rate, pressure, temperature of the substrates and precursors, as well as the durations for growth and cooling (Saeed et al., 2020; Yan et al., 2020).

For example, Xiaoming Tu et al. (Tu et al., 2025) managed to successfully deposit an amorphous monolayer of carbon (AMC) on copper foil substrates using CVD with carbon vapor produced from the sublimation of a graphite rod. Another investigation employing the same substrate but yielding a different end product is the work by Kumar et al. (Kumar et al., 2018) who synthesized nitrogen-doped graphene quantum dots (N-GQD) from chitosan on copper foil substrates through the CVD process. Additionally, it has been noted that the size and density of the products can be

manipulated simply by varying the growth time during the deposition. Kamaruzaman et al. (Kamaruzaman et al., 2020) effectively deposited a-C and iodine-doped a-C films on a glass substrate sourced from camphor oil through thermal CVD. The findings indicate that the conductivity of iodine-doped a-C is greater than that of the undoped films.

2.6 Potential Precursors for Amorphous Carbon Synthesis

The precursor serves as a crucial material in the synthesis of carbon, as it can significantly impact the growth of the final product. Precursors can be described as compounds that possess the essential elements needed to create a thin film on a substrate, where they decompose upon reaching the heated substrate to deposit the desired material as a solid film. The most commonly utilized precursors are primarily hydrocarbons due to their carbon compound content (Ouyang et al., 2021). Numerous sources have been employed in the past to produce a-C, including conventional precursors, which are largely derived from fossil hydrocarbons, as well as environmentally friendly alternatives, most of which come from natural hydrocarbons.

2.6.1 Conventional Precursors

For the past decades, the primary sources for carbon materials have been derivatives of fossil fuels such as methane, ethylene, and coal, which are both toxic and non-renewable (He et al., 2023). Alternatively, there are precursors derived from raw materials, like graphite, that can be used in the synthesis of carbon materials. Additionally, the production costs of the final products tend to be high due to the demanding and energy-intensive synthesis processes, making them unsuitable for large-scale manufacture. The sustainability of these sources is questionable, and there is a significant chance they could be exhausted in the near future.

Table 2.2
Research Gap on Previous Types of Conventional Precursors

Conventional Precursors	Final product	Methods	Ref.
Methane (CH_4)	Amorphous carbon	Fabricated using radio frequency plasma-enhanced CVD (RF-PECVD)	(Priyanto et al., 2019)

	Amorphous carbon	Fabricated onto GaAs and InP substrates using the PECVD process	(Henksmeier et al., 2024)
Iodomethane (CH_3I)	Amorphous carbon	Synthesized onto glass substrates by using the PE-CVD technique with iodine added	(Das et al., 2025)
Ethylene (C_2H_4)	Amorphous carbon	Grown on silicon, indium tin oxide (ITO), and quartz substrates by using microwave surface wave plasma CVD (MW SWP CVD)	(Ghimire et al., 2008)
	Carbon nanotubes	Synthesized onto a catalytic substrate (stainless steel) using CVD	(Zhuo et al., 2018)
Acetylene	Graphene	Synthesized by the magnetically rotating arc under atmospheric pressure	(Chen et al., 2019)
	Carbon nanotubes covered with amorphous carbon	Stepwise films of iron on a crystal silicon substrate obtained by the pulsed laser deposition (PLD), which was used as a catalyst. Then, synthesized by the modified CVD method in the tube flow reactor via catalytic pyrolysis of acetylene	(Egorov et al., 2021)
Coal	Graphene and amorphous carbon	Synthesized using CVD with graphene formed on nickel substrates, while amorphous carbon formed on copper foils	(Rane et al., 2021)
Graphite	Amorphous carbon	Developing the materials via a one-step sintering process using the SPS apparatus in a vacuum atmosphere	(Liang et al., 2025)
	Amorphous carbon	Synthesized using magnetron sputtering with graphite and nickel as targets and GaAs as substrate	(Solovyev et al., 2018)
Graphite	Amorphous carbon	Fabricated onto mono-crystalline n-type silicon wafer using a frequency-doubled pulsed Nd;YAG laser (PLD) under vacuum, followed by rapid thermal annealing	(Ismail et al., 2014)

2.6.2 Green Alternatives Precursors

The extensive reliance on non-renewable resources has raised concerns among society primarily due to the toxic by-products that can lead to pollution and the generation of greenhouse gases, as well as detrimental effects on environmental health. Hence, researchers have sought to tackle this issue by creating a green alternative that is beneficial both economically and environmentally. Examples of these green alternatives include biomass materials such as decomposed plants, biological wastes, and natural oils, which have successfully achieved the primary goal of substituting non-renewable resources as precursors. These materials can be sourced from various industries, such as agriculture, forestry, and livestock farming (He et al., 2023). The traits of these precursors that position them as preferable choices over traditional precursors include their non-toxic nature, availability, cost-effectiveness, and sustainability (Yan et al., 2020).

To generate high-quality a-C, the carbon content present in the precursors must be considered prior to selection, and these alternative sources are deemed suitable materials because they comprise long chains of carbon, hydrogen, and oxygen molecules. With their high carbon content and varied molecular structures, biomass can be transformed into carbon materials featuring different configurations, enabling these materials to be utilized in a wide range of applications. Furthermore, the transformation of biomass into high-value carbon products is significant in light of its advantages regarding waste management, biomass valorization, and reduced carbon emissions (He et al., 2023).

Table 2.3
Research Gap on Previous Types of Green Alternative Precursors

Alternative Precursors	Final product	Methods	Ref.
Palm oil-based cooking oil	Amorphous carbon	Fabricated onto a silicon substrate with zinc nitrate solution as a catalyst using a dual-furnace CVD method	(Zobir et al., 2011)
Refined cooking palm oil	Graphene	Grown on a copper substrate that act as metal catalyst using a homemade spray injector-assisted CVD	(Maarof et al., 2019)

Camphor oil	Amorphous carbon	Deposited onto the glass and silicon substrates using the thermal CVD method	(Kamaruzaman et al., 2020)
Charcoal of coconut shells and Palmyra sap carbon	Amorphous carbon	The carbon materials derived from biomass are deposited onto a quartz glass surface via spray coating	(Purwandari et al., 2025)
Palmyra sugar	Amorphous carbon	Deposited on the ITO glass substrate using the nano-spraying method	(Priyanto et al., 2024)
Coconut sap	Amorphous carbon	The powder was successfully prepared by the carbonization process and then deposited using spin-coating	(Pamungkas et al., 2019)
Cellulose in rice straw	Amorphous carbon	Prepared through a batch acid spraying technique in the presence of cobalt silicate as a catalyst	(Moubark et al., 2016)
2,4,6-Tris(dimethylamino)-1,3,5-triazine ($C_9H_{18}N_6$)	Carbon nitride	Grown onto quartz substrates from an organic molecule using the CVD method	(Murahari et al., 2020)
Chitosan	N-doped graphene quantum dots	Fabricated onto copper foils using the CVD technique	(Kumar et al., 2018)
Sugarcane dry leaves	Graphene oxide	Generated by using a facile two-stage pyrolysis method, assisted with ferric (III) citrate as a catalyst.	(Thangaraj et al., 2023)

2.6.2.1 Oyster Mushroom (Pleurotus ostreatus)

Oyster mushroom, scientifically known as *Pleurotus* genus, is one of the famous edible mushrooms or fungi that is considered a delicacy due to its aroma, texture, and flavor, along with its exceptional nutritional and medicinal benefits (Tagkouli et al., 2021). In addition, oyster mushrooms are also one of the most cultivated fungi in the

world, along with button mushrooms (*Agaricus bisporus*) and shiitake mushrooms (*Lentinula edodes*), with them taking 16% of the global supply (Zhou et al., 2023). This second most consumed mushroom (oyster mushroom) has more than 40 commercial species, including *P. ostreatus, P. pulmonarius, P. sajor-caju, P. eous, P. eryngii, P. djamor*, and *P. citrinopileatus* (Tagkouli et al., 2021). Among these species, *Pleurotus ostreatus* has gained a lot of attention due to its bioactive significance and other health-promoting abilities. For instance, this edible mushroom is rich in proteins, unsaturated fatty acids, phenolics, flavonoids, glycoproteins, terpenoids, steroids, and alkaloids, along with its pharmacological and therapeutic abilities such as antioxidant, antitumor, antimicrobial, anti-viral, anti-inflammatory, and antihypertensive (Elhusseiny et al., 2021; Ianni et al., 2021).

Furthermore, having a high carbon content in the precursor is one of the essential criteria for serving as a carbon source for the synthesis of a-C films. Previous research has indicated that mushrooms possess a sufficiently high carbon content to facilitate the growth of these films. Additionally, during the characterization process, nitrogen content was analyzed, which could potentially contribute to the creation of nitrogen-doped a-C. For example, Roy Das et al. (Roy Das et al., 2014) found that the wild edible mushroom *Pleurotus djamor* contains a carbon percentage of 37.42% and a nitrogen content of 4.61% when analyzed using a CHN-OS analyzer. Moreover, Gunasekaran et al. (Gunasekaran et al., 2021) also examined the carbon content of the mushroom *Pleurotus eous*, commonly referred to as the pink oyster mushroom, which was found to have a carbon percentage of 41.08% and a nitrogen percentage of 4.99% according to measurements taken with a CHNS elemental analyzer. Both of these mushroom species exhibit high carbon content and belong to the same genus as the oyster mushroom, *Pleurotus ostreatus*.

Global mushroom production has more than doubled during the past few decades, making mushroom agriculture a significant sector of the agricultural industry (Mwangi et al., 2024). The top producers of mushrooms are Malaysia, China, India, and Ireland. About 50 tons of mushrooms are needed every day in Malaysia, but only 24 tons are being produced. Malaysia, therefore, imported more than 2.71 million tons of fresh mushrooms and 3.11 million tons of dried mushrooms from China in 2012 to meet the rising demand for mushrooms. Each mushroom farm normally produces 100 tons of fresh mushrooms annually, according to Phan and Sabaratnam's research (Phan & Sabaratnam, 2012). China can be seen produces 1.5 million tons of mushrooms

annually, making it one of the world's leading producers. Production is expected to increase by as much as 65% over the next 10 years (Hanafi et al., 2018).

However, millions of tons of spent mushroom compost (SMC), the biomass waste of mushrooms, which includes the lower part of the mushroom that is usually discarded had been generated. This has become an issue that impedes the expansion of the mushroom industry and has an adverse effect on the environment (Mwangi et al., 2024). After the mushroom fruiting bodies are harvested, the farm produces a large amount of SMC. For every kilogram of fresh mushrooms, about 5kg of SMC is produced (Rusli & Jaludin, 2025). According to earlier research, Malaysia's current SMC management disposal methods–burning, composting, and landfill disposal–are not totally eco-friendly (Hanafi et al., 2018). Therefore, it is believed that using mushroom waste as a carbon precursor for a-C films production is an alternative to alleviate the problems associated with disposing of discarded mushrooms. Given its eco-friendliness, abundance, high carbon content, cost-effectiveness, and renewable nature, it has been selected as the carbonaceous precursor for synthesizing a-C in this research.

2.7 Potential Application of Amorphous Carbon

Amorphous carbon thin films possess several unique characteristics, including exceptional chemical stability, an adjustable optical band gap ranging from 0.0 to 5.5 eV, and semiconducting properties. The structure and features of amorphous materials have garnered attention for their potential uses across various domains, particularly in electronic devices like photovoltaic solar cells. Previous research indicates that a-C has been utilized to create a diverse array of applications for the solar industry, such as anti-reflection and self-cleaning coatings for crystalline silicon solar cells (Addie et al., 2022; Yang et al., 2021), heterojunction solar cells (Rajanna et al., 2022; Wu et al., 2021), and a window layer (Kouider et al., 2020). Additionally, a-C films demonstrate a greater sunlight absorption capacity compared to amorphous silicon when at equal thicknesses. The capacity for sunlight absorption and the consequent photocurrent can be manipulated by varying the hydrogen content and density.

For the past years, silicon solar cells have been the most commonly studied application for a-C, as they represent a highly promising solar technology based on naturally occurring silicon (Adeyinka et al., 2023). However, due to the high expenses

associated with silicon solar cells, researchers have been motivated to investigate lower-cost yet high-efficiency solar cell alternatives. In this quest for alternative materials, researchers have utilized a-C films to create thin-film solar cells. This is primarily because of their strong ability to absorb sunlight, allowing for the use of a thinner layer of material, which in turn lowers manufacturing costs (Adeyinka et al., 2023). Additional benefits of a-C solar cells include their higher theoretical conversion efficiency attributed to the adjustable optical band gap, more affordable materials and deposition techniques, and the potential to use cheaper precursors and substrates for deposition.

Research institutions are continuing to explore ways to fully enhance the properties of a-C to fulfill its role as an alternative material for specific applications. Nevertheless, earlier investigations into the viability of a-C for solar cells were lacking in essential understanding or research regarding its electrical, structural, and optical properties, as well as their relationship with the growth parameters of a-C, which remains ambiguous. Understanding this relationship is crucial to unlocking the complete potential of a-C as an alternative for solar cell materials.

2.8 Chapter Summary

Based on the reviewed literature, a-C and a-CN thin films have typically been produced via CVD with traditional gaseous and petroleum-based carbon sources. Many studies have demonstrated how the deposition parameters and the addition of nitrogen affect the structural, optical, and electrical properties of carbon-based thin films. Nonetheless, there has been relatively little focus on the use of biomass waste-derived extracts, particularly using oyster mushroom waste, as alternative carbon precursors for thin film deposition using CVD. Furthermore, there are fewer, if any, studies that can be found between the undoped and a-CN films derived from the same biomass source. Consequently, a clear research gap exists in the development of undoped and a-CN thin films synthesized from oyster mushroom waste extract using CVD. This research aims to fill this gap by examining the potential of biomass-derived extract as a carbon precursor and conducting comparative investigations between undoped and a-CN thin films by using this source.

CHAPTER 3
RESEARCH METHODOLOGY

3.1 Introduction

The method of research employed in this study is covered in detail in this chapter. This project is a collaboration between UiTM Solar Research Institute (SRI) and Universiti Malaya (UM). All of the mushroom waste extract extraction and characterization were done at the Functional Omics and Bioprocess Development Laboratory, Institute of Biological Sciences, Universiti Malaya, while the synthesis of amorphous carbon (a-C) and fabrication of the devices were all done at Nano Electronic Centre (NET), College of Engineering, UiTM Shah Alam. For the characterization, it was done at the NET UiTM Shah Alam and UNITEN. There are three phases involved in producing these a-C thin films, as shown in Figure 3.1. The first phase describes the preparation and extraction of oyster mushroom (*Pleurotus ostreatus*) waste extract. The following section explains how Chemical Vapor Deposition (CVD) is used to deposit a-C from mushroom waste extract. The last phase involves the characterization of a-C.

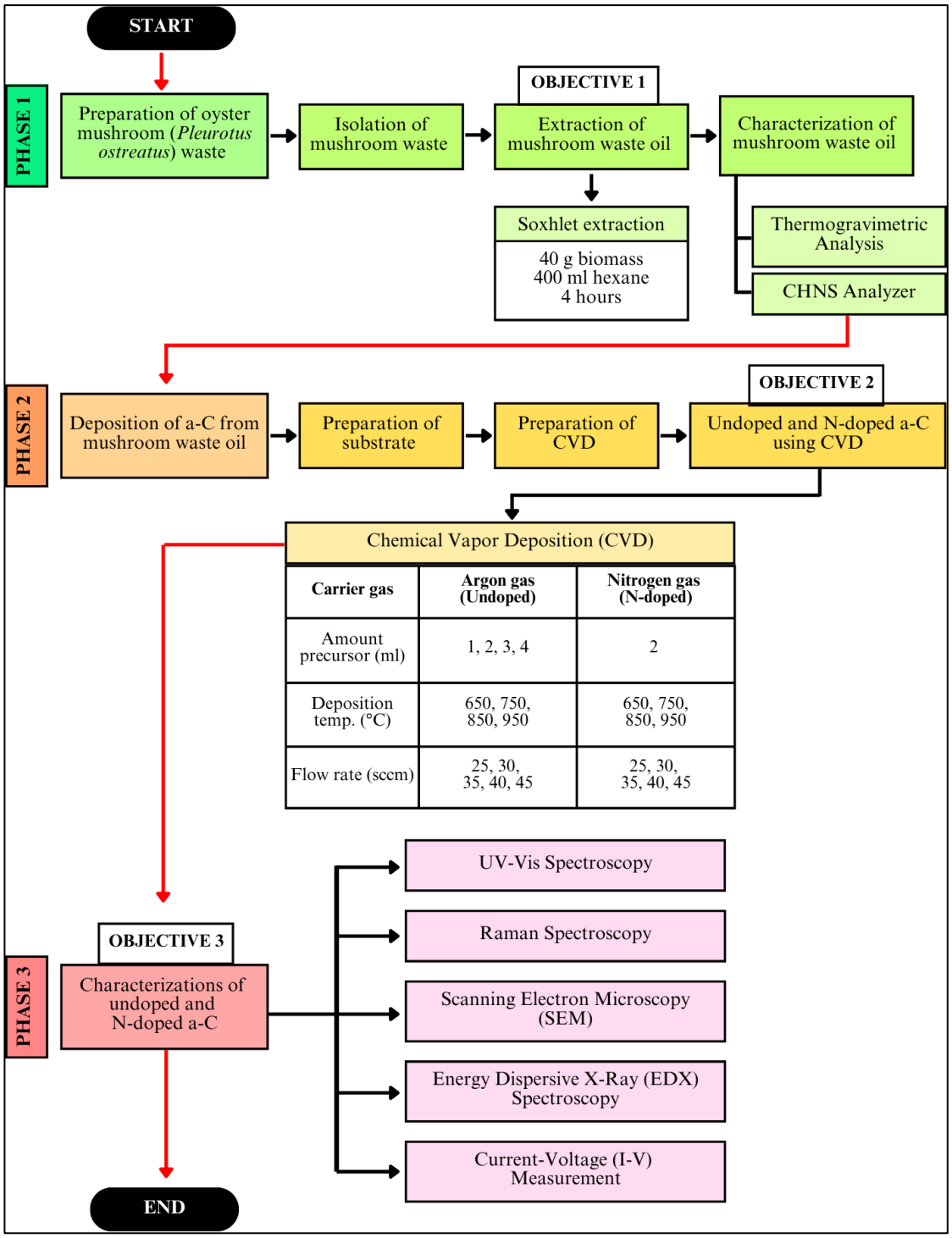

Figure 3.1 Flowchart of Research Methodology

3.2 Materials

The materials used as precursors are the extract of the waste part, which is the base of the fruiting body of the oyster mushroom (*Pleurotus ostreatus*), extracted using Soxhlet extraction. The extraction of the oyster mushroom waste biomass powder uses 99% n-hexane (ChemAR, Systerm) as a solvent. Acetone (C_3H_6O), deionized waste,

methanol (CH_3OH), and diluted hydrochloric acid was used to clean the silicon substrate and glass substrate from organic contaminants and native oxides. During the Chemical Vapor Deposition (CVD) process, pure undoped a-C synthesis was carried out using argon (Ar) gas as the dopant and carrier gas, while N-doped a-C (a-CN) synthesis was performed using nitrogen (N) gas. An n-type silicon substrate was utilized for the deposition of a-C thin films, whereas a p-type substrate was employed for a-CN films. The samples were then coated with gold (Au) using sputtering and a thermal evaporator.

Energy Dispersive X-Ray (EDX) Spectroscopy, Raman Spectroscopy, and Scanning Electron Microscopy (SEM) were used to describe the structural properties of each sample. Current-voltage (I-V) measurements were performed to evaluate electrical conductivity, while UV-Vis spectroscopy was employed to ascertain optical characteristics.

3.3 Oyster Mushroom (*Pleurotus ostreatus*) Waste Preparation

3.3.1 Oyster Mushroom Waste Isolation

The oyster mushroom harvest, which was obtained from a local producer, the Mushrooms Unit, Universiti Putra Malaysia (UPM), involved cutting off the lower portion of the fruiting body − the waste mushroom biomass (WMB), which is normally discarded − from its fruiting body. The WMBs were cleaned of soil and insects and dried in an oven dryer at 50°C overnight. The laboratory blender was then used to grind the dry WMBs into a fine powder. The resultant waste flour or powder was kept dry until it was needed by storing it in a bottle with silica gel. The waste mushroom flour preparation flow is shown in Figure 3.2 from pictures A to H.

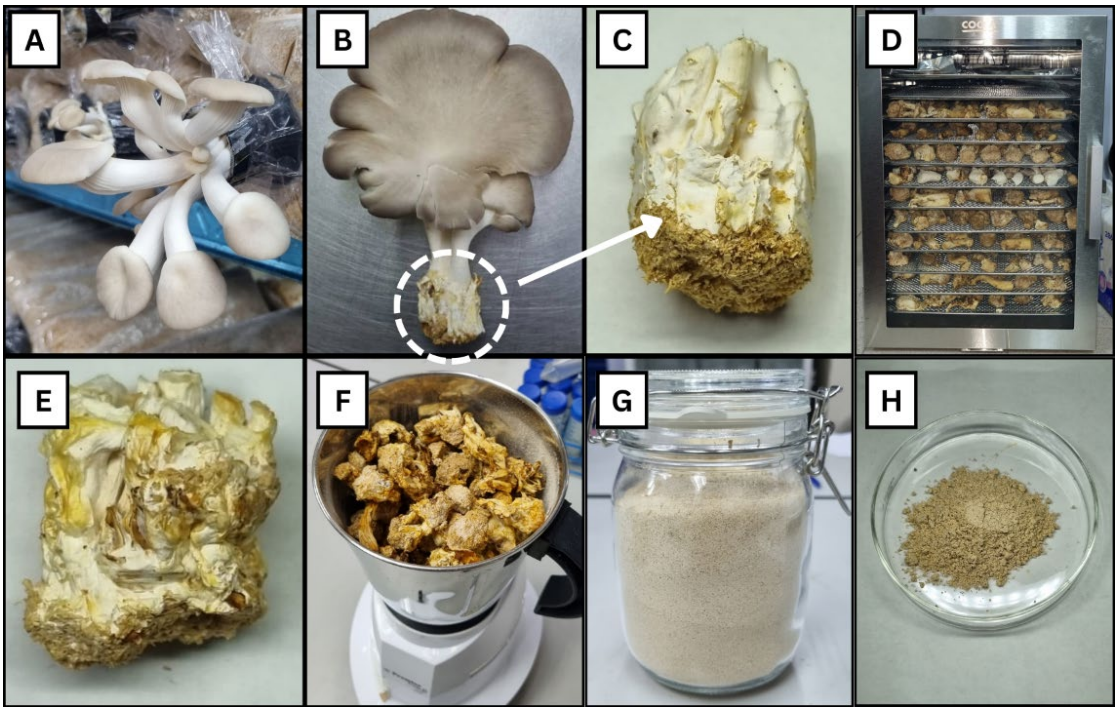

Figure 3.2 Preparation of the Oyster WMB A) Fresh Oyster Mushroom, B) Whole Fruiting Body, C) Fruiting Body Base, D) Oven-Dried Mushroom Waste, E) Dried Fruiting Body Base, F) Grinding of Dried Waste, G) Stored Mushroom Waste Flour, And H) Final Fine Mushroom Waste Flour

3.3.2 Oyster Mushroom Waste Extract Extraction

Using the technique described in the literature with slight adjustments, the extraction of extract was carried out through Soxhlet extraction with n-hexane (99%, ChemAR, Systerm) and ethanol (denatured 95%, ChemAR, Systerm) as solvents. A cellulose extraction thimble (CT43123) containing 40 g of fine powder WMB was set in the Soxhlet apparatus along with 400 ml of hexane, which acts as a solvent was heated to 80°C for 4 h. In order to obtain 1 ml of oyster mushroom waste extract, two batches of Soxhlet extraction using n-hexane as solvent are required. The procedure was then repeated by replacing hexane with ethanol as the solvent. Following extraction, a rotary evaporator (Heidolph Laborota 4000) was utilized to remove the solvent from the mixture of WMB lipids and solvents. This process took 10 to 15 mins at 50°C. The extracted extract of WMB was evaporated at room temperature to further remove the residual solvent and left to dry. The dried extract that was obtained was re-dissolved and stored at room temperature in a tightly sealed bottle to avoid oxidation for further analyses.

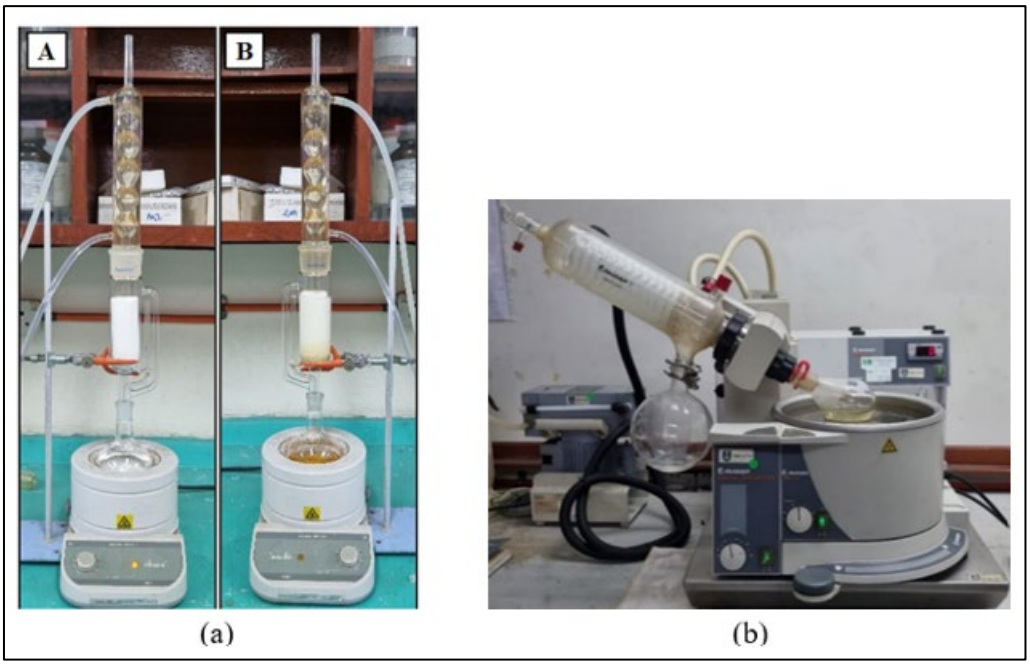

Figure 3.3 (a) Extraction of Extract from WMB through Soxhlet Extraction using Different Solvents. A: n-Hexane B: Ethanol (b) The Mixture of Lipid and Solvent was evaporated using a Rotary Evaporator (Heidolph Laborota 4000) after Extraction

3.3.3 Characterization of Oyster Mushroom Waste Extract

The extracts were characterized using a CHNS elemental analyzer (Thermo Scientific, FlashSmart CHNS) to measure the carbon content (percentage) present in the extracts. The analysis was done in triplicate. The mushroom waste extract using a suitable solvent, which was obtained from the elemental analyzer result, was then determined by its decomposition temperature using a Thermogravimetric analyzer (TGA) (Mettler Toledo) for the deposition of a-C using Chemical Vapor Deposition (CVD) later. It is measured to prevent the extract from decomposing early, which will affect the deposition of carbon during CVD.

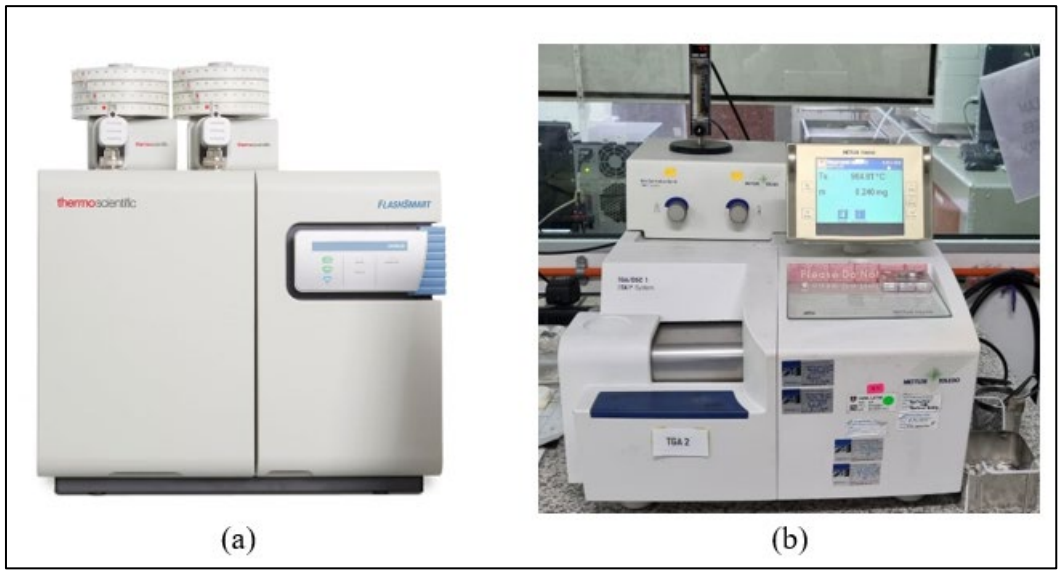

Figure 3.4 (a) CHNS Elemental Analyzer (Thermo Scientific, FlashSmart CHNS) (b) TGA (Mettler Toledo)

3.4 Deposition of Amorphous Carbon from Oyster Mushroom Waste Extract

3.4.1 Substrate Preparation

A well-cleaned p-type silicon wafer (100 mm)(thickness 525 microns, resistivity 0.001-0.005 Ω-cm), an n-type silicon wafer (100 mm)(thickness 525 microns, resistivity 0.001-0.005 Ω-cm), and glass were used as a substrate. The substrates were cut into a square shape of 2 cm x 2 cm. The substrates were cleaned using the Ultrasonic Cleaner (Hwanshin, Powersonic 405) with acetone for 15 mins and discarded later. After that, it was ultrasonically cleaned for 10 mins with deionized water. Next, use methanol for 15 mins and then discard. The substrates were then ultrasonically rinsed with deionized water for 10 mins. Using a diluted (0.5 M) hydrochloric acid (HCl), the substrates were sonicated for 2 mins and rinsed using deionized water. After being thoroughly cleaned, the substrates were placed in a desiccator with regulated humidity after being blow-dried with nitrogen (N) gas.

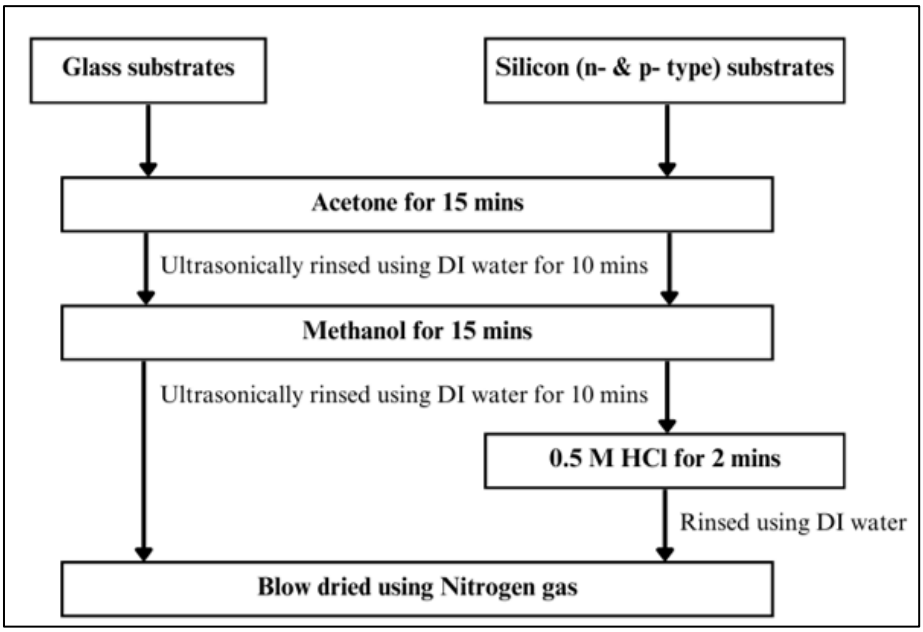

Figure 3.5 Flowchart of Substrate Preparation

3.4.2 Chemical Vapor Deposition (CVD) Preparation

Chemical Vapor Deposition (CVD) with a double furnace system was used to perform the depositions of a-C. Two furnaces (double furnace setup), a water bubbling system, a quartz tube, and a heater form the CVD system. One quartz tube, measuring 2.75 cm in inner diameter and 0.35 cm in wall thickness, was used for the CVD. With a length of 80 cm, the tube can tolerate temperatures of up to 1200°C. The furnace receives a maximum power of 1.5 kW from the direct current power source at a voltage of 240 V, which can be heated to 1100°C by the heater. The glass or silicon wafer, either n-type or p-type, was placed in the middle of the efficient heating element after being loaded into furnace 2. Concurrently, furnace 1 received the carbon precursor, or mushroom waste extract.


Figure 3.6 CVD with Double Furnace System

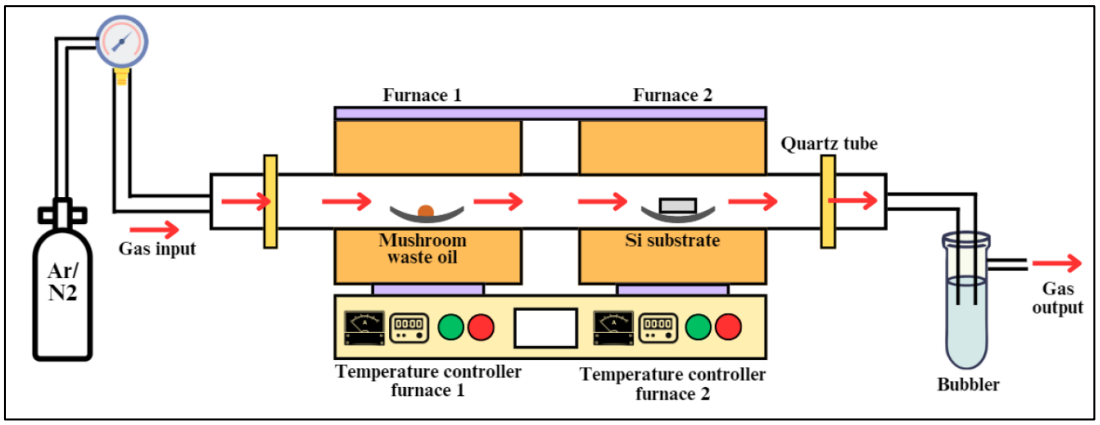

Figure 3.7 Schematic Diagram of CVD using Mushroom Waste Extract as the Precursor and Si/Glass as the Substrate

3.4.3 Undoped and Nitrogen-doped Amorphous Carbon Synthesis by CVD

The pure undoped and a-CN thin films were synthesized using the CVD technique. The process involves mushroom waste extract as the precursor and glass, n-type, and p-type silicon wafers as the substrate. For the pure, undoped a-C synthesis, the carrier Ar gas must be introduced into the furnace via a connection at the tube inlet. Furnace 1, which contains the carbon precursor, was heated from ambient temperature to the temperature required for deposition. The range of deposition temperature of the precursor was obtained from the results of TGA characterization of mushroom waste extract. The purpose of setting a specific temperature in furnace 1 is to provide sufficient energy for the mushroom waste extract particle to energize greatly, and as the transportation medium of the particle to furnace 2. Since this method involves 2 furnace systems, the temperature of the first furnace has to be lower than that of the second furnace in order for the pyrolysis process to occur. From the TGA's results, the temperature for the first furnace was 350°C.

In furnace 2, which contains substrates such as the use of n-type silicon and glass for undoped a-C, while p-type silicon for a-CN, the temperature was raised from ambient temperature to the desired temperature, with the maximum temperature of the CVD as the limit, which is 1100°C. It is also important to ensure that the temperature of furnace 2 is lower than the melting point of the substrates. The glass substrate was primarily employed for its optical properties because of its transparent nature, making it ideal for optical analysis. Meanwhile, the silicon substrate played a crucial role in this research as it improved the electrical conductivity of a-C due to its semiconducting

nature. This substrate also facilitates improved charge transport and reduced contact resistance, while also promoting better adhesion and strengthening sp^2 carbon bonding during deposition. Several samples were synthesized with different temperatures of furnace 2, the amount of precursor added into the alumina boat, and the flow rate of the gas were taken into account during the a-C synthesis. For the a-CN synthesis, the Ar gas was replaced by N gas, which acts as both carrier and dopant gas. This sample will be synthesized with different deposition temperatures and gas flow rates. The simplified synthesis parameter is tabulated in the Table 3.1 and Table 3.2. Each of the samples was synthesized for 30 mins.

Table 3.1
Synthesis of Undoped a-C Thin Films

Synthesis parameter	**Carrier gas**	**Substrate**	**Effect of amount precursor (ml)**	**Effect of deposition temperature (°C)**	**Effect of gas flow rate (sccm)**
Set 1	Argon	n-type Si & glass	1, 2, 3, 4	550	45
Set 2	Argon	n-type Si	2	650, 750, 850, 950	45
Set 3	Argon	n-type Si	2	850	25, 30, 35, 40, 45
Optimized	Argon	n-type Si	2	850	40

Table 3.2
Synthesis of Nitrogen-Doped a-C Thin Films

Synthesis parameter	**Carrier gas**	**Substrate**	**Effect of amount precursor (ml)**	**Effect of deposition temperature (°C)**	**Effect of gas flow rate (sccm)**
Set 4	Nitrogen	p-type Si	2	650, 750, 850, 950	40
Set 5	Nitrogen	p-type Si	2	850	25, 30, 35, 40, 45
Optimized	Nitrogen	p-type Si	2	850	35

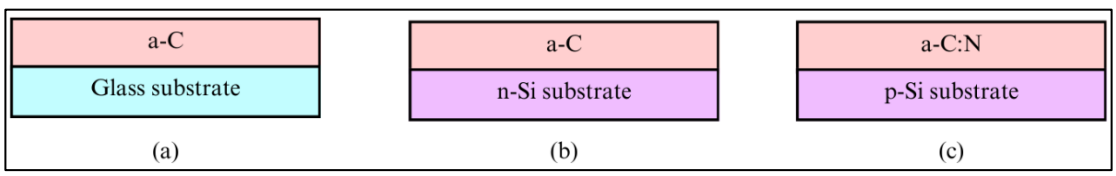

Figure 3.8 Thin Film Structure of Undoped a-C and a-CN on (a) Glass Substrate (b) n-type Si Substrate (c) p-type Si Substrate

Ensuring the environment of the furnace is free of the ambient gases, especially oxygen, is essential during the a-C's growth process. To avoid contamination, both ends of the tube connection need to be tightly secured. The flow meter was used to regulate the gases' flow rates (sccm). The exhaust gases were directly released into the fume hood, which subsequently expelled them through the chimney. This will enable the elimination of any undesirable and hazardous gases produced throughout the a-C production process. To oxidize any remaining carbon product, the furnace was heated to a high temperature of 1000°C after the synthesis was done.

For the thin film's characterization process, it will include the measurement of optical, structural, and electrical characteristics of the thin films. In order to assess the conductivity of the a-C thin films with and without N incorporation, gold (Au) was coated on the samples using a thermal evaporator. At the same time, the suitability of mushroom waste extract as the precursor of a-C synthesis was assessed. The metal contact is crucial in providing a current flow path inside the material for the measurement of current-voltage (I-V) analysis.

3.5 Characterization of Amorphous Carbon Thin Films

Raman spectroscopy, scanning electron microscopy (SEM), UV-Vis spectroscopy, energy dispersive x-ray spectroscopy (EDX), and current-voltage (I-V) measurement were used to characterize the deposited a-C and a-CN thin films. The optical, structural, and electrical characteristics of a-C and a-CN thin films were examined using these characterizations.

3.5.1 UV-Vis Spectroscopy

UV-Vis Spectroscopy (Perkin Elmer LAMBDA 750) was used to investigate the optical characteristics (e.g. optical transmittance and band gap) of the samples that were deposited on the glass substrates (Gesesse et al., 2020). Unfortunately, the optical characteristics cannot be investigated using a spectrophotometer when the samples are deposited on the silicon substrates. The spectroscopy employed in this investigation had wavelengths between 300 and 800 nm. The film's optical transmittance spectra and film thickness data were used to compute the absorption coefficient (α), which measures the amount of light with a certain wavelength or energy that may pass through a thin film

before being absorbed by it. Lambert's Law was used to determine the α of the a-C thin films using the following equation:

$$\alpha = \frac{1}{t}\ln(\frac{1}{T}) \tag{3.1}$$

Where T is the film's transmittance and t is its thickness. The optical band gap is the measurement of the gap between the extended state in the valence band and the conduction band. The optical band gap (E_g) for a-C were obtained by Tauc relationship, according to equation:

$$(\alpha hv)^{1/2} = B(E_g - hv) \tag{3.2}$$

where hv is the photon energy, B is the Tauc parameter, and α is the absorption coefficient. The optical gap, E_g is determined by the intercept of the Tauc's slope in the photon energy axis.

3.5.2 Surface Profiler

The thickness of a-C and a-CN thin films was measured using surface profilers, which operated by vertically moving a probe in contact with the sample surface and then scanning laterally across it at a controlled contact force. To obtain a clear step edge for the thickness measurement, a small region of the a-C and a-CN thin films is chemically etched using acid to remove the film locally and expose the substrate. The vertical displacement of the probe when crossing from the substrate to the unetched film area corresponds to the film thickness.

3.5.3 Raman Spectroscopy

The structural properties of a-C and a-CN thin films were investigated by Raman spectroscopy using an Ar ion laser with an excitation wavelength of 514 nm, which caused a number of photons to be scattered on the surface of the sample (Zhang et al., 2022b). This quick and non-destructive method can analyze the structure, internal stress, and the bond states of sp^2 and sp^3 in the a-C thin films. The excitation photons interact with the vibration of the molecular bonds during the scattering process, leading to the shift in the scattered photons' energy, also known as the Raman shift, which helps

to determine specific carbon materials. The Raman spectra that show two prominent peaks, the D and G peaks, indicate that the sample is a-C. The D peak can be located around 1350 cm^{-1} arises from the breathing modes of aromatic rings and is related to the defects in the carbon network. Meanwhile, the G peak, which can be seen around 1580 cm^{-1} corresponds to the stretching of carbon bonds and arises because of the vibration of the sp^2 bonded carbon atoms (Baqiya et al., 2025; Rana et al., 2025).

3.5.4 Scanning Electron Microscopy (SEM)

The a-C and a-CN thin films' exterior surface morphology and cross-sectional area were examined by scanning electron microscopy (SEM)(JSM-6360LA). It is a microscope that creates images by utilizing a concentrated electron beam to scan the surface of the samples. The sample's electrons interact with this beam, generating secondary electrons that are mostly used to image surface topography, which can reveal the microstructural characteristics of a-C and a-CN films (Zhang, 2013).

3.5.5 Energy Dispersive X-Ray Spectroscopy (EDX)

The elemental composition and distribution were investigated, as well as both quantitative and qualitative measurements, using EDX. Nearly every type of element listed in the periodic table can be found using this method. The analysis depends on identifying the distinctive X-rays that are emitted by the atoms in the thin films after they are subjected to a high-energy electron beam. Thus, producing a localized chemical analysis (Nurdiyanto, 2022).

3.5.6 Current-Voltage (I-V) Measurement

The current-voltage (I-V) measurement of a-C and a-CN thin films utilizes a two-point probe to analyze the electrical properties of the films. This technique relies on applying an electrical current through two electrodes (probes) contacting the sample and simultaneously measuring the voltage drop across these same two points. These enable the a-C and a-CN samples' electrical conductivity and resistivity to be determined. A thickness of 60 nm, gold (Au) was deposited on the samples by using a

thermal evaporator to create the ohmic contacts. The resistivity and conductivity of the deposited thin films were calculated according to the equation:

$$\rho = \left(\frac{V}{I}\right)\left(\frac{wt}{L}\right) \quad \text{in unit } \Omega.\text{cm} \tag{3.3}$$

$$\sigma = \frac{1}{\rho} \quad \text{in unit } \text{S.cm}^{-1} \tag{3.4}$$

Where ρ is the resistivity, σ is the conductivity, w is the width, t is the thickness of the a-C thin films, and L is the length between two electrodes.

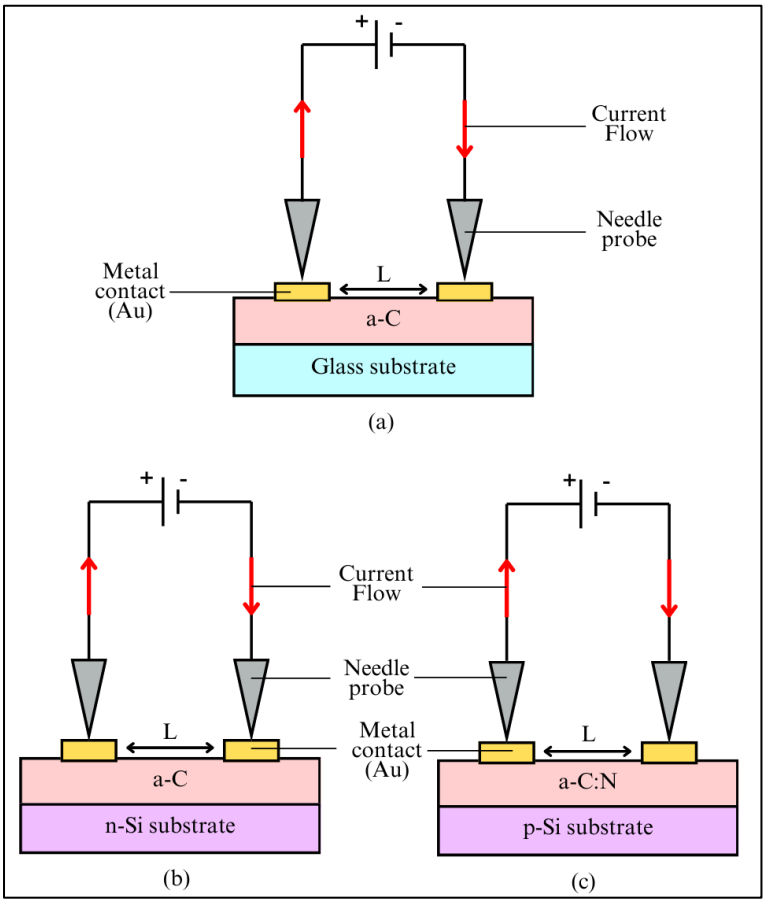

Figure 3.9 Schematic Diagram of I-V Measurement of a-C and a-CN Thin Films on (a) Glass Substrate (b) n-type Si Substrate (c) p-type Si Substrate

3.6 Chapter Summary

This chapter explained a detailed experimental procedure for the 3 phases in this study, including the preparation of the oyster mushroom waste, the deposition of a-C thin films from mushroom waste extract, and the characterization of undoped and N-

doped a-C thin films. This includes the extraction of oyster mushroom waste extract and its subsequent characterization. Next, the deposition of pure a-C and nitrogen doping of a-CN by using the CVD method, following the parameters such as the amount of precursor, deposition temperature, and gas flow rate. Then, the undoped a-C and a-CN thin films were characterized in terms of optical, structural, and electrical properties, and the detailed type of characterization used was provided.

CHAPTER 4
EXTRACTION OF OYSTER MUSHROOM WASTE EXTRACT

4.1 Introduction

In this chapter, we provide the experimental results of the extraction of oyster mushroom (*Pleurotus ostreatus*) waste extract by Soxhlet extraction using two different solvents, which are n-hexane and ethanol, and characterization of their extract by CHNS Analyzer and Thermogravimetric Analyzer (TGA) as described in Chapter 3. The analysis was conducted to investigate the suitability of the oyster mushroom waste extract as a carbon precursor for a-C synthesis. Also, to investigate the optimum decomposition temperature of oyster mushroom waste extract for the deposition of a-C to prevent the extract from decomposing early, which then affects the deposition process.

4.2 Characterization of Oyster Mushroom Waste Extract

4.2.1 Elemental Analysis of Oyster Mushroom Waste

The percentage of carbon (C), hydrogen (H), nitrogen (N), and sulphur (S) in the samples was ascertained using a CHNS Elemental Analyzer (Thermo Scientific, FlashSmart CHNS). This analysis was based on the complete combustion of the sample in a high-temperature furnace in an oxygen-rich environment, which converts the C, H, N, and S elements in the samples into measurable gases. These gases are then separated and quantified by using gas chromatography to determine the elemental composition accurately. However, in this study, we will prioritize the percentage of C, H, and N as the compounds are important in the synthesis of a-C, especially the C and N compounds. The higher the C percentage, the higher the suitability in producing a-C during the CVD process, and on top of that, the N content may assist in obtaining the N-doped a-C.

From Table 4.1, the compound percentage of the biomass of oyster mushroom waste is quite high, with the C percentage is 52.949%, the H percentage is 14.649%, the N percentage is 2.168%, and the S percentage is 2.641%. It can be seen that the carbon content in the oyster mushroom waste is high enough to supply the C to produce a-C using the CVD technique. Other than that, the oyster mushroom waste extract that was

extracted using n-hexane is higher compared to when using ethanol as a solvent. The C percentage for the extraction using n-hexane is 70.387%, the H percentage is 10.744%, the N percentage is 5.953%, and the S percentage is 0.000%. Meanwhile, the extraction using ethanol has a C percentage of 37.079%, an H percentage of 8.353%, an N percentage of 2.206%, and an S percentage is 0.000%.

Table 4.2 shows the yield extraction of oyster mushroom waste extract using both solvents for two batches of extraction. From the table, the yield extraction of the extract using ethanol is higher, with 7.48% and 11.53%, while n-hexane is 2.05% and 4.20%. Although the yield of extraction when using ethanol is higher, which is due to its high polarity index, it is not as efficient in dissolving certain non-polar compounds. Ethanol solvents are more suitable for extracting high concentrations of polar bioactive compounds with antioxidant and antimicrobial effects (Abd Aziz et al., 2021). In comparison, n-hexane, a non-polar solvent, is more effective in dissolving a non-polar compound such as fats, oils, and waxes, which are high in carbon content. Hexane is also more selective in extracting certain components from the extract, such as long-chain hydrocarbons, while ethanol may extract a broader range of compounds, including some lower molecular weight substances that have fewer carbon atoms, as they are polar solvents (Lee et al., 2024; Prasad et al., 2022).

In addition, hexane is easier to remove to get a pure extract due to its lower boiling point compared to ethanol, which may leave less residual solvent in the final product that contributes to a higher carbon content. Thus, it can be seen that when the oyster mushroom waste extract was extracted using n-hexane as a solvent, the compound percentage that is important to the synthesis of a-C was higher and better compared to ethanol, since they are inadequate for the extraction, since other materials, rather than the extract, were also extracted (Ferreira-Dias et al., 2003).

Table 4.1
CHNS Analysis of Oyster Mushroom Waste (Average ± Standard Deviation, n = 3)

Sample	**Elemental Analysis (%)**			
	Carbon (C)	**Hydrogen (H)**	**Nitrogen (N)**	**Sulphur (S)**
Biomass	52.949 ± 1.36	14.649 ± 0.90	2.168 ± 0.17	2.641 ± 0.24
Extract + n-hexane	70.387 ± 1.65	10.744 ± 1.02	5.953 ± 0.28	0.000 ± 0.00
Extract + ethanol	37.079 ± 1.38	8.353 ± 0.91	2.206 ± 0.18	0.000 ± 0.00

Table 4.2
Yield Extraction of Oyster Mushroom Waste Extract using n-Hexane and Ethanol as Solvents (for 2 Batches of Extraction)

Sample		Initial weight of biomass (g)	Weight of extract sample (g)	Extraction yield (%)
Extract + n-hexane	Batch 1	40.00	0.82	2.05
	Batch 2	40.00	1.68	4.20
Extract + ethanol	Batch 1	40.00	2.99	7.48
	Batch 2	40.00	4.61	11.53

4.2.2 Decomposition Temperature of Oyster Mushroom Waste Extract

The decomposition temperature was measured using TGA (Mettler Toledo). TGA was based on continuously measuring the mass change, either loss or gain, of the sample as it is subjected to a controlled temperature system. The sample is heated in a controlled atmosphere while a sensitive balance records the real-time mass variations, which correspond to physical or chemical processes such as volatilization, decomposition, oxidation, or combustion. This method is important to ensure that the oyster mushroom waste extract does not decompose early, which will affect the deposition process during CVD. From the CHNS result, the most suitable solvent used to extract oyster mushroom waste is n-hexane. Thus, this analysis is focused on the extract using n-hexane solvent. The graph shows that the best evaporation of the oyster mushroom waste extract is in the range of 330-360°C. This range can be the best guide in finding the optimum decomposition temperature of the oyster mushroom waste extract as a precursor in the synthesis of a-C. Thus, in this study, the decomposition temperature for the extract will be at 350°C, which is approximately the midpoint of the graph.

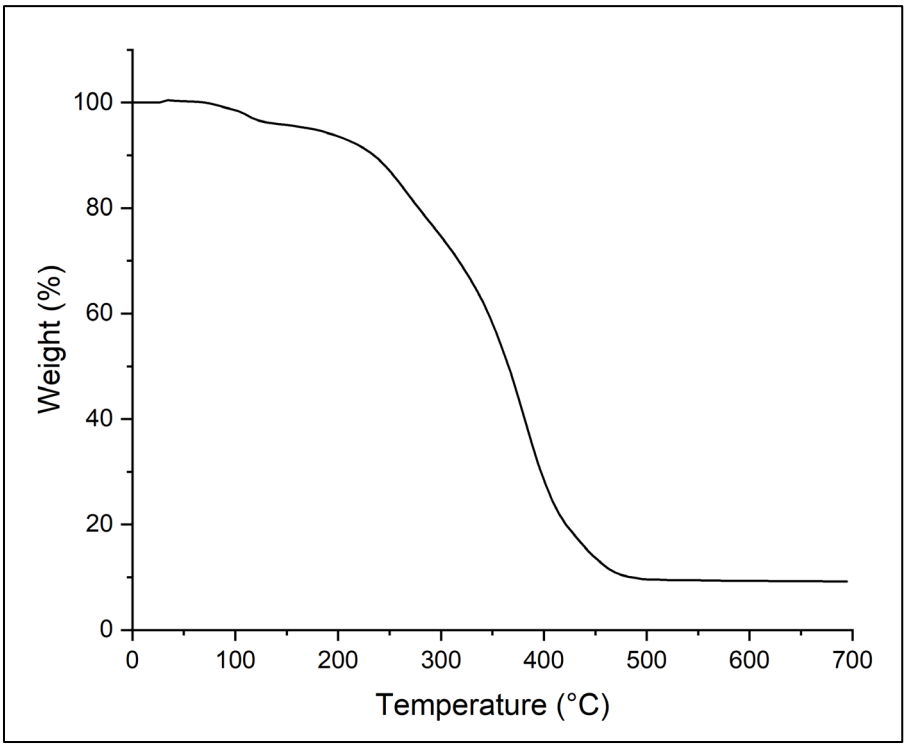

Figure 4.1 TGA Result of Oyster Mushroom Waste Extract

4.3 Chapter Summary

This chapter provides a detailed analysis of the extract derived from oyster mushrooms using two different solvents, ethanol and hexane, specifically for the CHNS analyzer. Among the two solvents, hexane has been shown to be the more advantageous choice for extracting the extract due to its higher carbon percentage. Subsequently, the extract extracted with hexane was analyzed using a TGA to determine the optimal decomposition temperature. The results presented in this chapter suggest that oyster mushroom waste extract is a promising candidate for use as a precursor, given its composition, which is essential for producing a-C films through the CVD technique.

CHAPTER 5
DEPOSITION OF AMORPHOUS CARBON THIN FILMS BY CVD TECHNIQUE

5.1 Introduction

This chapter contains the experimental results, along with the discussions of the research findings of amorphous carbon (a-C) thin films from oyster mushroom waste extract, which were extracted using n-hexane solvent, through the CVD technique as described in Chapter 3. The results included the structural and electrical properties that were obtained by Raman, I-V measurement, SEM, and EDX were discussed. Since the properties of a-C are highly influenced by the deposition technique and parameters, thus, the effect of the amount of carbon precursor, deposition temperature, and flow rate was studied.

5.2 Effect of the Amount of Precursor

In this sub-chapter, the synthesis of a-C on various amounts of carbon precursors on a glass substrate was employed using the CVD technique. The structural and electrical properties, along with optical properties, were discussed.

5.2.1 Optical Properties

To examine the optical characteristics of the a-C, UV-Vis spectroscopy was employed. The wavelengths used in this study ranged from 300 nm to 800 nm. Figure 5.1 displays the a-C thin film's optical transmittance. It is found that the transmittance has a value that is higher than 80% in the visible range, which is 390 – 790 nm. The thickness of a-C thin films has a significant impact on the transmittance, as seen in this study, where the percentage of transmittance decreased as the film thickness increased due to the increase in the amount of precursor. The films appear to be less transparent compared to the thinner films, as they are thicker (Liu et al., 2024; Mohagheghpour et al., 2016). The lowest thickness (92 nm) formed at 1 ml precursor has the highest

transmittance (89.95%), according to Table 5.1, whereas the thickest films (313 nm) had the lowest optical transmittance (80.81%).

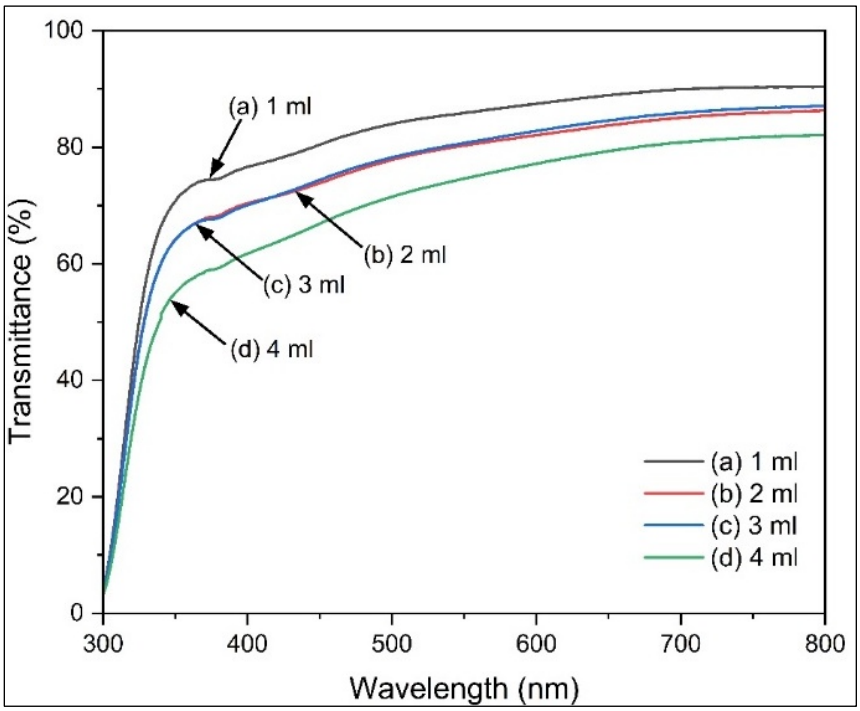

Figure 5.1 Graph of the Optical Transmittance against Wavelength of a-C Thin Films

As stated in Chapter 3, which provides examples of the Tauc relationship applications, Equation (3.2) was used to calculate the optical band gap (E_g) of the a-C films. It is mentioned in a previous study that the ratio of sp^2 and sp^3 bonds in the films are related to the band gap (Crespi et al., 2020). To obtain the E_g of the a-C films, the linear part of the curve at a=0 was extrapolated using the Tauc relation. Figure 5.2 shows the Tauc plot of $(\alpha hv)^{1/2}$ for a-C thin films against photon energy at different values of oyster mushroom waste extract. Li et al. (Li et al., 2018) claims that the optical characteristics are linked to the presence and relative ratio of the sp^2 and sp^3 carbon sites, where the band gap narrows as the sp^2 content increases are related.

Referring to Table 5.1, the a-C films' E_g was recorded at 0.80 eV when using 1 ml of the carbon precursor, reduced to 0.37 eV at 2 ml, and then gradually climbed to 0.57 eV and 0.65 eV as the amount of the carbon precursor grew to 3 ml and 4 ml, respectively. A number of variables, including the thickness of films, sp^2 clusters' sizes and contents, and the disordering of the π bonds, were identified as contributing to the shift in the band gap value (Li et al., 2020). In this case, samples that have a lower band

gap suggest a larger sp^2 cluster, whereas samples with higher band gaps can be thought of as having a smaller cluster of sp^2. This is because the size and connectivity of the conjugated pz electron network, which is also defined by the arrangement and clustering of sp^2 bonded carbon atoms, plays a crucial role in determining the band gap in carbon materials such as a-C (Baule et al., 2024; Li et al., 2020).

Generally, the amorphous network that governs the chemical, mechanical, electrical, and optical characteristics of a-C films is mostly made up of sp^2 and sp^3 carbon bonds. Although sp^2 carbon has both π and σ bonds; the band gap and conductivity were influenced by the extent of π electrons conjugation, which arises from overlapping pz orbitals of sp^2 carbon. This is due to the larger size of sp^2 clusters that enable greater electron delocalization, thus reducing the energy required for electronic transitions, and narrowing the band gap. Conversely, smaller or more isolated sp^2 limit the delocalization or only a few electrons conjugated, resulting in a wider band gap and low conductivity (Baule et al., 2024).

In this investigation, we find that the band gap rises as the transmittance percentage does. Nevertheless, we must take into account the sample thickness because the transmittance is influenced by the thickness, which rises with the precursor amount (Mohagheghpour et al., 2016). According to Table 5.1, the 1 ml sample exhibits the highest transmittance percentage (89.95%) and the biggest band gap (0.80 eV) despite being the lowest in thickness (92 nm) of all the samples. In contrast, the band gap (0.37 eV) and the transmittance percentage (85.07%) decreased for sample 2 ml as the thickness (115 nm) of the a-C films increased. As mentioned before, the larger conjugated sp^2 networks facilitate higher conductivity due to the increase in the π states density, further correlating with a reduced band gap (Kamaruzaman et al., 2020). But after 2 ml, the band gap progressively rises to 0.57 eV and 0.65 eV at 3 ml and 4 ml samples, respectively. The thickness rise is most likely the result of the film thickness being absorbed (Astinchap & Laelabadi, 2019).

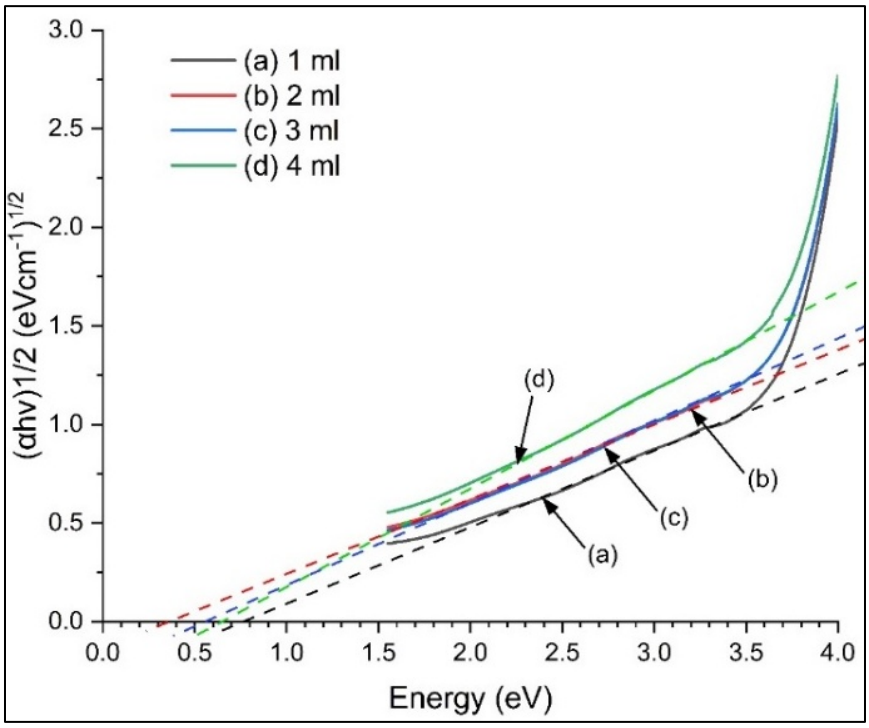

Figure 5.2 Graph of Tauc Plot against Photon Energy for a-C Thin Films

Table 5.1
Highest Transmittance and Optical Band Gap of a-C

Amount precursor (ml)	Highest transmittance (%)	Optical band gap (eV)	Average thickness (nm)
1	89.95	0.80	92
2	85.07	0.37	115
3	85.90	0.57	226
4	80.81	0.65	313

5.2.2 Structural Properties

5.2.2.1 Raman Spectroscopy

The structural characteristics of a-C were studied using Raman spectroscopy. This is because it can analyze how internal stress, bonding, and other factors behave in the a-C films (Dychalska et al., 2019; Orlando et al., 2021). Figure 5.3 shows the Raman spectra of the a-C thin films deposited with different concentrations of oyster mushroom waste extract ranging from 1000 cm^{-1} to 2000 cm^{-1}.

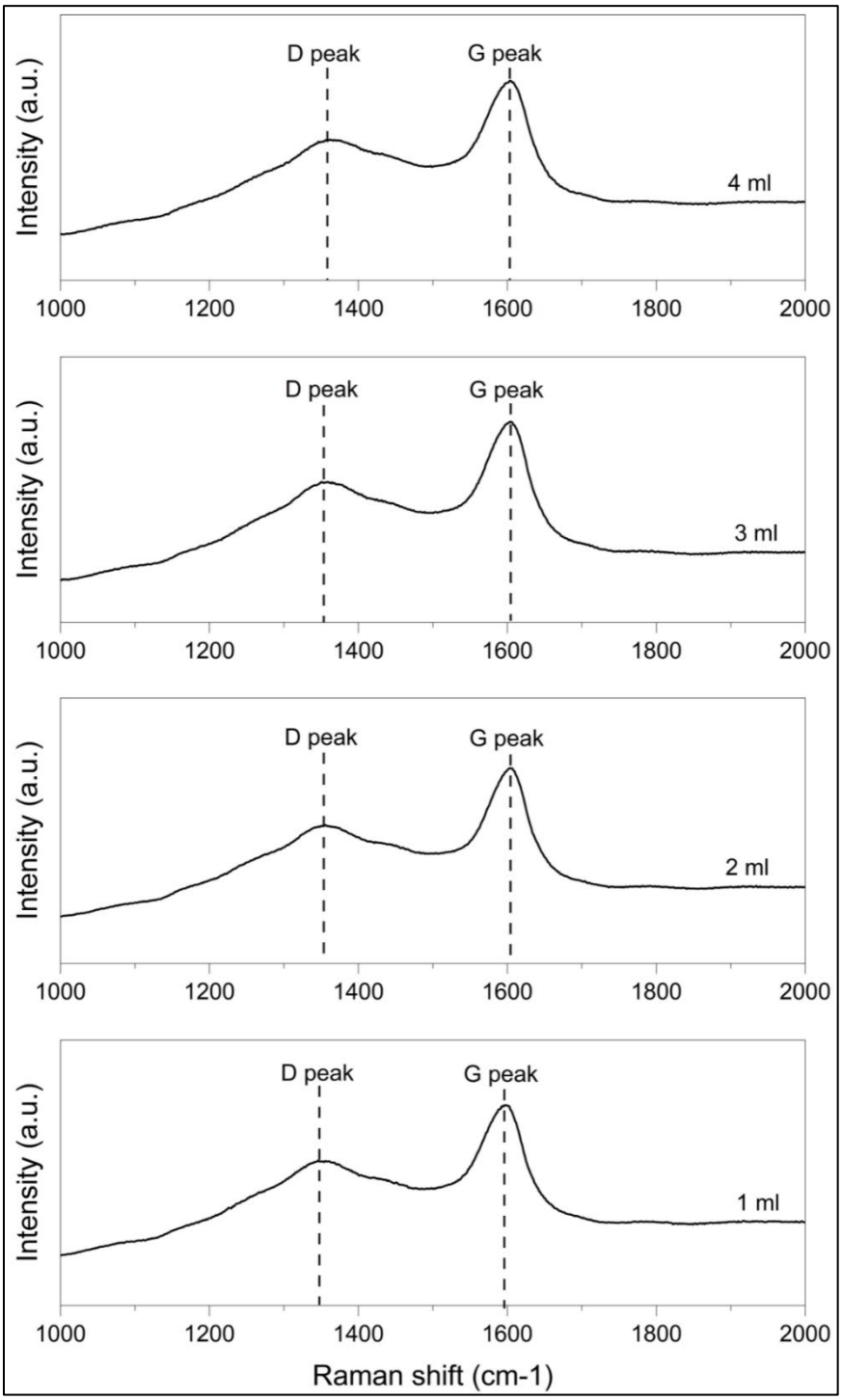

Figure 5.3 Raman Spectra of a-C Thin Films Deposited with Different Amounts of Precursor

The lack of 2D Raman peaks in the Raman spectrum suggests that the samples are a-C (Mitra et al., 2024). Typically, the Raman spectrum of a-C exhibits two broad peaks called the D peak, mostly found around 1350 cm^{-1} and the G peak, found around 1575-1600 cm^{-1}. The existence of these two peaks indicates the presence of sp^2 and sp^3 carbon bonding (Yuan et al., 2025). Theoretically, the D peak is thought to originate

from the breathing modes of aromatic rings and is associated with the defects in the carbon network, such as grain boundaries, edges, and structural disorder. The breathing modes that are not present in perfect graphite (graphene without defects) are activated by these defects. Concurrently, the G peak, which results from the vibration of sp^2 bonded carbon atoms, represents the stretching of carbon bonds in graphitic materials. It symbolizes the clustering of sp^2 sites in the carbon structure and the delocalization of π electrons' presence (Babu et al., 2016; Fadzilah et al., 2013). Consequently, a low intensity ratio I_D/I_G indicates a higher sp^3 content and lower sp^2 content. When the I_D/I_G value is higher, it is suggested that the sp^2 content for the samples is more clustered and ordered (Dychalska et al., 2019; Gabhi et al., 2020).

Moseenkov et al. (Moseenkov et al., 2023) have offered a thorough examination of the properties of several modes present in a-C in order to provide a straightforward explanation for the Raman spectra peaks for this material. The D peak (D_2 mode), which can be found at 1310-1390 cm^{-1} is due to the vibration of sp^2 carbon atoms in the rings with A_{1g} symmetry. This peak becomes active only when disorder or finite size effects, which means that these only appears in disordered (non-perfect) graphite or a-C. In the non-perfect graphite, this peak is weak; in a-C, it becomes prominent and broad. It is forbidden in perfect graphite. The G peak, which is located at 1575-1600 cm^{-1} corresponds to the E_{2g} symmetry and found in both rings and chains, all of sp^2 carbon systems, representing the in-plane carbon bond stretching. Furthermore, there are also modes that are associated with highly disordered and non-graphitic configurations of sp^2 bonded carbon in the a-C, called the modes D_3' that is located at 1450-1490 cm^{-1} and modes D_3'' situated at 1520-1555 cm^{-1}. D_4 mode is observed as a distinct peak near the G peak, with vibrations similar to the G peak.

The approximate locations of the D and G peaks in this investigation were found to be around ~1350 cm^{-1} and ~1600 cm^{-1}, respectively. As mentioned before, the existence of both peaks indicates that it is an a-C. The G peaks for the samples at 2-4 ml were moved somewhat over 1600 cm^{-1}, which is outside of the normal G peaks range, according to the data. It most likely happened as a result of the G peak position shifting upward due to the increase in compressive stress that occurs when thickness increases during deposition (Mohagheghpour et al., 2016). As shown in Figure 5.3 and Table 5.2, the Raman peak position was used to compute the I_D/I_G ratio for a-C thin films. The I_D/I_G ratio is used to determine the amount of sp^2 and sp^3 in the a-C films,

and the I_D/I_G ratio is computed to examine the modification in the carbon bonding structure in the film (Crespi et al., 2020; Zhang et al., 2022b). The results in Table 5.2 showed that the I_D/I_G ratio slightly decreased from 0.72 to 0.70 when the concentration of the precursor increased. This illustrates that while the high I_D/I_G ratio shows the film structure graphitization due to the sp^2 bonds, whereas the samples' low I_D/I_G ratio values show an increase in the crystallinity behavior in a-C films (Fadzilah et al., 2014b; Ono et al., 2024).

Table 5.2
D and G Peak Position, and Intensity Ratio of a-C Deposited at Different Amounts of Precursor

Amount precursor (ml)	**D peak position (cm^{-1})**	**G peak position (cm^{-1})**	**Intensity ratio (I_D/I_G)**
1	1345	1595	0.72
2	1356	1603	0.71
3	1359	1604	0.70
4	1361	1603	0.70

5.2.2.2 Scanning Electron Microscope (SEM)

The image of a scanning electron microscope (SEM) shows the surface morphology of a-C films deposited with different amounts of precursor, each observed at a magnification of 20 kx, as displayed in Figure 5.4. From the images, the surface morphology of the film when using 1 ml precursor is uniformly covered with fine, densely packed carbon nanoparticles, indicating a continuous and homogenous film. There are no noticeable defects or large agglomerates, and the particle size seems to be very small. At 2 ml precursor, a fine-grained a-C, with the surface that is still mostly uniform but somewhat less densely packed than in the 1 ml sample, can be detected.

Starting from a 3 ml sample, an obvious increase in particle size can be seen. There is a discernible rise in the quantity and size of carbon particles at the 3 ml sample. The morphology changes toward more noticeable granular features and larger clusters, indicating that agglomeration results from an increase in nucleation and growth sites with more precursor. Meanwhile, at 4 ml, the surface exhibits an obvious agglomeration and development of larger, irregular clusters and perhaps some fiber- or flake-like

structures. Some of the areas observed are rough and discontinuous, which might be possible due to the excessive precursor supply or incomplete carbon incorporation at this high dosage.

Thus, from the results, it can be concluded that a low amount of precursor (1-2 ml) leads to uniform, continuous, and fine-grained a-C coatings. The nucleation density is considered high, but the excessive clustering was prevented. However, as the amount of precursor increases, prominent aggregation, inhomogeneity, and increasing surface roughness are developed. Cluster growth is most likely the result of excessive carbon feeding the growth beyond the optimal.

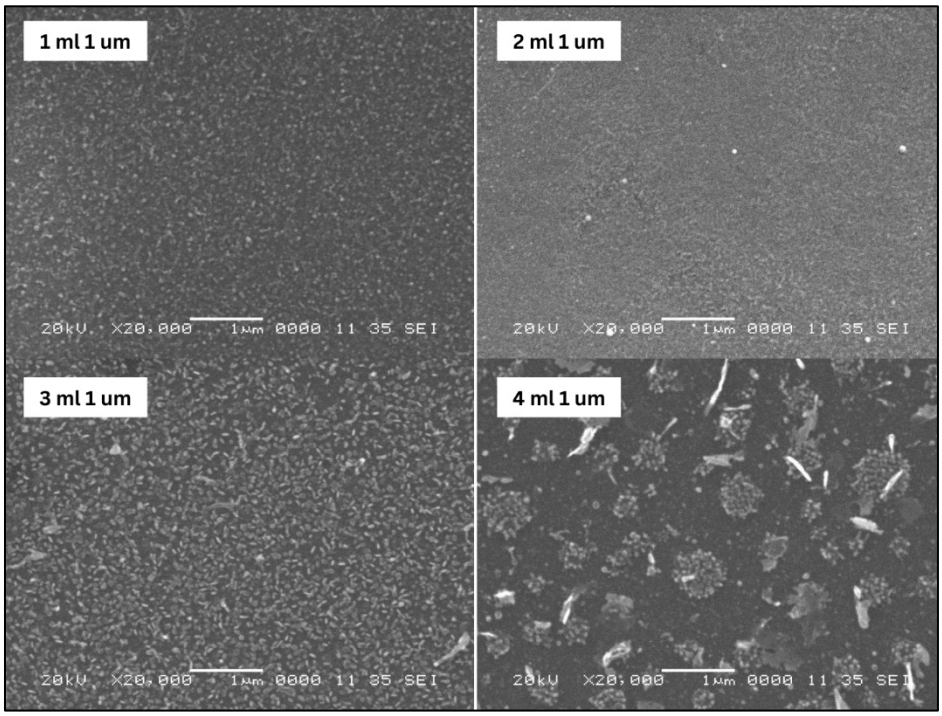

Figure 5.4 SEM Image of a-C Thin Films Deposited at Different Amounts of Precursor

5.2.3 Electrical Properties

5.2.3.1 Current-Voltage (I-V) Measurement

The measurement of current-voltage (I-V) was utilized to describe the electrical properties of the a-C thin film. On top of the film, the thermal evaporator deposited 99.9% Au, which is a well-known conductor and provides stable electrical contact with a-C, with a thickness of 60 nm to create the ohmic connections. As mentioned in

Chapter 3, Equations (3.3) and (3.4) were used to determine the resistivity and conductivity of the films.

In general, for a-C, it can be found the presence of the sp^2 and sp^3 carbon atoms. Carbon nanotubes, graphene, and graphite are examples of ordered sp^2 carbons that are conductors, while the sp^3 carbons that are ordered, such as diamonds, are insulators. Thus, the existence of sp^2 carbons that contain the π electrons influenced the conductivity of the a-C films (Gabhi et al., 2020). Figure 5.5 shows the I-V characteristic curve of a-C films. It is clear from the data that they were linear, meaning that at room temperature, the current gradually increased as the voltage increased. According to Kamaruzaman et al. (Kamaruzaman et al., 2020), a greater slope indicates a lower resistance.

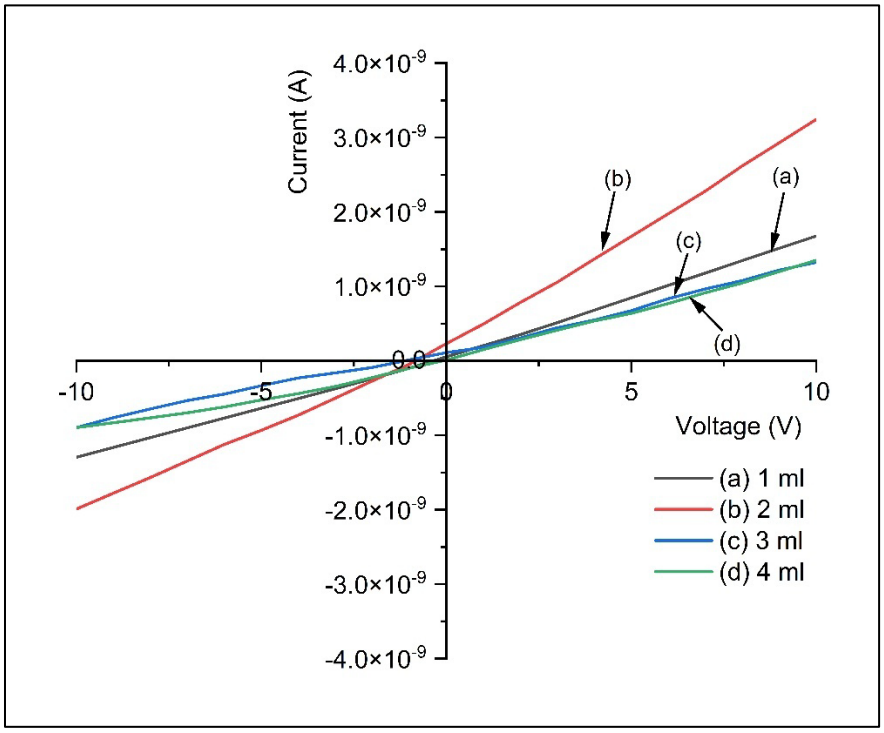

Figure 5.5 I-V Curve of a-C Thin Films Deposited at Different Amounts of Precursor

Table 5.3 and Figure 5.6 display the a-C films' conductivity as a function of the concentration of precursor. From 1.08×10^{-5} S. cm^{-1} to 1.51×10^{-5} S. cm^{-1} at 1 ml to 2 ml, the conductivity was observed to increase. At 3 ml, it greatly decreased to 3.18×10^{-6} S. cm^{-1}, and at 4 ml, it continued to fall to 2.44×10^{-6} S. cm^{-1}. The findings show that when the conductivity decreases and the resistivity increases, it indicates that the sp^3 content increases (Valcheva et al., 2023).

Electrical conductivity is also influenced by the carrier mobility, density, and size of sp^2 cluster. As the film thickness (from 92 nm to 313 nm) increases along with the compressive stress during deposition, the number of π states of the sp^2 sites may decrease. In addition, the lower band gap in a-C arises from an increased size and connectivity of sp^2 clusters, resulting in increasing conductivity. This is due to the sp^2 clusters that formed a larger π-conjugated networks, which enable electron excitation across smaller energy differences more easily. To simplify, a smaller band gap means electrons require less energy to move from the valence to the conduction band, thus increasing conductivity due to an enhanced delocalized π states' density (Jhaa et al., 2023; Mohagheghpour et al., 2016). It is found that 2 ml is the ideal quantity of oyster mushroom waste extract in order to create a-C thin films since the electrical conductivity was the largest at this volume.

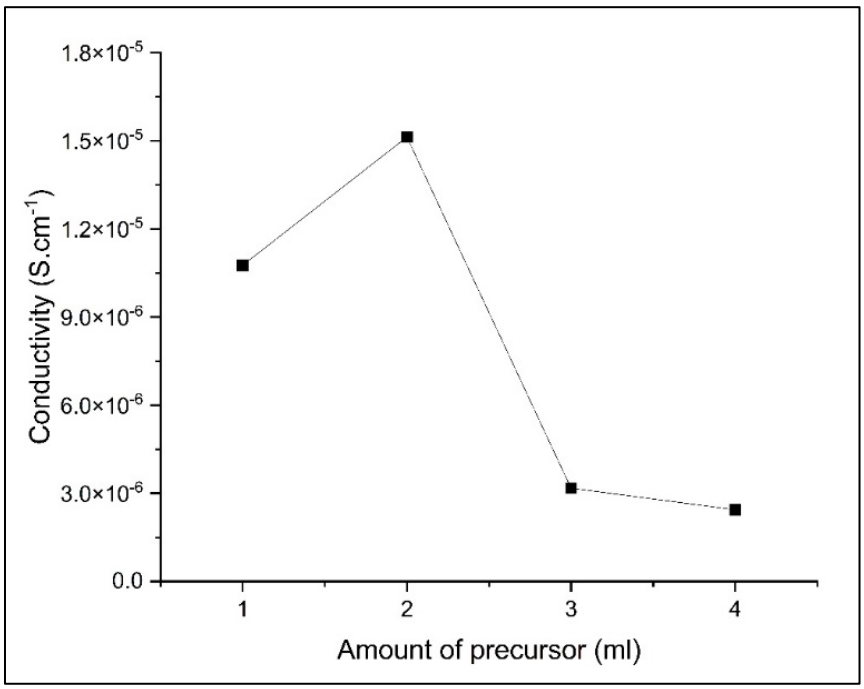

Figure 5.6 Electrical Conductivity of A-C Thin Films Deposited at Different Amounts of Precursor

Table 5.3
Electrical Resistivity and Conductivity of a-C Deposited at Different Amounts of Precursor

Amount precursor (ml)	**Resistivity (Ω.cm)**	**Conductivity ($S.cm^{-1}$)**
1	9.29×10^4	1.08×10^{-5}
2	6.61×10^4	1.51×10^{-5}

3	3.15×10^5	3.18×10^{-6}
4	4.10×10^5	2.44×10^{-6}

5.3 Effect of Deposition Temperature

Amorphous carbon growth has been previously demonstrated on different amounts of precursor. The optimum amount was found to be 2 ml with a 350°C precursor/oyster mushroom waste extract temperature. In this parameter, the deposition temperatures of a-C were varied from 650°C to 950°C by 100°C increments, which were synthesized on silicone substrates using the CVD technique. The structural and electrical characteristics were investigated.

5.3.1 Structural Properties

5.3.1.1 Raman Spectroscopy

Figure 5.7 displays the Raman spectra of a-C thin film deposition ranging from 1000-2000 cm^{-1} at various deposition temperatures. The absence of 2D and the presence of D and G peaks only, confirming the characteristics of the thin films, which are a-C (Mitra et al., 2024). Due to this, there is the existence of the sp^2 and sp^3 carbon bonds in the a-C films. As mentioned before, the first peak (D peak) appears only when there is disorder in the a-C, including defects, edges, or finite cluster size. Whereas, the second peak (G peak) reflects the degree of graphitic order and sp^2 bonding configuration (Babu et al., 2016; Chen et al., 2015; Fadzilah et al., 2013). Thus, the I_D/I_G ratio that has a lower value indicates that it contains a smaller sp^2 clusters. Likewise, the higher I_D/I_G ratios exhibit larger sp^2 clusters (Dychalska et al., 2019; Gabhi et al., 2020).

As typical for a-C films, the D and G peaks in our investigation are situated roughly at 1350~ and 1590~ cm^{-1}, respectively. Compared to the normal range of G peaks, which is between 1575 and 1600 cm^{-1}, the G peaks for the samples at 650°C presented in Table 5.4 are somewhat higher than 1600 cm^{-1} (Moseenkov et al., 2023). The I_D/I_G ratios that were calculated using both of the Raman peaks with varying deposition temperatures are shown in Table 5.4. This ratio demonstrates how the carbon bonding structures have modified as a result of the existence of sp^2 and sp^3 in the

sample. As the deposition temperature rises, the data shows that the I_D/I_G ratios rise from 0.70 to 0.80, indicating an increase in the sp^2 bonds that affect the structure's graphitization (Babu et al., 2016; Ono et al., 2024; Torres et al., 2024). The slight decrease in I_D/I_G ratio at 750°C might be due to the changes in the film's microstructure during deposition. At lower 650-750°C suggests smaller sp^2 cluster while at higher 850-950°C suggests enhanced the graphitization and clustering of sp^2 bonds.

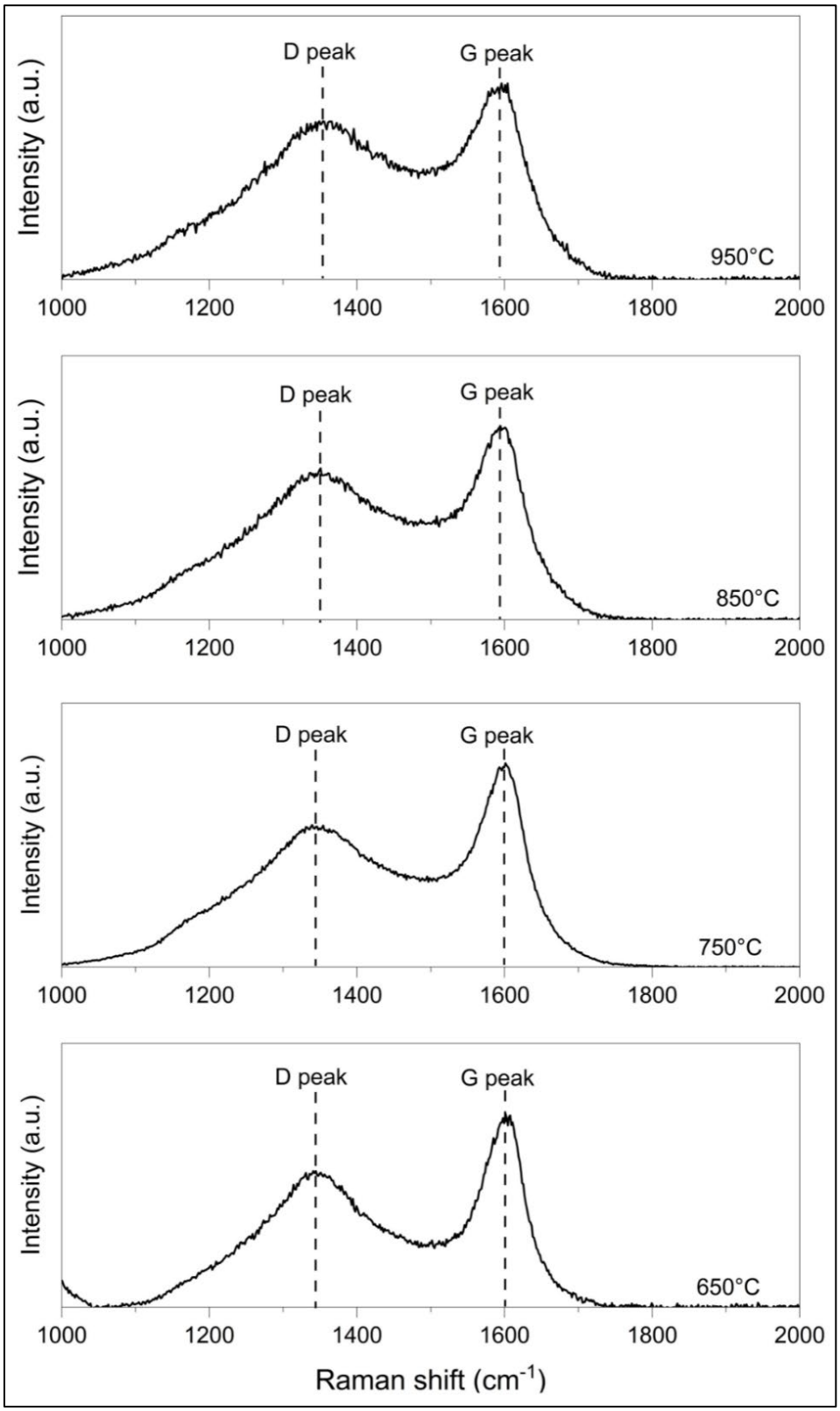

Figure 5.7 Raman Spectra of a-C Thin Films Deposited at Different Deposition Temperatures

Table 5.4
D and G Peak Position, and Intensity Ratio of a-C Deposited at Different Deposition Temperatures

Deposition temperature (°C)	D peak position (cm^{-1})	G peak position (cm^{-1})	Intensity ratio (I_D/I_G)
650	1344	1601	0.70
750	1345	1599	0.70
850	1350	1594	0.78
950	1354	1595	0.80

5.3.1.2 Scanning Electron Microscope (SEM)

Figure 5.8 shows the SEM images of a-C films that were deposited at various temperatures. The surface morphology of the films was examined from the images. It is a little challenging to determine whether or not it is a carbon particle at 650°C due to the surface not exhibiting the surface of a typical a-C film, which is an obvious spherical carbon particle. However, according to the findings of the EDX analysis, at 650°C, indicates that there are no carbon content was detected, as the carbon percentage for this sample is 0.00%. These could be the causes of the SEM's inability to accurately scan the 650°C sample's image. Another possibility is that the particles may not be visible at the current magnification and resolution (µm scale) since the thickness of the sample is comparatively smaller, at 190 nm (Ishak et al., 2013). At 750°C, the particles seem somewhat bigger and distinct, with each spherical feature being better defined. This may suggest enhanced mobility and aggregation as surface diffusion improves with temperature (Li et al., 2020).

For the samples deposited at 850°C, the particle size is shown to rise with notably more prominent and well-separated spherical particles, also a visible increase in agglomeration. The nucleation density was decreased as larger clusters formed connected islands rather than a homogeneous film. In contrast, the particles show relatively big and sparsely dispersed carbon spheres for samples heated to 950°C. As the particle size distribution widens and large agglomerates predominate, the image suggests a surface roughness and decreased homogeneity (Addie et al., 2022; Li et al., 2020).

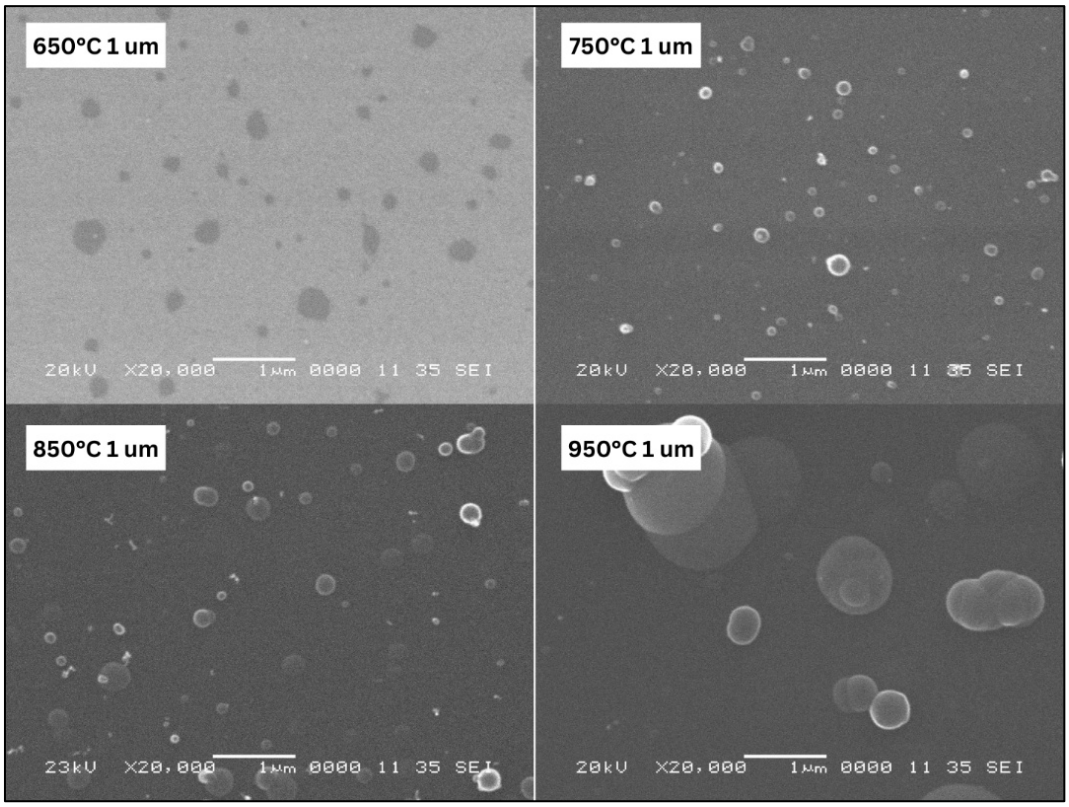

Figure 5.8 SEM Image of a-C Thin Films Deposited at Different Deposition Temperatures

5.3.1.3 Energy Dispersive X-Ray Spectroscopy (EDX)

Energy Dispersive X-ray Spectroscopy (EDX) measures characteristic X-ray signals emitted from elements in the sample when bombarded by a concentrated electron beam, providing elemental composition in percentage of weight and atomic (Robaiah et al., 2023). The main elements that make up the composition of a-C that is present on the silicon substrate are silicon (Si), carbon (C), and oxygen (O). The presence of the C element indicates a successful carbon deposition process, while the presence of the Si element usually comes from the silicon substrate. The O elements are part of the potential surface oxidation or residual oxygen.

From Table 5.5, it can be seen that as the temperature increases, the C content percentage increases from 0.00% to 75.80%. It also shows that other elements, like the O and Si elements, decrease as the deposition temperatures increase. According to the findings, the C element is 0.00% at 650°C, which might be due to the thickness of the films (190 nm), or the films are not fully covering the substrate, which allows a strong

Si element signal from the substrate beneath the film. Since there is no carbon detected, this suggests insufficient deposition or incomplete carbon film formation.

Then, at 750°C, the C elements show a slight increase to 0.26%, but still mostly the signal of the Si substrate dominates, which means that the carbon deposition has begun, but remains thin or sparse. The C element further increases to 26.18% at 850°C while the O and Si percentage decreases, indicating a clearer C film forming, and the film thickness or coverage improves. Meanwhile, at 950°C, the C content dominates overwhelmingly with 75.80%, indicating a thick a-C layer and higher C coverage, resulting in the reduction in the Si element's signal.

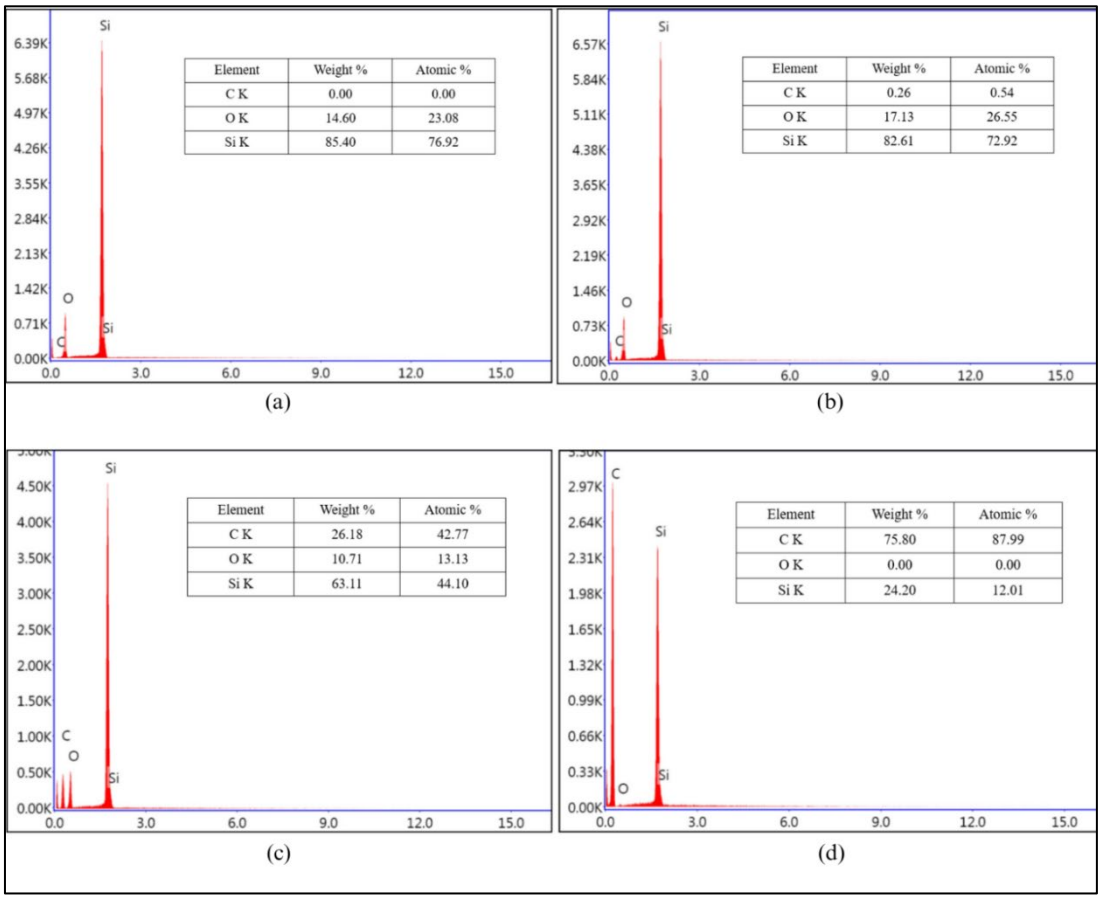

Figure 5.9 EDX Data of a-C Thin Films Deposited at Different Deposition Temperatures (a) 650°C (b) 750°C (c) 850°C (d) 950°C

Table 5.5
EDX Data of a-C Deposited at Different Deposition Temperatures

Deposition temperature (°C)	Elements	Weight %	Atomic %
650	C K	0.00	0.00
	O K	14.60	23.08
	Si K	85.40	76.92
750	C K	0.26	0.54
	O K	17.13	26.55
	Si K	82.61	72.92
850	C K	26.18	42.77
	O K	10.71	13.13
	Si K	63.11	44.10
950	C K	75.80	87.99
	O K	0.00	0.00
	Si K	24.20	12.01

5.3.2 Electrical Properties

5.3.2.1 Current-Voltage (I-V) Measurement

For the I-V characterization, a 2-point probe method was employed to assess the electrical characteristics of undoped a-C films. By using a thermal evaporator, Au was deposited on top of the film for ohmic contacts. As mentioned in Chapter 3, Equations (3.3) and (3.4) were utilized to investigate the resistivity and conductivity of the films.

Typically, it is the sp^2 hybridized carbon atoms, with their delocalized π electrons, that facilitate electrical conduction in a-C films, which consist of both sp^2 and sp^3 carbon bonds (Gabhi et al., 2020). Figure 5.10 presents a linear graph operating within the voltage range of -10V to 10V, suggesting optimal ohmic behavior. It is proposed that a steeper slope correlates with reduced resistance (Kamaruzaman et al., 2020). A surface profiler was employed to analyze the thickness of the samples. The results obtained were tabulated in Table 5.6, indicating that thickness increases as the deposition temperature increases. This could be attributed to the elevated temperature providing greater energy to carbon atoms, enhancing their mobility on the substrate, which promotes more efficient nucleation and growth, as well as intensifying the

adhesive forces between carbon particles and the substrate, resulting in thicker films (Li et al., 2020).

The electrical conductivity of a-C films deposited at various deposition temperatures was determined using the I-V measurement data and illustrated in Figure 5.11 and Table 5.6. The conductivity was observed to rise from 1.71×10^{-6} S.cm^{-1} at 650°C to 1.57 S.cm^{-1} at 750°C. The lower temperature is linked to a higher presence of sp^3 states, which results in a reduced conductivity value (Pradhan & Sharon, 2007). Subsequently, at 850°C, there was a significant increase in conductivity to 1.41×10^{2} S.cm^{-1}. The rise in deposition temperature indicates an increase in sp^2 content and their π states, leading to higher conductivity and lower resistivity. At a temperature of 950°C, the conductivity was recorded at 6.44×10^{1} S.cm^{-1}, indicating a reduction. This phenomenon can be attributed to the changes in the films' microstructure, which impacts electron mobility, leading to a decrease in conductivity (Dayana et al., 2012; Ishak et al., 2013). Additionally, the transition from sp^2 to sp^3 carbon bonds may elevate the compressive stress, contributing to a reduction in the electrical conductivity of the films (Kamaruzaman et al., 2012; Mohagheghpour et al., 2016).

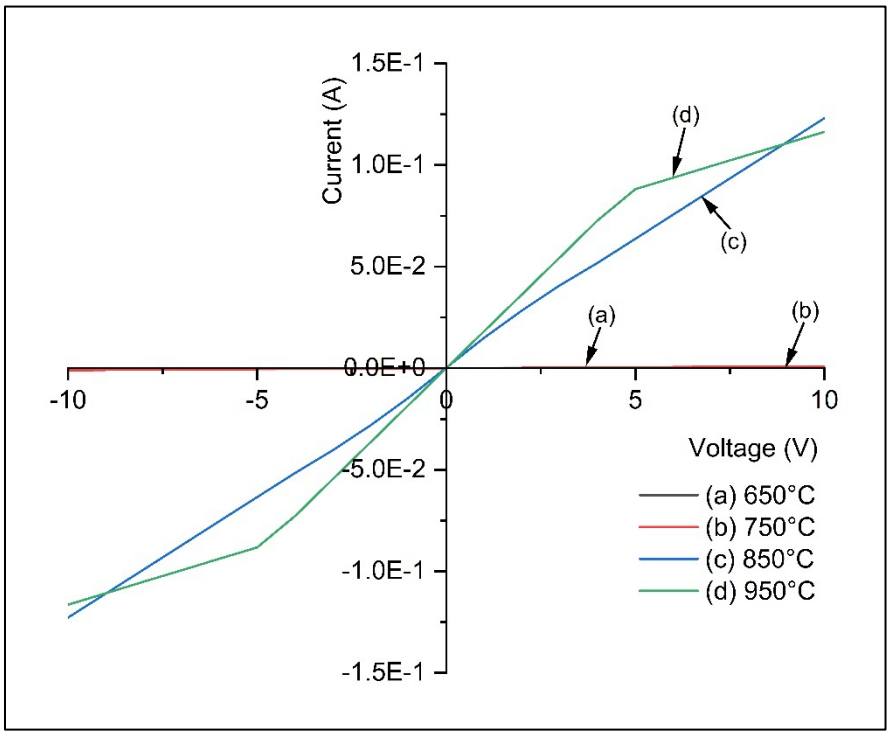

Figure 5.10 I-V Curve of a-C Thin Films Deposited at Different Deposition Temperatures

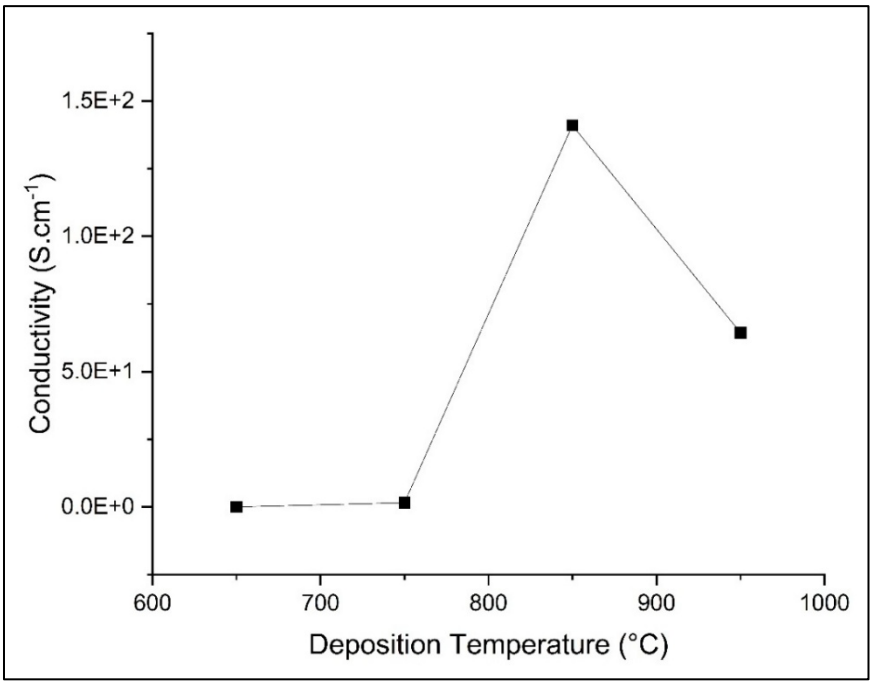

Figure 5.11 Electrical Conductivity of a-C Thin Films Deposited at Different Deposition Temperatures

Table 5.6
Electrical Resistivity, Conductivity, and Thickness of a-C Deposited at Different Deposition Temperatures

Deposition temperature (°C)	**Resistivity (Ω.cm)**	**Conductivity ($S.cm^{-1}$)**	**Average thickness (nm)**
650	5.86×10^{5}	1.71×10^{-6}	190
750	6.36×10^{-1}	1.57	410
850	7.09×10^{-3}	1.41×10^{2}	590
950	1.55×10^{-2}	6.44×10^{1}	1410

5.4 Effect of Gas Flow Rates

The growth of a-C has been previously investigated at different amounts of precursor and deposition temperatures. The optimum parameter for now was found to be 2 ml at 850°C deposition temperature with a fixed 350°C precursor temperature for 30 mins deposition. In this parameter, the flow rate of carrier gas, which is Argon gas, was employed with varied rates from 25 sccm to 45 sccm by 5 sccm increments. The structural and electrical properties of the a-C on a silicon substrate were investigated.

5.4.1 Structural Properties

5.4.1.1 Raman Spectroscopy

The results were obtained by Raman spectroscopy, where the samples were scanned ranging from 1000 cm^{-1} to 2000 cm^{-1}. In Figure 5.12, the Raman spectrum of the a-C thin films that were grown on a silicon substrate at 850°C deposition temperature with different flow rates from 25 sccm to 45 sccm was displayed. From the results, it can be seen that there are two well-separated asymmetric peaks located around ~1360 cm^{-1} and ~1600 cm^{-1}, which are known as D and G peaks, respectively. Since these two peaks are present in a typical a-C, their occurrence verifies that the samples are a-C. Moseenkov et al. (Moseenkov et al., 2023) stated that in-plane vibrations with the E_{2g} symmetry that involved the movement of the stretching of the sp^2 carbon pairs are represented by the G peak. Meanwhile, the D peak is associated with the disorder of the carbon because of the A_{1g} symmetry vibration. Furthermore, these two peaks demonstrate that the a-C thin films include a combination of sp^2 and sp^3 bonds.

In this study, it can be seen that the D and G peak position at 40 sccm has a higher wave number, 1361 cm^{-1} and 1601 cm^{-1}, respectively. This behaviour implies that the thin films have more sp^2 carbon atoms and less bond angle disorder (Rusop et al., 2006). The intensity ratio (I_D/I_G) was calculated and tabulated in Table 5.7. This ratio was calculated to estimate the content of sp^2 and sp^3 in the a-C thin films (Crespi et al., 2020; Zhang et al., 2022b). In Table 5.7, as the flow rate increases, the I_D/I_G ratio value rises from 0.69 to 0.78, demonstrating that the sp^2 content in the a-C thin films is increasing.

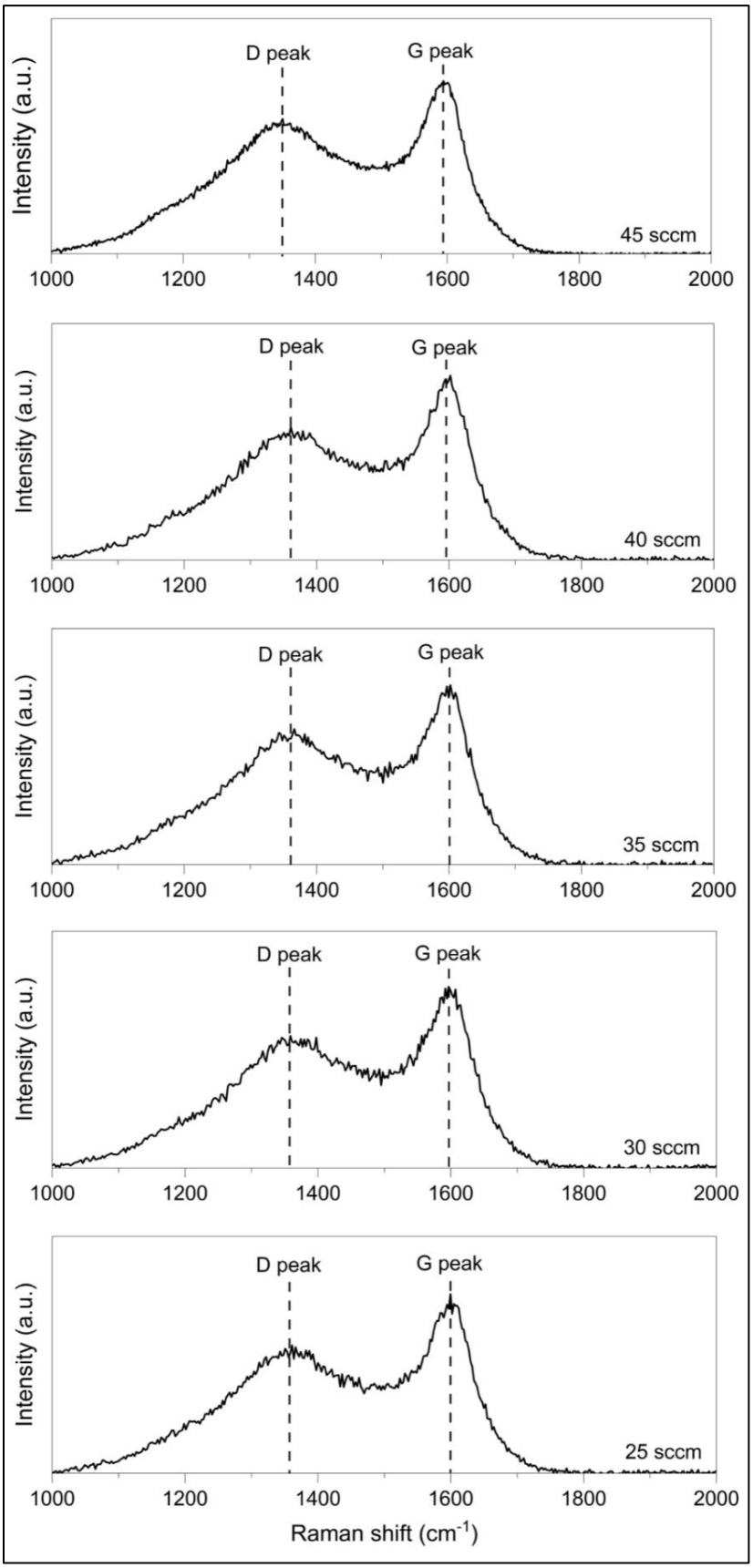

Figure 5.12 Raman Spectra of a-C Thin Films Deposited at Different Gas Flow Rates

Table 5.7
D and G Peak Position, and Intensity Ratio of a-C Deposited at Different Gas Flow Rates

Flow rate (sccm)	D peak position (cm^{-1})	G peak position (cm^{-1})	Intensity ratio (I_D/I_G)
25	1350	1599	0.69
30	1358	1596	0.73
35	1342	1596	0.74
40	1361	1601	0.73
45	1350	1594	0.78

5.4.1.2 Scanning Electron Microscope (SEM)

The SEM image of the deposited a-C films at various flow rates is shown in Figure 5.13. According to the results, the image shows that the silicon substrate is covered with circular particles that range in size from nano to micro. A few larger, isolated spherical particles are visible when the films are formed at 25 sccm. The scattered distribution of the particles further suggests that the C particles are not homogeneous. The particle density increases at 30 sccm, where the distribution becomes more uniform but remains sparse. The smaller nucleation density may be the cause of the formation of larger particles from both flow rates (25 and 30 sccm). Nevertheless, due to the current magnification and resolution, it is somewhat challenging to recognize if it is agglomerated or not because more particles are obscured (Ishak et al., 2013).

At 35 sccm, a more noticeable ring-like structure and a discernible rise in the number of carbon particles can be seen. At 40 sccm, there is an obvious rise in the number of ring structures and homogeneity of C particles. This would suggest that the nucleation density has increased, resulting in more uniform particles but limiting individual particle growth. This implied enhanced diffusion and vapor transport during deposition. The highest flow rate in this investigation, 45 sccm, exhibits the highest particle density as the field is densely populated with particles, showing a clear trend of particle agglomeration and possible overlap. There was a combination of large and small particles with more noticeable ring-like and spherical shapes. These results demonstrate that increasing gas flow rate enhances particle nucleation and surface

coverage, but reduces average particle size and increases the risk of particle agglomeration.

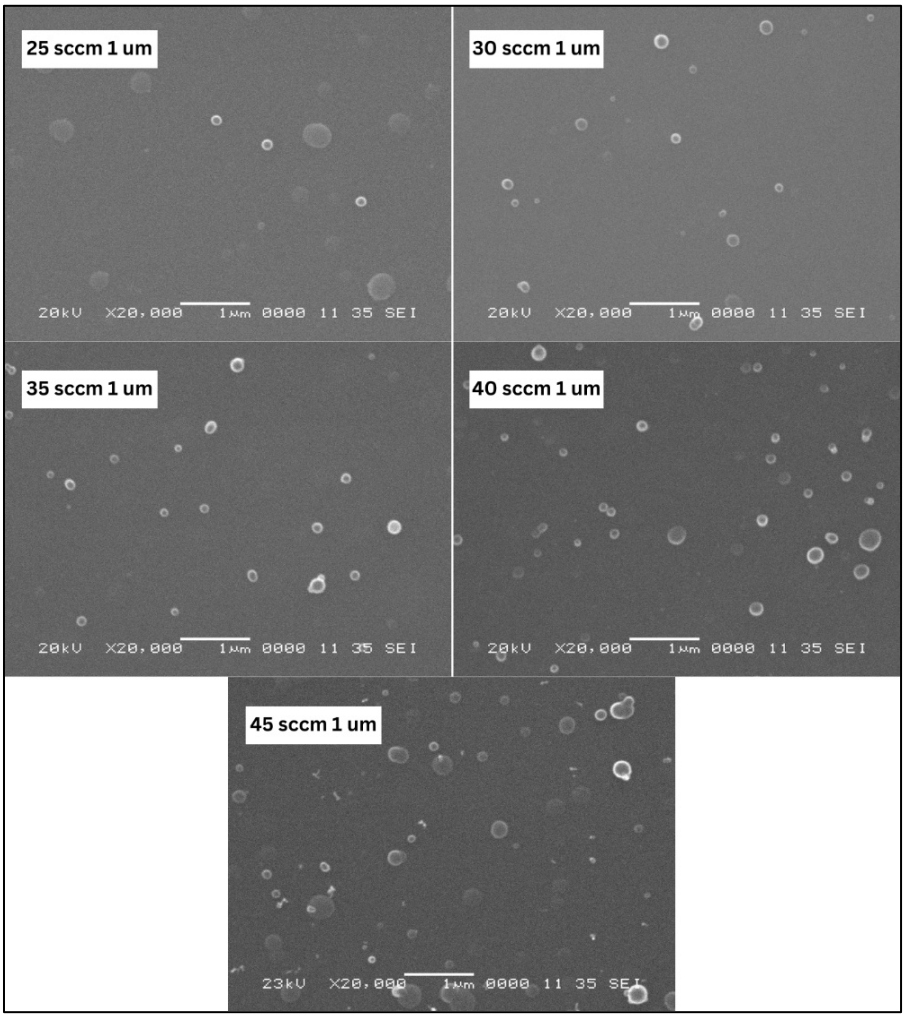

Figure 5.13 SEM Image of a-C Thin Films Deposited at Different Gas Flow Rates

5.4.1.3 Energy Dispersive X-Ray Spectroscopy (EDX)

Figure 5.14 shows the elemental composition of a-C films, which consists of C, O, and SI elements. From the Table 5.8, it confirms the presence of C elements on the substrate, validating the successful deposition of a-C films. For Si and O elements, their existence may be due to the substrate signal and surface oxidation or residual oxygen incorporation during deposition, respectively. At 25 sccm, the C content is moderately high with 20.33%, with lower Si and moderate O content, indicating decent C particle coverage on the substrate. The C content drops to 11.79% at 30 sccm, then slightly increases to 12.48% at 35 sccm and decreases to 11.26% at 40 sccm, with higher Si and

O percentages. This suggests the samples have thinner or less dense carbon layers, which allow more substrate signal through. At 45 sccm, the C content increases significantly, 26.18%, with lower Si contents, implying a thicker or denser C film and better coverage. The inconsistency of the C element of all samples might be due to the spot scan area, where it might hit a certain region that has more C clusters, or hit a thin area that has low content.

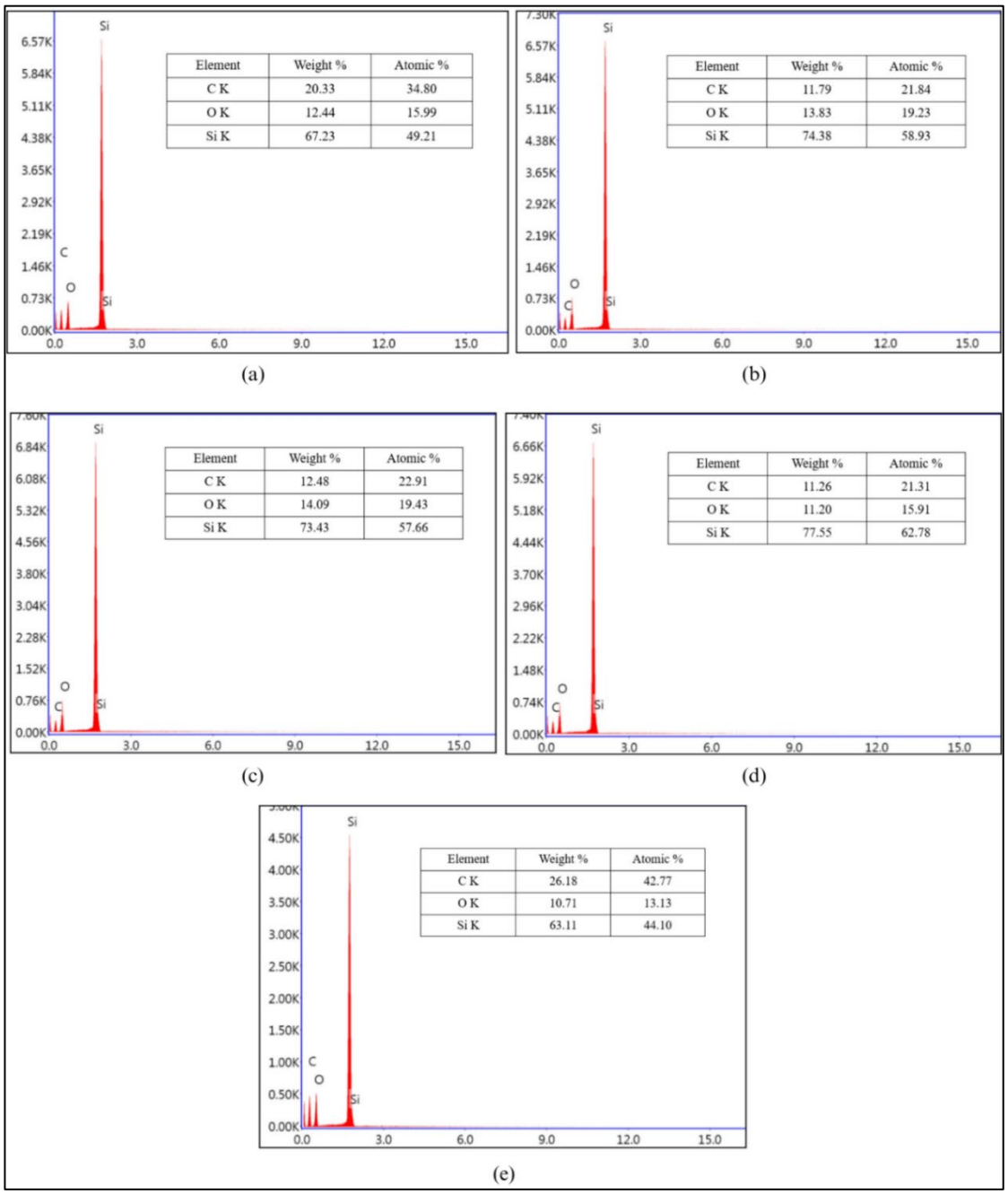

Figure 5.14 EDX Data of a-C Thin Films Deposited at Different Gas Flow Rates (a) 25 sccm (b) 30 sccm (c) 35 sccm (d) 40 sccm (e) 45 sccm

Table 5.8
EDX Data of a-C Thin Films Deposited at Different Gas Flow Rates

Flow rate (sccm)	Elements	Weight %	Atomic %
25	C K	20.33	34.80
	O K	12.44	15.99
	Si K	67.23	49.21
30	C K	11.79	21.84
	O K	13.83	19.23
	Si K	74.38	58.93
35	C K	12.48	22.91
	O K	14.09	19.43
	Si K	73.43	57.66
40	C K	11.26	21.31
	O K	11.20	15.91
	Si K	77.55	62.78
45	C K	26.18	42.77
	O K	10.71	13.13
	Si K	63.11	44.10

5.4.2 Electrical Properties

5.4.2.1 Current-Voltage (I-V) Measurement

A 2-point probe method was employed to carry out an I-V measurement to assess the electrical characteristics. Figure 5.15 displays the I-V curve for the a-C thin films deposited at different gas flow rates. The graph appears to exhibit a linear relationship within the voltage range of -10V to 10V, suggesting that the results demonstrate ohmic behavior. Each sample that displays a low-resistive linear current-voltage characteristic also exhibits good ohmic contact. The thickness of the samples was measured using a surface profiler, and it was found that the thickness decreases as the flow rate increases. This may be connected to the increase in the flow rate of the carrier gas during deposition, which leads to a shorter duration for the carbon species to adhere to the substrate and create a film. Alternatively, the elevated flow rates might facilitate the elimination of precursor and byproduct gases before they have the chance to contribute to film growth, resulting in a decrease in the overall film thickness. On the

other hand, at lower flow rates, the carbon species have a longer period to be adsorbed and to react on the substrate surface, resulting in thicker films (Wang et al., 2024).

Figure 5.16 illustrates the electrical conductivity obtained from the I-V curve data. It can be noted that the conductivity showed a significant rise from 4.49×10^1 $S.cm^{-1}$ to 1.08×10^2 $S.cm^{-1}$ at 25 sccm and 30 sccm, respectively. This increase may be attributed to the tendency of sp^2 bonding to form π bonds, which enhances conductivity (Kamaruzaman et al., 2013). At 35 sccm, however, the conductivity decreases to 9.60×10^1 $S.cm^{-1}$; this reduction is likely linked to altered microstructure in the films that results in suboptimal sp^2 clustering in the carbon network (Dayana et al., 2012). Subsequently, conductivity improves again at 40 sccm, reaching 1.66×10^2 $S.cm^{-1}$ before dropping once more to 1.41×10^2 $S.cm^{-1}$ at 45 sccm. The enhancement in conductivity is associated with an increase in the proportion of sp^2 bonded carbon within a-C films. Nonetheless, the decline in conductivity at 45 sccm is likely related to the higher argon flow rate, which may disrupt the formation of sp^2 clusters, resulting in thinner, less dense films with reduced sp^2 content.

The data indicate that a decrease in conductivity corresponds with an increase in the sp^3 content of the sample, along with a rise in resistivity. Likewise, as the conductivity and sp^2 content increases, the resistance decreases. The conductivity is also influenced by carrier density and mobility, in addition to the size of the sp^2 clusters. With increasing compressive stress and film thickness, the number of π states at sp^2 sites may diminish (Mohagheghpour et al., 2016). A comparison of the conductivity reveals that a-C thin films deposited at 25 sccm exhibit lower conductivity than those deposited at 40 sccm, which may be attributed to thickness, given that the 25 sccm samples (1820 nm) are thicker than those at 40 sccm (410 nm).

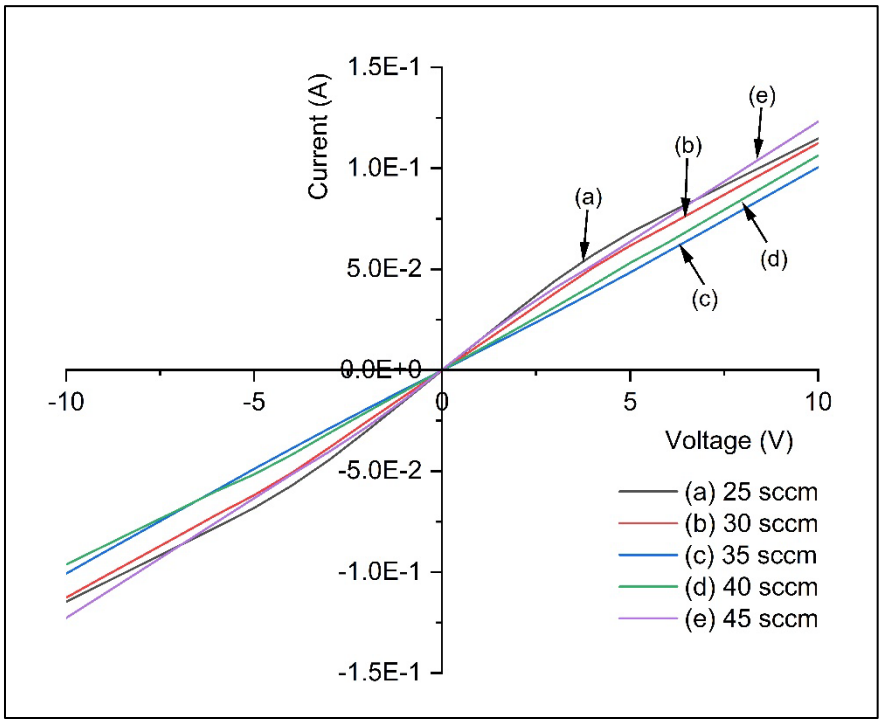

Figure 5.15 I-V Curve of a-C Thin Films Deposited at Different Gas Flow Rates

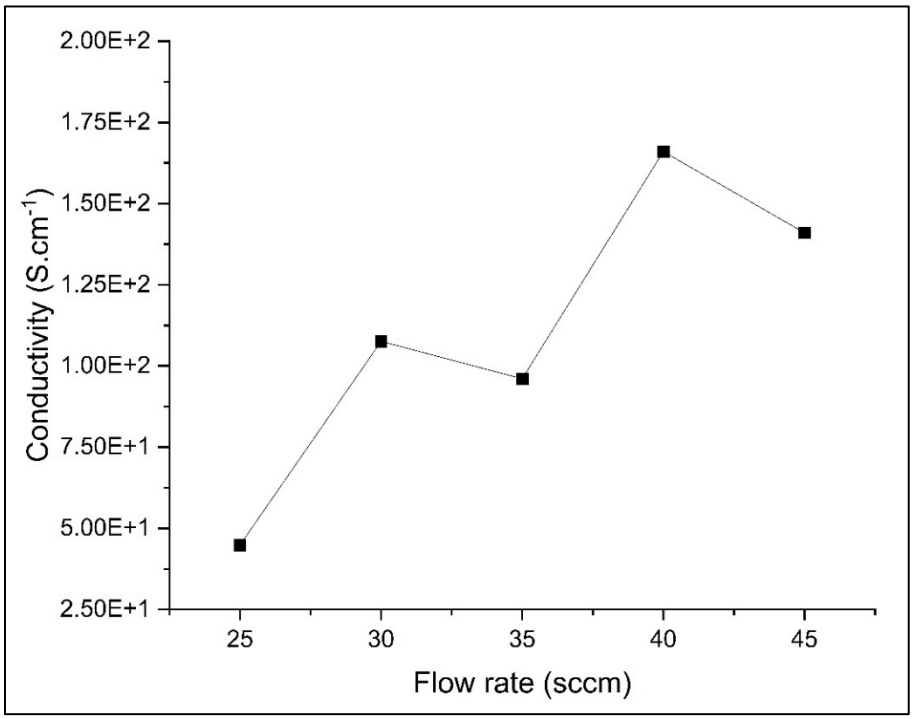

Figure 5.16 Electrical Conductivity of a-C Thin Films Deposited at Different Gas Flow Rates

Table 5.9
Electrical Resistivity, Conductivity, and Thickness of a-C Deposited at Different Gas Flow Rates

Flow Rate (sccm)	**Resistivity (Ω.cm)**	**Conductivity ($S.cm^{-1}$)**	**Average thickness (nm)**
25	2.23×10^{-2}	4.49×10^{1}	1820
30	9.29×10^{-3}	1.08×10^{2}	720
35	1.04×10^{-2}	9.60×10^{1}	690
40	6.02×10^{-3}	1.66×10^{2}	410
45	7.09×10^{-3}	1.41×10^{2}	590

5.5 Chapter Summary

The production of a-C thin films from oyster mushroom extract, which was extracted using n-hexane solvent, in this research, utilized the CVD method. To examine the influence of growth parameters, various factors such as the quantity of oyster mushroom waste extract used, deposition temperatures, and the flow rate of argon gas were investigated. The findings indicated that a usage of 2 ml of oyster mushroom waste extract, a deposition temperature of 850°C, and a flow rate of 40 sccm were identified as the optimal growth conditions for the undoped a-C films. These conditions were brought forward to compare the structural and electrical properties of pure undoped a-C films with the N-doped a-C films for each parameter.

CHAPTER 6
DEPOSITION OF NITROGEN-DOPED AMORPHOUS CARBON THIN FILMS

6.1 Introduction

The study findings and experimental results of nitrogen-doped amorphous carbon (a-CN) thin films from oyster mushroom waste extract, which was extracted using n-hexane solvent, through the CVD technique, as detailed in Chapter 3, are presented in this chapter. The analysis of the structural and electrical data is part of the investigation of these results. This chapter also uses the same characterization and analysis methods as Chapter 5. The purpose of this study is to examine how nitrogen doping affects the characteristics of a-C thin films made from oyster mushroom waste extract and deposited using the CVD process. Since the characteristics of a-CN are greatly influenced by the deposition methods and parameters, the effects of deposition temperatures and gas flow rate are investigated.

6.2 Effect of Deposition Temperature

The previous chapter established the ideal quantity of oyster mushroom waste extract, which is 2 ml, at a fixed precursor temperature of 350°C for 30 minutes. In this sub-chapter, the synthesis of a-CN thin films at different deposition temperatures (650°C, 750°C, 850°C, and 950°C) with 40 sccm nitrogen (N) gas flow rate on a silicon substrate was employed using the CVD technique. The structural and electrical properties were investigated.

6.2.1 Structural Properties

6.2.1.1 Raman Spectroscopy

The Raman spectra of the a-CN thin films grown from oyster mushroom waste extract at different deposition temperatures ranging from 1000 cm^{-1} to 2000 cm^{-1} are displayed in Figure 6.1. As mentioned in Chapter 5, the peaks that are typically existed

in a-C are known as D and G peaks, that are often found around 1310-1390 cm^{-1} and 1575-1600 cm^{-1}, respectively (Moseenkov et al., 2023). Generally, both of the peaks associated with the disorder and the sp^2 carbon bonding information, such as the sp^2 vibration and clustering (Yuan et al., 2025). The breathing modes of the sp^2 carbon atoms in the rings, which are only active when defects or disorder are present, are associated with the D peaks (Li et al., 2020). Meanwhile, all pairs of sp^2 carbon atoms in the rings and chains have stretching bonds, which is the reason G peaks occur (Lin et al., 2021; Park et al., 2025).

The presence of the D and G peaks, which are approximately positioned at ~1350 cm^{-1} and ~1590 cm^{-1} in this study, the deposition of carbon from oyster mushroom waste extract using the CVD technique was successful. Table shows the intensity ratio (I_D/I_G) for a-CN thin films that is determined from the data of the Raman peaks positions. There is an increase in I_D/I_G ratios of the a-CN thin films with incorporation of the deposition temperatures. As the deposition temperatures rise to 950°C, it is evident that the I_D/I_G ratio, which is 0.67 at 650°C, rises to 1.12. These might be due to the increase in the sp^2 carbon structures in the a-CN thin films which affect the graphitization (Jaisi et al., 2023).

According to the results from the Raman spectra of undoped a-C (Chapter 5) and a-CN thin films, shown that there are certain modifications occur, particularly an increase in the I_D/I_G ratio, just by merely switching their carrier gas from argon gas (Ar) to nitrogen gas (N). This is evident when comparing the undoped a-C and a-CN thin films that were deposited from 750°C to 950°C. However, it is found only at 650°C does not follow the trends, where the I_D/I_G ratio decreases from 0.70 for undoped a-C to 0.67 for a-CN thin films. From the highest I_D/I_G ratio (0.80) of the undoped a-C at 950°C, the ratio can be seen to increase to 1.12, which is the highest I_D/I_G ratio for the a-CN thin films at similar deposition temperatures, 950°C. This can be attributed to the existence of N doping in the a-C thin films, which boosts the sp^2 concentration along with the decrease of the sp^3/sp^2 ratio in the samples (Marton et al., 2013).

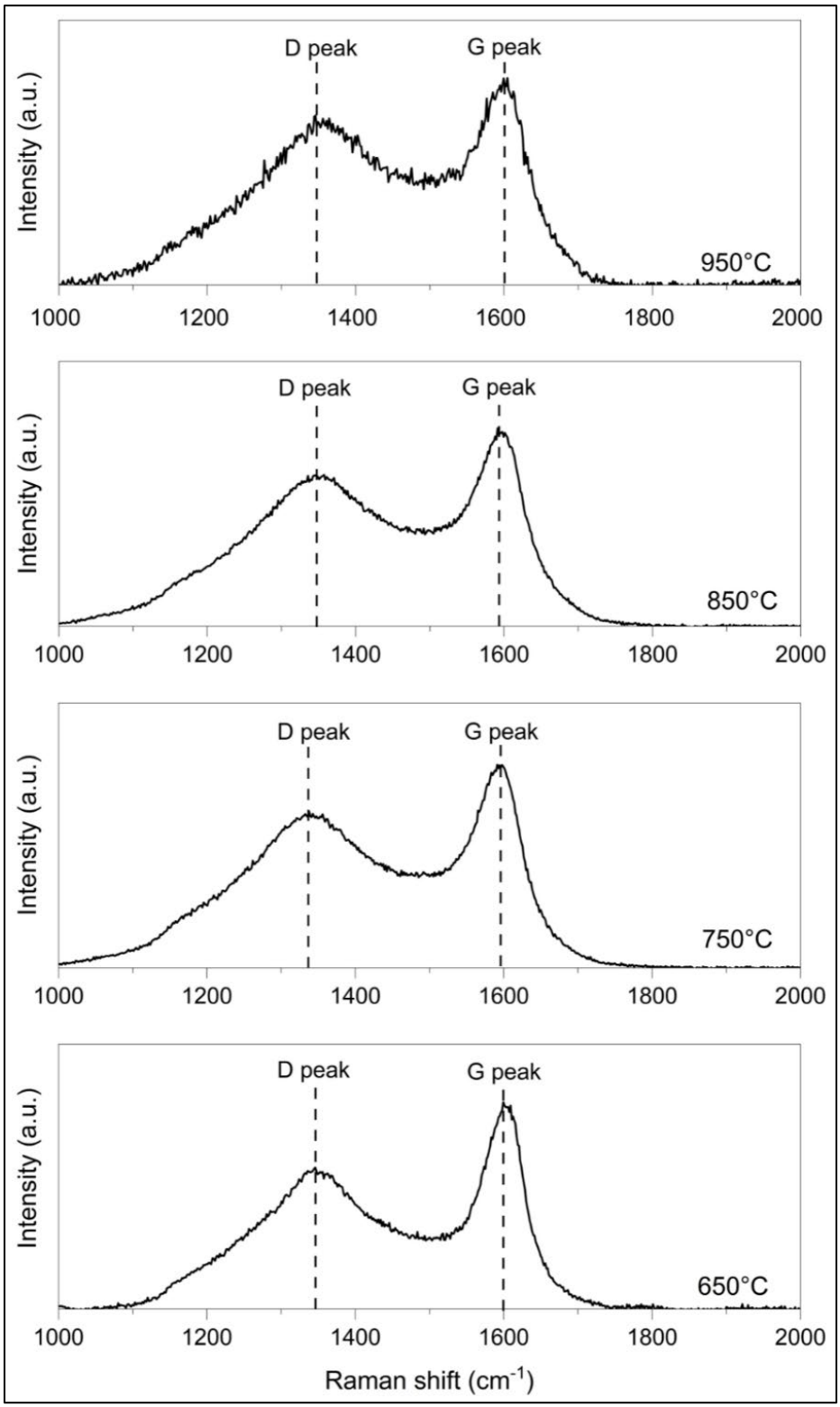

Figure 6.1 Raman Spectra of a-CN Thin Films Deposited at Different Deposition Temperatures

Table 6.1
The D and G Peak Position, and the Intensity Ratio of a-CN Deposited at Different Deposition Temperatures

Deposition temperature (°C)	**D peak position (cm^{-1})**	**G peak position (cm^{-1})**	**Intensity ratio (I_D/I_G)**
650	1342	1599	0.67
750	1342	1591	0.76
850	1357	1591	0.78
950	1345	1599	1.12

6.2.1.2 Scanning Electron Microscope (SEM)

Figure 6.2 displays the SEM images of the surface of the a-CN thin films at various deposition temperatures at a 20kx magnification using a 20kV voltage. From the image, at 650°C, it shows a very smooth, featureless surface with no visible particles or granules. The film appears continuous and shows no significant texture or roughness. Similarly, the film deposited at 750°C maintains its relative smoothness, though a few small bright spots are sparsely distributed, but still without obvious particle formation. The low deposition temperature may be the reason for this, as it leads to limited atomic mobility, which inhibits significant nucleation and particle development (Panickar et al., 2020). Another possibility is that the particles appear to be in a smaller form, which is invisible at the current magnifications and resolutions (Ishak et al., 2013).

In contrast, a few distinct, well-defined spherical particles with a few tiny spots or irregularities in the background occur in the a-CN film that was deposited at 850°C. It is clear at this temperature that the higher deposition temperature raises surface mobility, enabling some C clusters to form and develop into microspheres (Nikolova & Tzvetkov, 2025). Additionally, a morphological transition is observed, with some spherical particles appearing on the surface in place of the continuous, particle-free films from the previous deposition temperature. Nearly no clear background is visible at 950°C, since the surface is now densely covered with many spherical particles of various sizes. High temperatures promote the nucleation, development, and aggregation of C into microspheres throughout the entire surface because they maximize atomic diffusion and complete precursor decomposition. Partial graphitization of C spheres is possible, particularly at the surface. Based on these findings, it is clear that the a-CN

films show less uniform granularity and more spherical particles as the deposition temperature increases. The reason for this is that N greatly impacted the nucleation of the particles, which altered the C's morphology (Jaisi et al., 2023; Kim et al., 2023; Song et al., 2024)

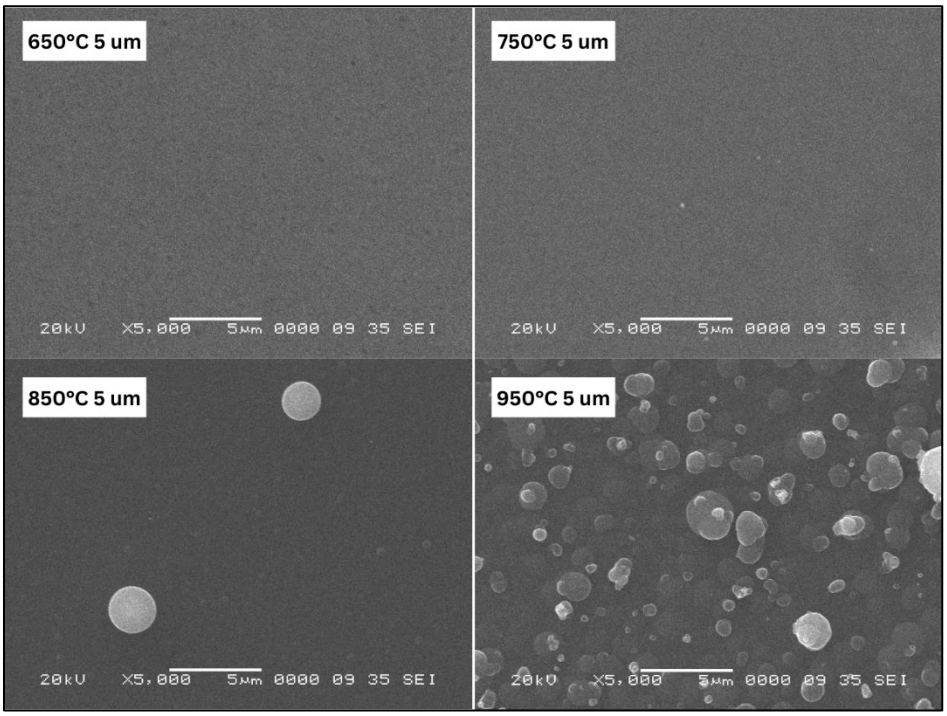

Figure 6.2 SEM Images of a-CN Thin Films Deposited at Different Deposition Temperatures

6.2.1.3 Energy Dispersive X-Ray Spectroscopy (EDX)

EDX analysis was used to examine the chemical compositions of the a-CN thin films. The study shows that the elemental composition on the surface of the a-CN thin films consists of carbon (C), oxygen (O), nitrogen (N), and silicon (Si). The successful nitrogen doping operation into the a-C thin films is indicated by the presence of the elements N and C. The presence of the Si element here corresponds to the silicon substrate. However, the Si and O elements are unnecessary as the main purpose of this analysis is to validate the presence of N and C elements in the a-CN thin films. Figure 6.3 and Table demonstrate that the percentage of C atoms rose moderately from 0.00% to 83.21% with the increasing deposition temperatures. It is evident that the N, Si, and O elements that are also present in the a-CN thin films gradually decrease with deposition temperatures. It is mentioned that the decline in N element might be caused by the C-N bonds that are detached as the deposition temperatures increase (Kumar et

al., 2010). The C elements that are not found in the samples at 650°C and 750°C might be due to the sample's thickness, which is 135 nm and 166 nm, respectively, as it may be too low to impair detectability.

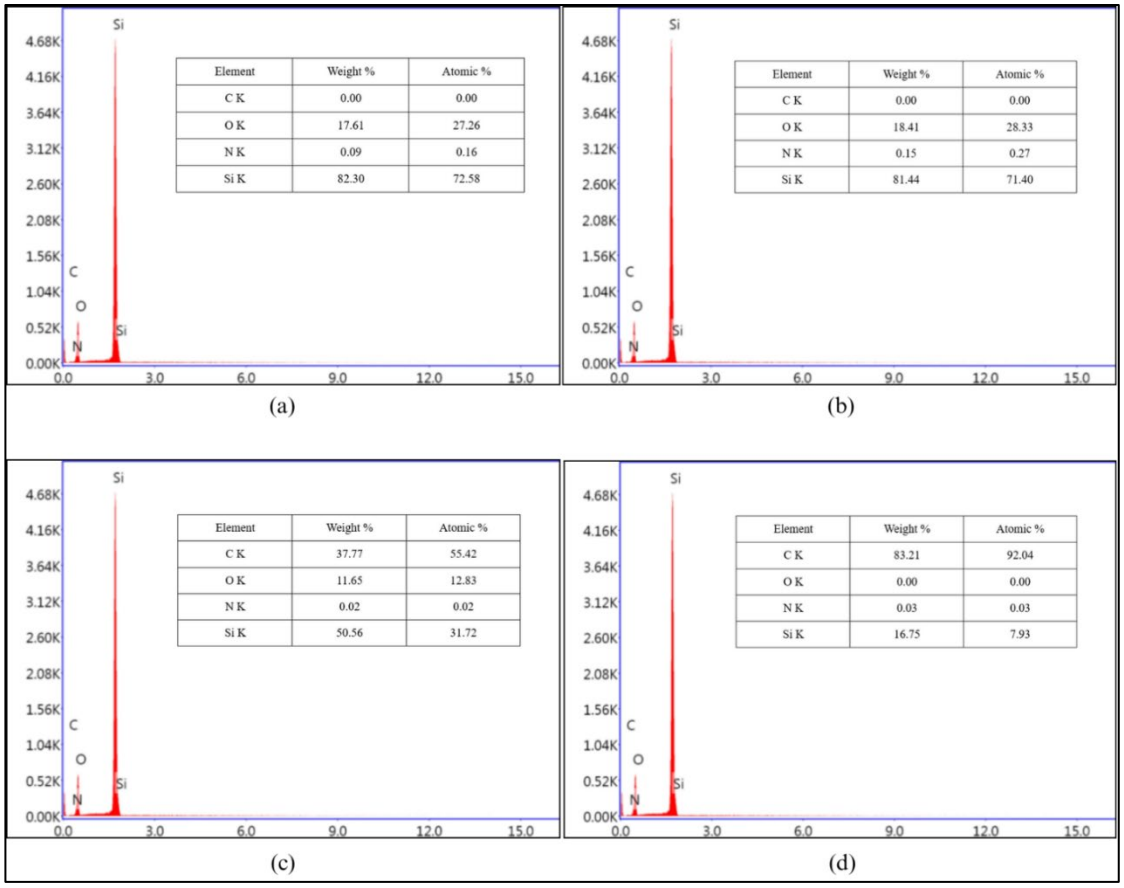

Figure 6.3 EDX Data of the A-CN Thin Films Deposited at Different Deposition Temperatures (a) 650°C (b) 750°C (c) 850°C (d) 950°C

Table 6.2
EDX Data of a-CN Deposited at Different Deposition Temperatures

Deposition temperature (°C)	Elements	Weight %	Atomic %
650	C K	0.00	0.00
	O K	17.61	27.26
	N K	0.09	0.16
	Si K	82.30	72.58
750	C K	0.00	0.00
	O K	18.41	28.33
	N K	0.15	0.27
	Si K	81.44	71.40
850	C K	37.77	55.42

	O K	11.65	12.83
	N K	0.02	0.02
	Si K	50.56	31.72
950	C K	83.21	92.04
	O K	0.00	0.00
	N K	0.03	0.03
	Si K	16.75	7.93

6.2.2 Electrical Properties

6.2.2.1 Current-Voltage (I-V) Measurement

In Figure 6.4, the graph exhibits linear behavior that shifts upwards as the deposition temperatures rise, indicating that the resistance is low as the a-CN thin films are deposited at increasing temperatures. It has a similar trend to the obtained results for undoped a-C thin films, though the electrical conductivity value for a-CN thin films is higher compared to the undoped a-C. A surface profiler was used to determine the thickness of the a-CN (135-1320 nm), and it is evident that the thickness of the films increased as the deposition temperatures increased. However, the thickness value is smaller compared to the undoped a-C, which was discussed in Chapter 5 (190-1410 nm). The desorbed N species or the regionally N-rich areas on the film surface may be the cause of the decrease in thickness in a-CN films, which lowers the accumulation and film thickness during the deposition process (Awang & Abd Aziz, 2019; Kumar et al., 2010).

The electrical conductivity of a-CN thin films formed at various deposition temperatures is shown in Figure 6.5. The conductivity between 650°C and 950°C is more clearly visible on the graph. It can be seen that starting from 650°C, the electrical value progressively rises from 2.45×10^{-5} S.cm^{-1} to 4.27 S.cm^{-1} at 750°C. The conductivity value increased drastically from 4.27 S.cm^{-1} at 750°C to 1.59×10^{2} S.cm^{-1} at 850°C, which is the highest conductivity in the a-CN thin films. However, the electrical conductivity (7.48×10^{1} S.cm^{-1}) decreases when the deposition temperature reaches 950°C. The fraction of sp^2 clusters in the amorphous network increase as a result of the rearrangement of C and N atoms encouraged by the increasing deposition temperatures. Furthermore, the doping of N causes the π states at

sp^2 sites, which are close to the Fermi level, to provide a connection between the edges of the valence and conduction band, which controls the electrical conductivity (Lin et al., 2021).

In comparison to the undoped a-C that is also formed at various temperatures (Chapter 5), the electrical conductivity value of a-CN thin films is clearly higher. This is due to the successful incorporation of N doping into the films, increasing graphitic properties and conductivity, while lowering resistivity through the formation of conductive bonds and sp^2 carbon clustering, which introduces localized hopping states that facilitate charge transport (Mi et al., 2024; Ray et al., 2014).

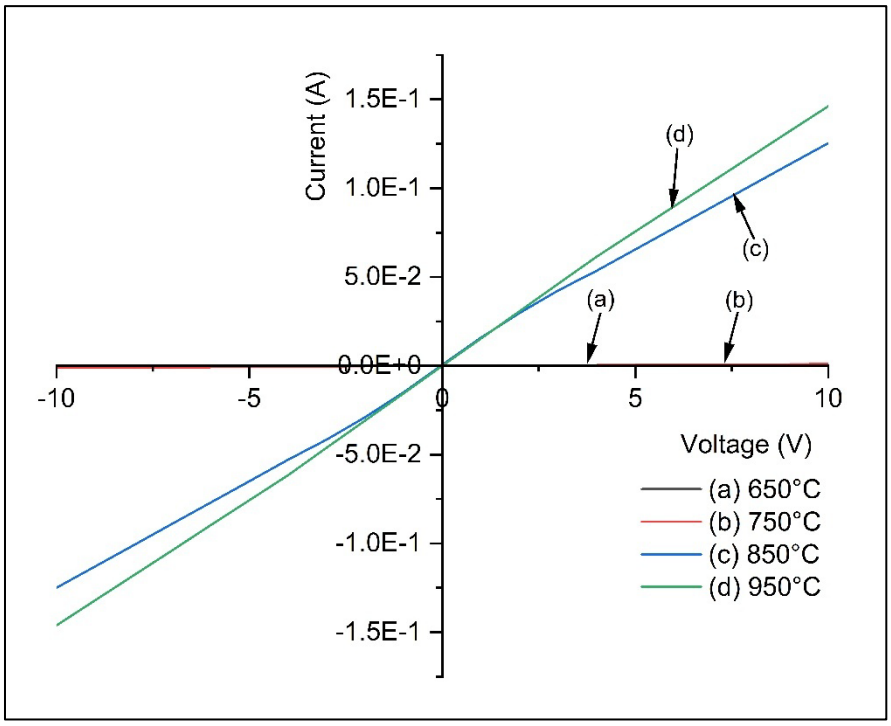

Figure 6.4 I-V Curve of a-CN Thin Films Deposited at Different Deposition Temperatures

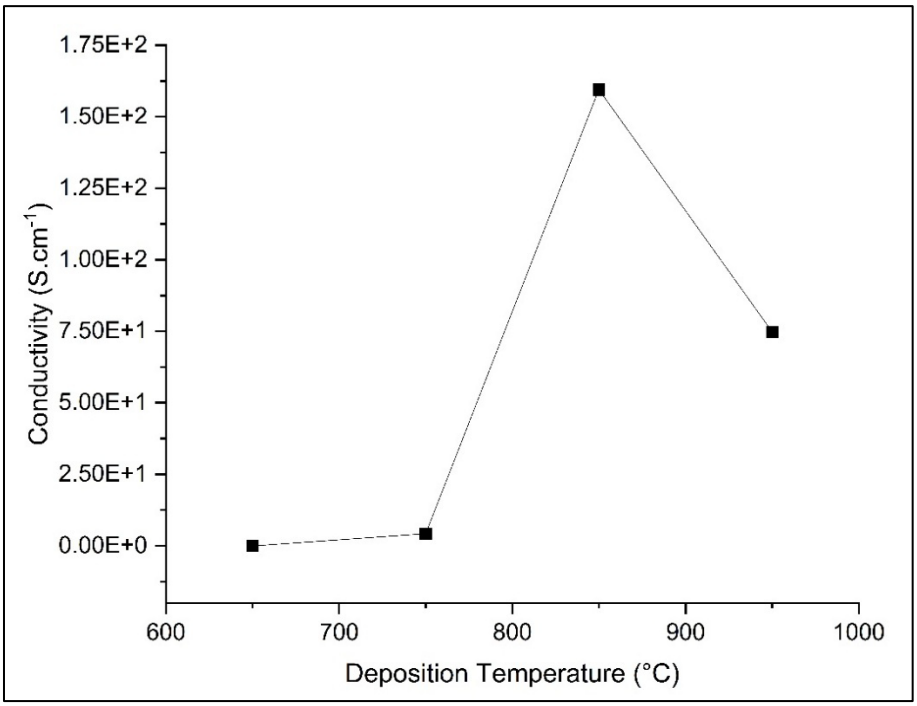

Figure 6.5 Electrical Conductivity of a-CN Thin Films Deposited at Different Deposition Temperatures

Table 6.3
Electrical Resistivity, Conductivity, and Thickness of a-CN Deposited at Different Deposition Temperatures

Deposition temperature (°C)	**Resistivity (Ω.cm)**	**Conductivity ($S.cm^{-1}$)**	**Average thickness (nm)**
650	4.09×10^{4}	2.45×10^{-5}	135
750	2.34×10^{-1}	4.27	166
850	6.27×10^{-3}	1.59×10^{2}	533
950	1.34×10^{-2}	7.48×10^{1}	1320

6.3 Effect of Gas Flow Rate

The growth of a-CN has been previously investigated at different deposition temperatures. The optimum parameter for now was found to be using 2 ml of oyster mushroom waste extract at 850°C deposition temperature with a fixed 350°C precursor temperature for 30 mins deposition. In this parameter, the flow rate of carrier gas, which is Nitrogen gas, was employed with varied rates from 25 sccm to 45 sccm by 5 sccm increments. The structural and electrical properties of the a-CN on a silicon substrate were investigated.

6.3.1 Structural Properties

6.3.1.1 Raman Spectroscopy

Figure 6.6 shows the Raman spectra of a-CN thin films deposited at various flow rates ranging from 1000 cm^{-1} to 2000 cm^{-1}. It is evident that two peaks, referred to as the D and G peaks, are present at various flow rates. The existence of these peaks is typically shown in a-C. The I_D/I_G ratio and the D and G peak position data were summarized in Table. The data show that when the gas flow rates rose, the G peak of the a-CN location moved lower, from 1604 cm^{-1} (25 sccm) to 1601 cm^{-1} (35 sccm). Additionally, from 0.77 (25 sccm) to 0.79 (35 sccm), the I_D/I_G ratio rises. The π to π^* scattering of the sp^2 clusters of the a-CN where the sp^2 concentration increases are thought to be connected to the changes in G peak position that occur as the flow rates increase and the increases in the I_D/I_G ratio. It is caused by the moderate N incorporation, which boosted the graphitization and sp^2 carbon clustering (Mi et al., 2024; Sun et al., 2022). However, the I_D/I_G ratio shows a reduction from 0.79 (35 sccm) to 0.78 (45 sccm), indicating that the size of sp^2 domains may be reduced at high N gas flow. The excessive N introduction leads to the defect density as they are disrupting the graphitic domains (Hoque et al., 2019).

As mentioned before, because of the modifications brought about by the presence of N in the films, the I_D/I_G ratio of the undoped a-C (Chapter 5) is lower compared to the a-CN thin films. In the a-C matrix, the N doping creates defects and encourages the development and clustering of sp^2 graphitic domains. The development of more disorder films is further supported by the rise of the I_D/I_G value of a-CN thin films (Ray et al., 2014). In contrast, undoped a-C thin films typically exhibit a lower degree of sp^2 clustering and fewer defects, resulting in a lower I_D/I_G ratio.

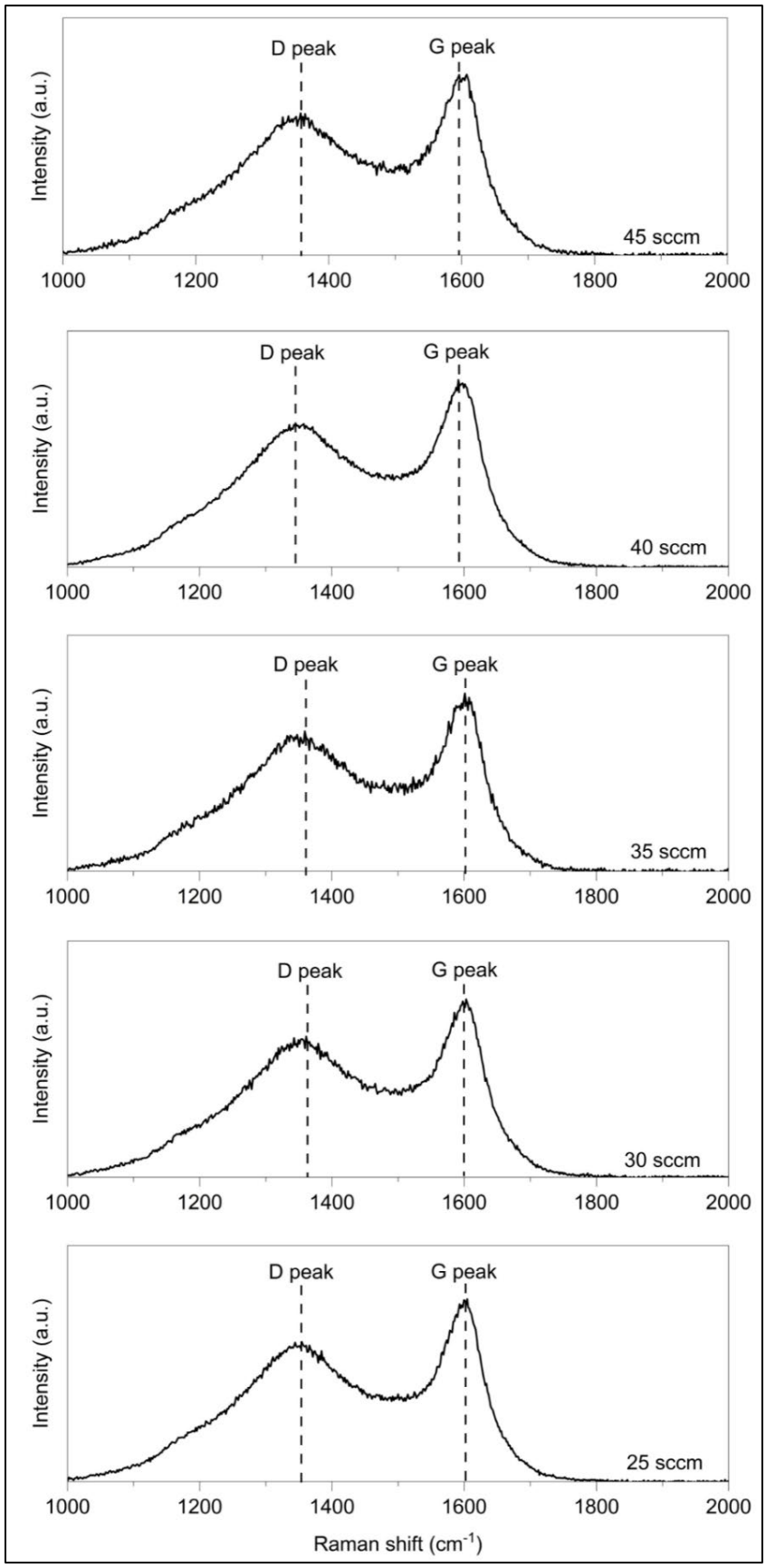

Figure 6.6 Raman Spectra of a-CN Thin Films Deposited at Different Gas Flow Rates

Table 6.4
D and G Peak Position, and Intensity Ratio of a-CN Deposited at Different Gas Flow Rates

Flow rate (sccm)	D peak position (cm^{-1})	G peak position (cm^{-1})	Intensity ratio (I_D/I_G)
25	1354	1604	0.77
30	1360	1602	0.79
35	1359	1601	0.79
40	1357	1591	0.78
45	1357	1596	0.78

6.3.1.2 Scanning Electron Microscope (SEM)

Figure 6.7 shows the SEM image of a-CN films deposited at different flow rates. A comparatively sparse dispersion of particles on the Si substrate is seen in the image at 25 sccm. The slow growth may be the cause of the particles' relatively smooth surface, small spherical, well-separated particles that do not exhibit substantial aggregation. The low density implies fewer nucleation sites, possibly indicating that the availability of N species is constrained by the N flow rate at this level, leading to fewer nucleation events. Particles are still mostly tiny, spherical, well-defined, and more uniform at 30 sccm, however, the film exhibits a somewhat higher density compared to the film at 25 sccm. This might be due to more nucleation sites as the N species increase, enhancing the C deposition process.

Meanwhile, the images shown at 35 sccm display a higher density with some overlapping or agglomerated particles and closely packed particles. Despite their relative uniformity, the particles exhibit some signs of coalescence, which results in somewhat bigger particle sizes. This is due to the higher N flow that encourages particle development and high nucleation density. The particle density or surface coverage clearly decreases at 40 sccm in comparison to 35 sccm, but the spherical particles become notably larger, more distinct, and more isolated. This is due to the increased N flow, which may inhibit nucleation but promote the growth of already-existing particles. At 45 sccm, the particles remain spherical, large, well-formed, and distinct. Similar to 40 sccm, the particle density is sparse, but the particles are larger because of very high

N flows, maintaining particle development conditions rather than nucleation (Jaisi et al., 2023; Kim et al., 2023; Song et al., 2024).

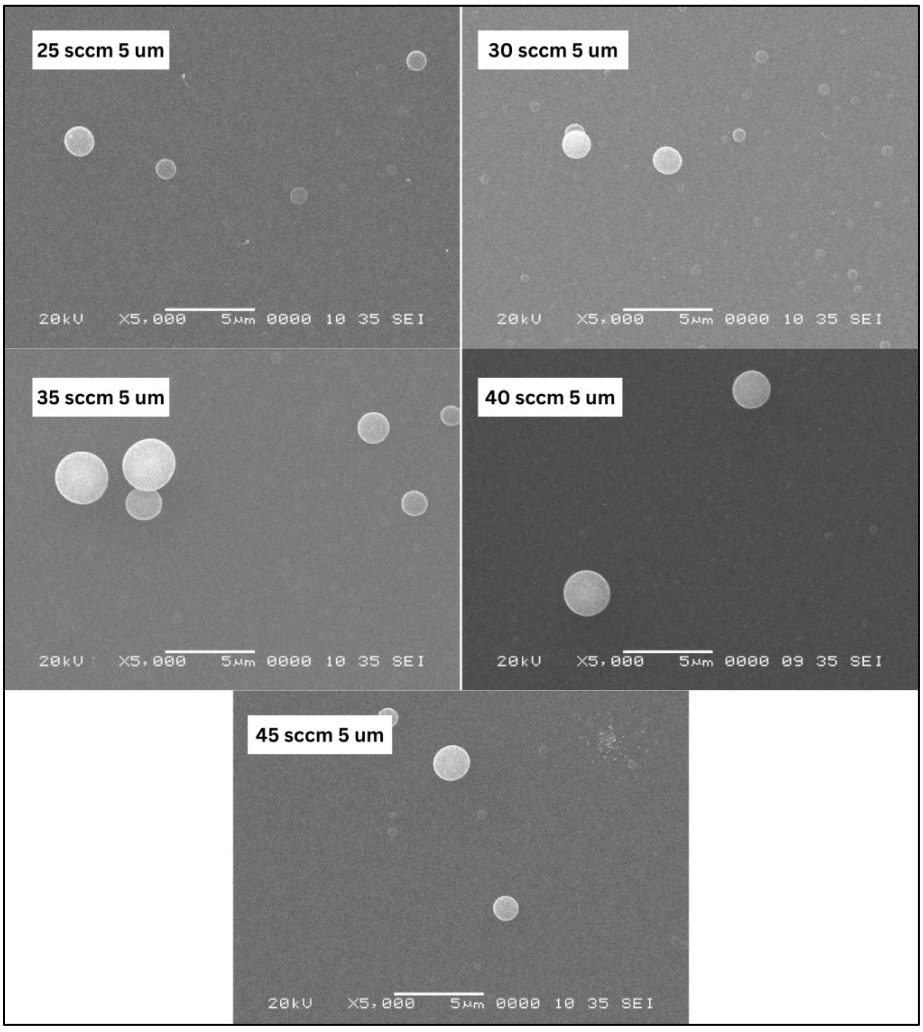

Figure 6.7 SEM Images of a-CN Thin Films Deposited at Different Gas Flow Rates

6.3.1.3 Energy Dispersive X-Ray Spectroscopy (EDX)

According to Table and Figure 6.8, the main detected elements are C, O, N, and Si. The existence of C and N elements indicates the success of carbon deposition and N doping into the films. It can be seen that at 25 sccm, it has high C content (39.10%), low O (5.87%), and traces of N (0.01%). This indicates substantial but discontinuous C coverage, low N incorporation, and modest O detected due to the lower flow of gas. At 30 sccm, the C elements decreased to 26.95% with an increase in O (9.24%) and Si (63.80%). Lower C may indicate less dense coverage or thinner deposits, and increased O reflects more oxidation, while N elements remain minimal. This could be seen

through their thickness, where the 25 sccm sample has a thickness of 595 nm thicker compared to the 30 sccm sample with 450 nm.

Meanwhile, at 35 sccm, the C element increases (34.17%), O element decreases (7.13%) compared to 30 sccm, suggesting more effective C deposition and less oxygenated species. The N element remains low. It can be seen that the a-CN films deposited at these flow rates are thicker (550 nm) compared to 30 sccm (450 nm), as the Si elements of 35 sccm are lower than 30 sccm. Then, at 40 sccm, the C content slightly increases (37.77%), and the N elements remain low, though slightly more than in previous samples. The O element is the highest (11.65%) among all samples, which might come from more oxygen-containing groups or surface contamination. At 45 sccm, there is a slight drop in C (32.64%) and O (7.25%) content compared to 40 sccm, higher Si element (60.10%), indicating reduced film thickness or particle density, which matches the previous SEM data of fewer particles at high flow.

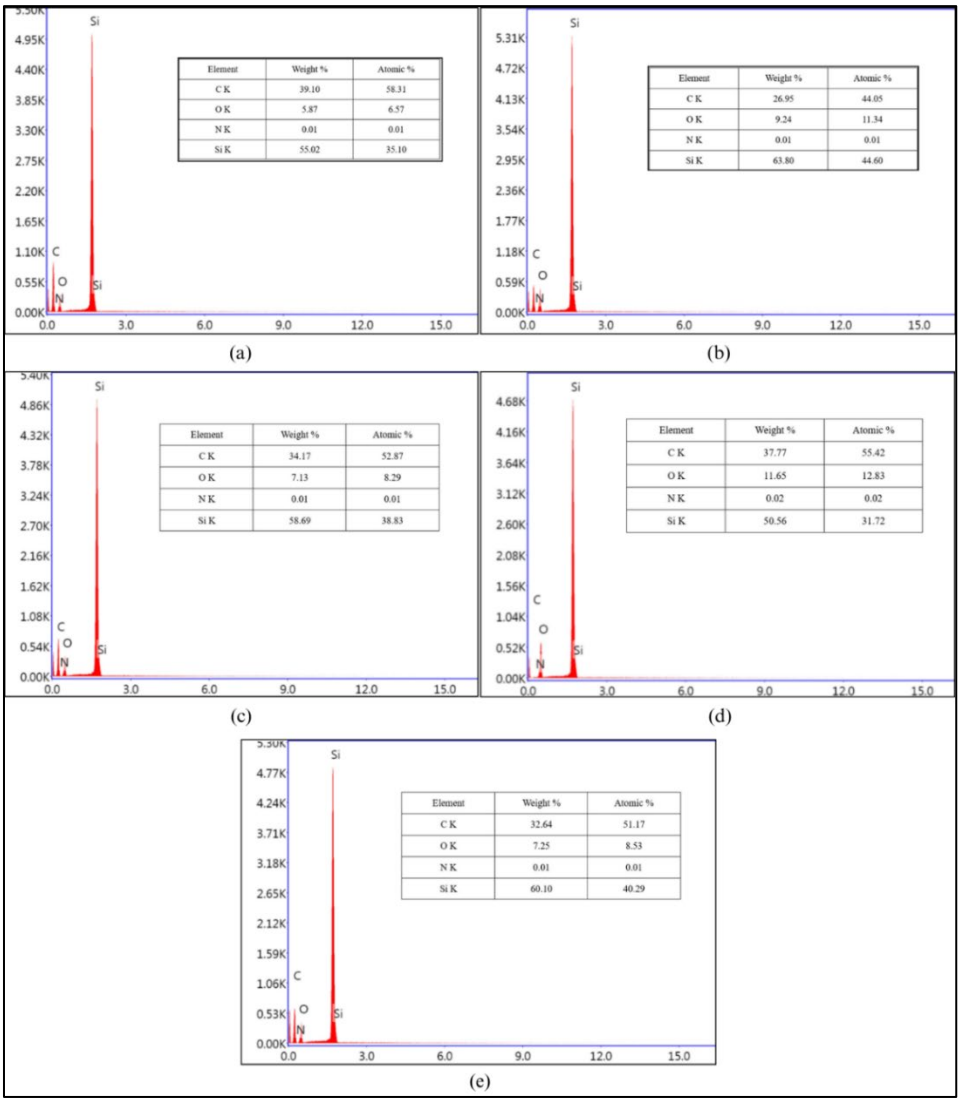

Figure 6.8 EDX Data of a-CN Films Deposited at Different Gas Flow Rates (a) 25 sccm (b) 30 sccm (c) 35 sccm (d) 40 sccm (e) 45 sccm

Table 6.5
EDX Data of a-C Thin Films Deposited at Different Gas Flow Rates

Flow rate (sccm)	Elements	Weight %	Atomic %
25	C K	39.10	58.31
	O K	5.87	6.57
	N K	0.01	0.01
	Si K	55.02	35.10
30	C K	26.95	44.05
	O K	9.24	11.34
	N K	0.01	0.01
	Si K	63.80	44.60
35	C K	34.17	52.87
	O K	7.13	8.29

	N K	0.01	0.01
	Si K	58.69	38.83
40	C K	37.77	55.42
	O K	11.65	12.83
	N K	0.02	0.02
	Si K	50.56	31.72
45	C K	32.64	51.17
	O K	7.25	8.53
	N K	0.01	0.01
	Si K	60.10	40.29

6.3.2 Electrical Properties

6.3.2.1 Current-Voltage (I-V) Measurement

To examine the electrical characteristics of a-CN thin films, a 2-point probe was utilized. Figure 6.8 displays the linear I-V graph of the films that were deposited at different flow rates of N gas. The linear graph shows a good ohmic behavior. It is believed that their resistance decreases with increasing slope. The thickness of the samples was examined using a surface profiler, and it was found that the value dropped as the gas flow rate rose. The thickness obtained ranged from 450 nm to 595 nm for all of the samples with a flow rate of 25 sccm to 45 sccm. Table 6.6 shows that the thickness decreased gradually as the gas flow rate increased due to the uniformity of the precursor carried from the first furnace by the N gas to the second furnace, where the deposition on the substrate occurred. This is because the transported precursors traveled too quickly when the flow rate increased, leaving them with little time to deposit on the substrate in the second furnace. Furthermore, it seems that the undoped a-C films (410-1820 nm) have a higher thickness value than the a-CN films as the gas flow rate increases. The areas that are filled with N species on the surface are said to have the potential to reduce the thickness of a-CN films, which in turn reduces the accumulation and film thickness during the deposition process (Awang & Abd Aziz, 2019; Kumar et al., 2010).

Figure 6.9 demonstrates the electrical conductivity of a-CN films produced at different gas flow rates. It is observed that the conductivity shows a slight decrease from 1.64×10^2 S.cm^{-1} at 25 sccm to 1.60×10^2 S.cm^{-1} at 30 sccm. Given that the

conductivity first dropped and then sharply increased at 35 sccm with 1.73×10^2 S.cm^{-1}, this could be the result of an increase in defects raised by uneven N incorporation (Ishak et al., 2015; Silva et al., 1997). The increase in conductivity might be caused by the N incorporation, which provides excess electrons. The existence of N dopant could induce a conversion from sp^3 to sp^2, which increases the intensity of the π region, thus increasing the conductivity of the a-CN films with the flow rates (Endrino et al., 2009; Kaushal & Andrews, 2025; Kumar et al., 2010). However, the conductivity then decreases sharply to 1.62×10^2 S.cm^{-1} and 1.54×10^2 S.cm^{-1} at 40 sccm and 45 sccm, respectively. This might be due to excessive N causing structural defects and degradation of a-CN film when the flow rate increases. In comparison to the undoped a-C that was also produced at various flow rates (Chapter 5), the electrical conductivity of a-CN films is obviously higher. This is due to the successful incorporation of N doping into the films, which increases the graphitic and conductivity of a-CN.

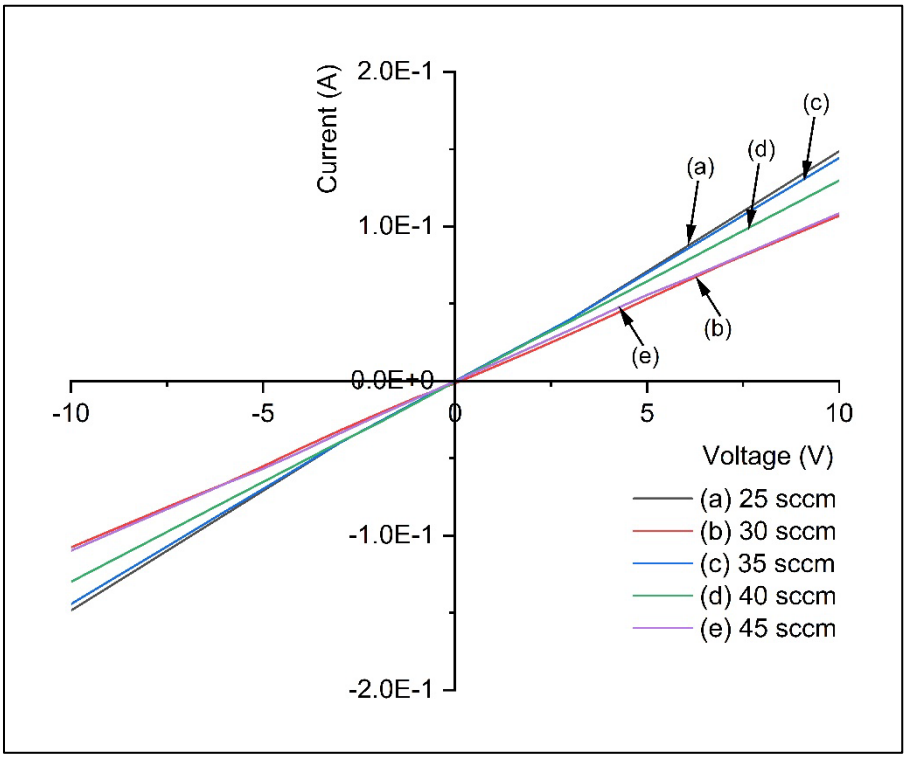

Figure 6.9 I-V Curve of a-CN Films Deposited at Different Gas Flow Rates

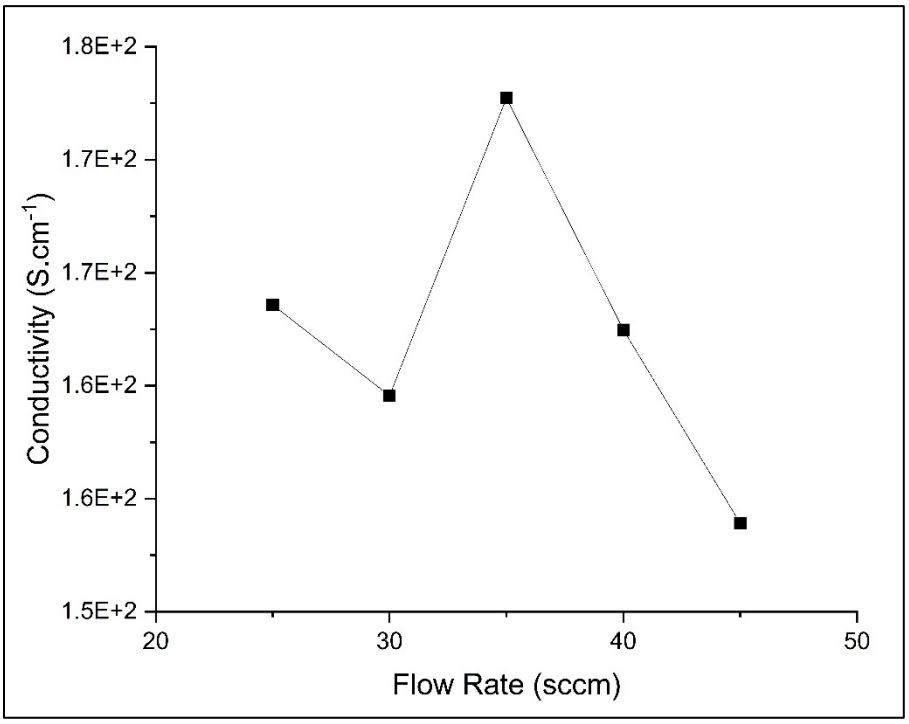

Figure 6.10 Electrical Conductivity of a-CN Films Deposited at Different Gas Flow Rates

Table 6.6
Electrical Resistivity, Conductivity, and Thickness Of a-CN Deposited at Different Gas Flow Rates

Flow Rate (sccm)	**Resistivity (Ω.cm)**	**Conductivity ($S.cm^{-1}$)**	**Average thickness (nm)**
25	6.11×10^{-3}	1.64×10^{2}	595
30	6.27×10^{-3}	1.60×10^{2}	450
35	5.79×10^{-3}	1.73×10^{2}	550
40	6.15×10^{-3}	1.62×10^{2}	533
45	6.50×10^{-3}	1.54×10^{2}	476

6.4 Chapter Summary

Doping was carried out using the CVD method by switching the gas from argon to nitrogen. To assess the effect of growth conditions, different factors were analyzed, including the deposition temperatures by adjusting furnace 2's temperature from 650°C to 950°C and the nitrogen gas flow rate varying between 25 sccm and 45 sccm. The results indicated that the doping process was effective, confirming the suitability of the CVD method for doping nitrogen into a-C films. The analysis revealed that a deposition

temperature of 850°C and a nitrogen flow rate of 40 sccm were determined to be the optimal conditions for fabricating a-CN films. Therefore, it can be concluded that when comparing the properties of undoped a-C films, there is a noticeable enhancement in both structural and electrical characteristics of a-C films after nitrogen doping.

CHAPTER 7
CONCLUSION AND FUTURE WORK

7.1 Conclusion

In this research, undoped a-C and a-CN were synthesized from a novel carbon precursor derived from oyster mushroom waste extract through the CVD process. To determine the feasibility of using oyster mushroom waste extract as a carbon precursor for the production of a-C films, characterization was performed utilizing a CHNS elemental analyzer and a TGA. The extraction of extract from the oyster mushroom waste was efficiently accomplished using Soxhlet extraction with two different solvents, hexane and ethanol. Based on the results from the CHNS analyzer, hexane proved to be more effective than ethanol for the extraction, as the hexane solvent shows a higher carbon percentage, 70.387%, which is more suitable to be used as a carbon precursor. Furthermore, the biomass of the oyster mushroom waste was analyzed using the same characterization methods, revealing that it contains sufficient carbon for synthesizing a-C. These findings confirmed that the first objective was met. To determine the optimal decomposition temperature of the oyster mushroom waste extract when used as a precursor for a-C synthesis, TGA analysis was carried out, indicating that 350°C is the ideal temperature, as it does not lead to early or late decomposition.

Various growth parameters were employed to synthesize a-C and a-CN with the desired properties, and the influence of these parameters was thoroughly examined through Raman spectroscopy, scanning electron microscopy (SEM), energy dispersive X-ray spectroscopy (EDX), and current-voltage (I-V) measurements. The growth parameters included examining the effects of precursor volume, deposition temperatures, and gas flow rates for both a-C and a-CN films generated via CVD. For undoped a-C films, the precursor volume was varied between 1-4 ml of oyster mushroom waste extract, while the deposition temperature ranged from 650°C to 950°C, and the gas flow rate was adjusted between 25-45 sccm. For a-CN films, the deposition temperature was explored from 650°C to 950°C, along with the gas flow rate varying between 25-45 sccm.

For every synthesis parameter, the influence of that parameter on the structural characteristics of a-C and a-CN was examined to analyze the type of carbon deposited,

the surface morphology, and the elemental composition and distribution of both films. The optical properties can only be investigated when investigating the effect of the amount of precursor, and it is explored to identify the optical band gap for undoped a-C. The electrical properties were primarily the focus of the investigation, particularly studying the electrical conductivity associated with the synthesis parameters for both a-C and a-CN films. The optimal results for undoped a-C films were achieved when the deposition parameters were set to a precursor amount of 2 ml, a deposition temperature of 850°C, and a deposition flow rate of 40 sccm, using argon gas as the carrier gas.

When exploring the impact of the precursor amount, the recorded electrical conductivity for 2 ml of precursor was 1.51×10^{-5} S. cm^{-1}, which was the highest among the various precursor amounts. An optical band gap of 0.37 eV and optical transmittance of 85.07% were measured, with an intensity ratio (I_D/I_G) of 0.71. A high I_D/I_G value indicates a significant presence of sp^2 clusters in the a-C films. Subsequently, when examining the effects of deposition temperature, the highest electrical conductivity of 1.41×10^2 $S.cm^{-1}$ was recorded at a deposition of 850°C. The carbon percentage (C%) was noted to be 26.18% with an I_D/I_G of 0.78. The detection of carbon indicates successful deposition and good film coverage on the substrate. When analyzing the influence of deposition flow rates, the conductivity measured at 40 sccm exhibited the highest electrical conductivity at 1.66×10^2 $S.cm^{-1}$. The C% was recorded at 11.26% with an I_D/I_G of 0.73. The variation in the C element might be attributed to the scanning area, which may have encountered regions with differing amounts of C clusters.

For the nitrogen-doped a-C films, the carrier gas was replaced with nitrogen gas. Besides nitrogen gas, another n-type dopant, such as phosphorus, could be utilized for a-C, but the nitrogen gas was selected because it functions well as both a carrier and a dopant. The primary focus of the investigation was the electrical properties of the films, with electrical conductivity examined for various synthesis parameters. The conductivity of a-CN was found to be higher compared to the undoped a-C films due to the introduction of nitrogen into the films. The structural characteristics were studied to determine the type of carbon films, surface morphology, and elemental composition detectable in the films. The optimal results for a-CN films were achieved with a deposition temperature of 850°C and a deposition flow rate of 35 sccm.

When examining the influence of deposition temperature on a-CN, the recorded electrical conductivity for 850°C measured 1.59×10^2 S.cm^{-1}, the highest among the other deposition temperatures. The C% of 37.77% with an N% of 0.02% and I_D/I_G of 0.78 was obtained. Both the C% and I_D/I_G were higher in the a-CN films compared to the undoped a-C. This sample was then analyzed further concerning the gas flow rate. During the assessment of gas flow rate, the highest electrical conductivity was found at 1.73×10^2 S.cm^{-1} when deposited at 35 sccm. The C% of 34.17% and N% of 0.01% with I_D/I_G of 0.79 was obtained. The findings of both a-C and a-CN films demonstrate that objectives 2 and 3 have been successfully met.

Overall, it can be deduced that nitrogen-doped material exhibits enhanced electrical conductivity, higher carbon content, and improved intensity ratios compared to undoped a-C films. This indicates that the presence of nitrogen has positively influenced the properties of the previously undoped a-C films, which exhibited weak p-type behavior.

7.2 Future Work

For future endeavors, additional efforts are required to explore the use of natural, sustainable resources to create a more environmentally friendly system. The utilization of waste extract from oyster mushrooms as a carbon precursor in the creation of a-C films represents an innovative approach to fostering an eco-friendly environment, while also reducing production costs due to the accessibility and abundance of oyster mushroom waste. In this investigation, a-C was synthesized employing oyster mushroom waste extract on a silicon substrate through the CVD method. Future advancements could include enhancements in systems, methodologies, and control metrics to minimize defects in the a-C films and to achieve a more thorough understanding of the deposition process. For example, improvements could be made in the substrate cleaning methods during preparation, selection of substrate types and carrier gases, as well as optimizing the deposition duration. Additionally, studying the potential uses of these a-C films in electronic applications such as solar cells and sensors would yield valuable practical insights. Moreover, research into additional properties, like the mechanical characteristics of a-C, should be pursued to establish a notable material for numerous prospective applications.

REFERENCES

Abd Aziz, N. A., Hasham, R., Sarmidi, M. R., Suhaimi, S. H., & Idris, M. K. H. (2021). A review on extraction techniques and therapeutic value of polar bioactives from Asian medicinal herbs: Case study on Orthosiphon aristatus, Eurycoma longifolia and Andrographis paniculata. *Saudi Pharmaceutical Journal : SPJ*, *29*, 143 - 165.

Abid, N., Khan, A. M., Shujait, S., Chaudhary, K., Ikram, M., Imran, M., Haider, J., Khan, M., Khan, Q., & Maqbool, M. (2022). Synthesis of nanomaterials using various top-down and bottom-up approaches, influencing factors, advantages, and disadvantages: A review. *Advances in Colloid and Interface Science*, *300*, 102597. https://doi.org/https://doi.org/10.1016/j.cis.2021.102597

Addie, A. J., Ismail, R. A., & Mohammed, M. A. (2022). Amorphous carbon nitride dual-function anti-reflection coating for crystalline silicon solar cells. *Scientific Reports*, *12*(1), 9902. https://doi.org/10.1038/s41598-022-14078-0

Adeyinka, A. M., Mbelu, O. V., Adediji, Y. B., & Yahya, D. I. (2023). A review of current trends in thin film solar cell technologies. *Int. J. Energy Power Eng*, *17*(1), 1-10.

Ahmed, M., Ahmed, H., Adebayo, P., Carter, R., & Khanal, L. (2023). Mechanical Properties and Application of Graphite and Graphite-based Nanocomposite : A Review. *15*, 10-32. https://doi.org/10.7176/CMR/15-1-02

Aisenberg, S., & Chabot, R. (1971). Ion-beam deposition of thin films of diamondlike carbon. *Journal of applied physics*, *42*(7), 2953-2958.

Angelucci, R., Rizzoli, R., Salvatori, S., Nicoletti, S., Migliori, A., & Brugnoli, E. (2002). Amorphous carbon deposited by pulsed laser ablation as material for cold cathode flat emitters. *Applied Surface Science*, *186*(1), 423-428. https://doi.org/https://doi.org/10.1016/S0169-4332(01)00711-5

Astinchap, B., & Laelabadi, K. G. (2019). Effects of substrate temperature and precursor amount on optical properties and microstructure of CVD deposited amorphous TiO2 thin films. *Journal of Physics and Chemistry of Solids*, *129*, 217-226.

Awang, R., & Abd Aziz, S. A. (2019). Chemical Bonding Composition and Humidity Sensing Properties of a-CNx Thin Films by Low-Temperature rf-PECVD Technique.

Babu, R., Balakrishnan, G., Ramaswamy, S., Manavalan, S., & Song, J. (2016). Deposition and characterization of amorphous carbon thin film. *Carbon: Science and Technology*, *8*, 43-47.

Baqiya, M. A., Purwandari, E., Asih, R., Astuti, F., Nakajima, H., Ibrahim, A., & Wong, L. H. (2025). A brief review and prospect of amorphous carbon and reduced graphene oxides derived from biomass as a low cost and new photovoltaic cell. *Applied Surface Science*, 163203.

Baule, N., Tsu, D. V., Haubold, L., & Schuelke, T. (2024). The inner workings of sp2 clusters in nitrogen-incorporated tetrahedral amorphous carbon thin films according to optical analyses. *Diamond and Related Materials*, *145*, 111111. https://doi.org/https://doi.org/10.1016/j.diamond.2024.111111

Bhakta, P., & Barthunia, B. (2020). Fullerene and its applications: A review. *Journal of Indian Academy of Oral Medicine and Radiology*, *32*, 159. https://doi.org/10.4103/jiaomr.jiaomr_191_19

Bharadia, H. A., Shah, J. K., Sureja, D. K., Bodiwala, K. B., & Dhameliya, T. M. (2024). FUTURE OF ENVIRONMENT WITH CARBON ALLOTROPES. *Nirma University Journal of Pharmaceutical Sciences: Volume 11, Issue 1 (January-June 2024)*, 33.

Chen, T.-S., Hsueh, Y.-C., Chiou, S.-E., & Shiue, S.-T. (2015). The effect of the native silicon dioxide interfacial layer on photovoltaic characteristics of gold/p-type amorphous boron carbon thin film alloy/silicon dioxide/n-type silicon/aluminum solar cells. *Solar Energy Materials and Solar Cells*, *137*, 185-192.

Chen, X., Wang, C., Song, M., Ma, J., Ye, T., & Xia, W. (2019). The morphological transformation of carbon materials from nanospheres to graphene nanoflakes by thermal plasma. *Carbon*, *155*, 521-530. https://doi.org/https://doi.org/10.1016/j.carbon.2019.08.077

Choudhary, F., Mudgal, P., Parvez, A., Sharma, P., & Farooqi, H. (2024). A review on synthesis, properties and prospective applications of carbon nanomaterials. *Nano-Structures & Nano-Objects*, *38*, 101186.

Crespi, Â. E., Ballage, C., Hugon, M. C., Robert, J., Lundin, D., Vickridge, I., Alvarez, J., & Minea, T. (2020). Low resistivity amorphous carbon-based thin films employed as anti-reflective coatings on copper. *Thin Solid Films*, *712*, 138319.

Cui, T., Lv, R., Huang, Z.-H., Zhu, H., Jia, Y., Chen, S., Wang, K., Wu, D., & Kang, F.

(2012). Low-temperature synthesis of multilayer graphene/amorphous carbon hybrid films and their potential application in solar cells. *Nanoscale Research Letters*, *7*, 1-7.

Dadsetan, M., Latham, K. G., Kumral, B., Khan, M. F., Scott, M., Mitra, T., Naseri, A., Manzoor, S., Bobicki, E. R., Filleter, T., Titirici, M. M., & Thomson, M. J. (2023). Carbon film produced from microwave-driven methane pyrolysis. *Carbon Trends*, *12*, 100283. https://doi.org/https://doi.org/10.1016/j.cartre.2023.100283

Dai, H. Y., Zhan, C., & Du, J. (2015). Studies on the influence of sputtering power on amorphous carbon films deposited by pulsed unbalanced magnetron sputtering. *Optik - International Journal for Light and Electron Optics*, *127*. https://doi.org/10.1016/j.ijleo.2015.11.154

Das, S. C., Hossain, J., Rahman, M. M., & Talukder, M. R. (2025). Synthesis of amorphous carbon (aC) thin films from the iodomethane chemical route by PE-CVD method for optoelectronic devices. *Diamond and Related Materials*, *154*, 112173.

Dayana, K., Fadzilah, A. N., Noor, U. M., & Rusop, M. (2012, 19-21 Sept. 2012). Electrical and optical properties of iodine doped amorphous carbon thin film by Thermal CVD. 2012 10th IEEE International Conference on Semiconductor Electronics (ICSE),

Dhameliya, T. M., Bharadia, H. A., Shah, J. K., Sureja, D. K., & Bodiwala, K. B. (2024). Future of environment with carbon allotropes. *Nirma University Journal of Pharmaceutical Sciences*, *11*(1), 33-54.

Dos Santos, E. J., Pereira, M. L., Tromer, R. M., Galvão, D. S., & Ribeiro, L. A. (2025). Exploring the electronic and mechanical properties of the recently synthesized nitrogen-doped amorphous monolayer carbon. *Nanoscale*, *17*(12), 7253-7263.

Dychalska, A., Fabisiak, K., Paprocki, K., Koczorowski, W., Trzcinski, M., & Szybowicz, M. (2019). The effect of low temperature thermal treatment on structural and chemical composition of a-C film with nc-G admixture studied by Raman spectroscopy. *Diamond and Related Materials*, *95*, 44-54. https://doi.org/https://doi.org/10.1016/j.diamond.2019.03.016

Egorov, A. V., Andreychev, V. V., Putilin, F. N., Meshkov, G. B., Parshina, L. S., Khramova, O. D., Novodvorsky, O. A., Shchur, P. A., & Savilov, S. V. (2021). Single stage synthesis of amorphous carbon covered nanotubes arrays. *Carbon*

Trends, *5*, 100099. https://doi.org/https://doi.org/10.1016/j.cartre.2021.100099

Elhusseiny, S. M., El-Mahdy, T. S., Awad, M. F., Elleboudy, N. S., Farag, M. M. S., Yassein, M. A., & Aboshanab, K. M. (2021). Proteome Analysis and In Vitro Antiviral, Anticancer and Antioxidant Capacities of the Aqueous Extracts of Lentinula edodes and Pleurotus ostreatus Edible Mushrooms. *Molecules*, *26*(15). https://doi.org/10.3390/molecules26154623

Endrino, J. L., Horwat, D., Anders, A., Andersson, J., & Gago, R. (2009). Impact of annealing on the conductivity of amorphous carbon films incorporating copper and gold nanoparticles deposited by pulsed dual cathodic arc. *Plasma Processes and Polymers*, *6*(S1), S438-S443.

Etula, J., Wester, N., Liljestrom, T., Sainio, S., Palomaki, T., Arstila, K., Sajavaara, T., Koskinen, J., Caro, M. A., & Laurila, T. (2021). What determines the electrochemical properties of nitrogenated amorphous carbon thin films? *Chemistry of Materials*, *33*(17), 6813-6824.

Fadzilah, A., Dayana, K., & Rusop, M. (2013). Fabrication and characterization of camphor-based amorphous carbon thin films. *Procedia Engineering*, *56*, 743-749.

Fadzilah, A., Kamaruzaman, D., Siran, Y. M., Syahril Anuar, M. R., Asis, A. J., Syawaluddin, T., & Mahmood, M. R. (2014b). Influence of Deposition Time on Amorphous Carbon Thin Films Performance with Aerosol-Assisted Chemical Vapor Deposition. *Advanced Materials Research*, *832*, 712-717.

Fathy, M., Moghny, T. A., Mousa, M. A., El-Bellihi, A.-H. A., & Awadallah, A. E. (2017). Synthesis of transparent amorphous carbon thin films from cellulose powder in rice straw. *Arabian Journal for Science and Engineering*, *42*(1), 225-233.

Ferreira-Dias, S., Valente, D., & Abreu, J. (2003). Comparison between ethanol and hexane for oil extraction from Quercus suber L. fruits. *Grasas y Aceites*, *54*. https://doi.org/10.3989/gya.2003.v54.i4.225

Gabhi, R., Basile, L., Kirk, D. W., Giorcelli, M., Tagliaferro, A., & Jia, C. Q. (2020). Electrical conductivity of wood biochar monoliths and its dependence on pyrolysis temperature. *Biochar*, *2*, 369-378.

Gaudiuso, R. (2023). Pulsed laser deposition of carbon-based materials: a focused review of methods and results. *Processes*, *11*(8), 2373.

Gesesse, G. D., Gomis-Berenguer, A., Barthe, M.-F., & Ania, C. O. (2020). On the

analysis of diffuse reflectance measurements to estimate the optical properties of amorphous porous carbons and semiconductor/carbon catalysts. *Journal of Photochemistry and Photobiology A: Chemistry*, *398*, 112622. https://doi.org/https://doi.org/10.1016/j.jphotochem.2020.112622

Ghimire, D. C., Adhikari, S., Aryal, H., Mominuzzamn, S., Soga, T., Jimbo, T., Uchida, H., & Umeno, M. (2008). Effects of ethylene gas flow rate on optoelectrical properties of nitrogenated thin amorphous carbon films grown by microwave surface wave plasma CVD. *Diamond and Related Materials*, *17*(7-10), 1724-1727.

Gunasekaran, S., Govindan, S., & Ramani, P. (2021). Sulfated modification, characterization and bioactivities of an acidic polysaccharide fraction from an edible mushroom Pleurotus eous (Berk.) Sacc. *Heliyon*, *7*(1), e05964. https://doi.org/https://doi.org/10.1016/j.heliyon.2021.e05964

Hanafi, F., Rezania, S., Mat Taib, S., Md Din, M. F., Yamauchi, M., Sakamoto, M., Hara, H., Park, J., & Shafiei Ebrahimi, S. (2018). Environmentally sustainable applications of agro-based spent mushroom substrate (SMS): an overview. *Journal of Material Cycles and Waste Management*, *20*, 1383–1396. https://doi.org/10.1007/s10163-018-0739-0

He, H., Zhang, R., Zhang, P., Wang, P., Chen, N., Qian, B., Zhang, L., Yu, J., & Dai, B. (2023). Functional carbon from nature: biomass-derived carbon materials and the recent progress of their applications. *Advanced Science*, *10*(16), 2205557.

Henksmeier, T., Mahler, P., Wolff, A., Deutsch, D., Voigt, M., Ruhm, L., Sanchez, A. M., As, D. J., Grundmeier, G., & Reuter, D. (2024). Low-temperature fabrication of amorphous carbon films as a universal template for remote epitaxy. *Communications Materials*, *5*(1), 276. https://doi.org/10.1038/s43246-024-00718-7

Hoffmann, R., Kabanov, A. A., Golov, A. A., & Proserpio, D. M. (2016). Homo citans and carbon allotropes: for an ethics of citation. *Angewandte Chemie International Edition*, *55*(37), 10962-10976.

Honglertkongsakul, K., May, P., & Paosawatyanyong, B. (2010). Electrical and optical properties of diamond-like carbon films deposited by pulsed laser ablation. *Diamond and Related Materials*, *19*(7-9), 999-1002.

Hoque, M. K., Behan, J. A., Stamatin, Serban N., Zen, F., Perova, T. S., & Colavita, P. E. (2019). Capacitive storage at nitrogen doped amorphous carbon electrodes:

structural and chemical effects of nitrogen incorporation [10.1039/C8RA10187F]. *RSC Advances*, *9*(7), 4063-4071. https://doi.org/10.1039/C8RA10187F

Hughes, K. J., Iyer, K. A., Bird, R. E., Ivanov, J., Banerjee, S., Georges, G., & Zhou, Q. A. (2024). Review of carbon nanotube research and development: materials and emerging applications. *ACS Applied Nano Materials*, *7*(16), 18695-18713.

Ianni, F., Blasi, F., Angelini, P., Simone, S. C. D., Angeles Flores, G., Cossignani, L., & Venanzoni, R. (2021). Extraction Optimization by Experimental Design of Bioactives from Pleurotus ostreatus and Evaluation of Antioxidant and Antimicrobial Activities. *Processes*, *9*(5), 743. https://www.mdpi.com/2227-9717/9/5/743

Ikon, G., Udobre, E., Etang, U., Ekanemesang, U., Ebana, R., & Edet, U. (2018). Phytochemical Screening, Proximate Composition and Antibacterial Activity of Oyster Mushroom, Pleurotus ostreatus Collected from Etim Ekpo in Akwa Ibom State, Nigeria. *Asian Food Science Journal*, *6*, 1-10. https://doi.org/10.9734/AFSJ/2019/45956

Ishak, A., Dayana, K., Mamat, M., Malek, M., & Rusop, M. (2015). Nano-structured amorphous carbon films using novel palm oil precursor for solar cell applications. *Optik*, *126*(18), 1610-1612.

Ishak, A., Dayana, K., & Rusop, M. (2013). Surface morphology and compositional analysis of undoped amorphous carbon thin films via bias assisted pyrolysis-CVD. *Advanced Materials Research*, *667*, 468-476.

Ishak, A., Dayana, K., Saurdi, I., Malek, M., & Rusop, M. (2018). Hydrogenated nanostructure boron doped amorphous carbon films by DC bias. IOP Conference Series: Materials Science and Engineering,

Ismail, M. S., Yusof, N., Yusop, M. Z. M., Ismail, A. F., Jaafar, J., Aziz, F., & Karim, Z. A. (2019). Synthesis and characterization of graphene derived from rice husks. *Malays. J. Fundam. Appl. Sci*, *15*, 516-521.

Ismail, R. A., Hamoudi, W. K., & Saleh, K. K. (2014). Effect of rapid thermal annealing on the characteristics of amorphous carbon/n-type crystalline silicon heterojunction solar cells. *Materials Science in Semiconductor Processing*, *21*, 194-199.

Jaisi, B. P., Zhu, R., Kalita, G., & Umeno, M. (2023). Morphological changes of carbon thin films with nitrogen doping synthesized by microwave-excited surface wave

plasma CVD. *Materials Chemistry and Physics*, *307*, 128183. https://doi.org/https://doi.org/10.1016/j.matchemphys.2023.128183

Jara, A. D., Betemariam, A., Woldetinsae, G., & Kim, J. Y. (2019). Purification, application and current market trend of natural graphite: A review. *International Journal of Mining Science and Technology*, *29*(5), 671-689. https://doi.org/https://doi.org/10.1016/j.ijmst.2019.04.003

Jhaa, G., Pancharatna, P. D., & Balakrishnarajan, M. M. (2023). Topological Impact of Delocalization on the Stability and Band Gap of Partially Oxidized Graphene. *ACS Omega*, *8*(5), 5124-5135. https://doi.org/10.1021/acsomega.2c08169

Judai, K., Iguchi, N., & Hatakeyama, Y. (2016). Low-Temperature Production of Genuinely Amorphous Carbon from Highly Reactive Nanoacetylide Precursors. *Journal of Chemistry*, *2016*(1), 7840687.

Kamaruzaman, D., Fadzilah, A., & Rusop, M. (2012). The Effect of Camphor Oil Amounts on the Properties of Amorphous Carbon Thin Films by Thermal Chemical Vapor Deposition. *Advanced Materials Research*, *576*, 611-614.

Kamaruzaman, D., Fadzilah, A. N., Annuar, I., Siran, Y., Rejab, S., Asis, A., Tahirruddin, S., & Rusop, M. (2013). Effect of Gas Flow Rate on the Properties of Amorphous Carbon Thin Films Prepared by Thermal CVD Using Camphoric Carbon Precursor. *Advanced Materials Research*, *832*, 423-428. https://doi.org/10.4028/www.scientific.net/AMR.832.423

Kamaruzaman, D., Rosly, M. A., Annuar, I., Ahmad, N., & Mahmood, M. R. (2020). Deposition and characterization of amorphous carbon thin film by thermal CVD. Journal of Physics: Conference Series,

Kang, J., Yang, X., Hu, Q., Cai, Z., Liu, L.-M., & Guo, L. (2023). Recent Progress of Amorphous Nanomaterials. *Chemical Reviews*, *123*(13), 8859-8941. https://doi.org/10.1021/acs.chemrev.3c00229

Kaushal, S., & Andrews, J. (2025). A review on the nitrogenated carbon materials and their electrochemical performance for energy storage applications. *International Journal of Hydrogen Energy*, *100*, 1231-1245. https://doi.org/https://doi.org/10.1016/j.ijhydene.2024.12.202

Kayed, K. (2024). Water adsorption on amorphous carbon nitride thin films synthesized by pulsed laser deposition. *Adsorption*, *30*(6), 1205-1212. https://doi.org/10.1007/s10450-024-00500-8

Keller, B. D., Ferralis, N., & Grossman, J. C. (2016). Rethinking coal: thin films of

solution processed natural carbon nanoparticles for electronic devices. *Nano Letters*, *16*(5), 2951-2957.

Kim, J.-H., Kim, H.-G., & Kwac, L.-K. (2021). High-efficient Schottky-junction silicon solar cell using silver nanowires covering nitrogen-doped amorphous carbon. *Current Applied Physics*, *26*, 1-8.

Kim, S., Jeong, M.-W., Kim, K., Kim, U.-g., Kim, M., Lee, S.-Y., & Joo, Y.-C. (2023). Effect of N doping on the microstructure and dry etch properties of amorphous carbon deposited with a DC sputtering system [10.1039/D2RA06808G]. *RSC Advances*, *13*(3), 2131-2139. https://doi.org/10.1039/D2RA06808G

Koós, M., Moustafa, S. H. S., Szilágyi, E., & Pócsik, I. (1999). Non-Arrhenius temperature dependence of direct-current conductivity in amorphous carbon (a-C:H) above room temperature. *Diamond and Related Materials*, *8*(10), 1919-1926. https://doi.org/https://doi.org/10.1016/S0925-9635(99)00165-X

Kothandam, G., Singh, G., Guan, X., Lee, J. M., Ramadass, K., Joseph, S., Benzigar, M., Karakoti, A., Yi, J., & Kumar, P. (2023). Recent Advances in Carbon-Based Electrodes for Energy Storage and Conversion. *Advanced Science*, *10*(18), 2301045.

Kouider, W. H., Belfar, A., BelmekkiI, M., & Ait-Kaci, H. (2020). Window layer thickness effect on amorphous silicon oxide solar cell performances. *Journal: Algerian Journal of Renewable Energy and Sustainable Development*, *2*(1), 67-74.

Kroto, H. W., Heath, J. R., O'Brien, S. C., Curl, R. F., & Smalley, R. E. (1985). C60: Buckminsterfullerene. *Nature*, *318*(6042), 162-163. https://doi.org/10.1038/318162a0

Kumar, D. R., Singh, D. R., & Singh, D. (2016). Natural and waste hydrocarbon precursors for the synthesis of carbon based nanomaterials: Graphene and CNTs. *Renewable and Sustainable Energy Reviews*, *58*, 976. https://doi.org/10.1016/j.rser.2015.12.120

Kumar, S., Aziz, S. K. T., Girshevitz, O., & Nessim, G. D. (2018). One-Step Synthesis of N-Doped Graphene Quantum Dots from Chitosan as a Sole Precursor Using Chemical Vapor Deposition. *The Journal of Physical Chemistry C*, *122*(4), 2343-2349. https://doi.org/10.1021/acs.jpcc.7b05494

Kumar, S., Dwivedi, N., Rauthan, C. M. S., & Panwar, O. S. (2010). Properties of nitrogen diluted hydrogenated amorphous carbon (n-type a-C:H) films and their

realization in n-type a-C:H/p-type crystalline silicon heterojunction diodes. *Vacuum*, *84*(7), 882-889. https://doi.org/https://doi.org/10.1016/j.vacuum.2009.12.003

Lee, J.-E., Jayakody, J. T. M., Kim, J.-I., Jeong, J.-W., Choi, K.-M., Kim, T.-S., Seo, C., Azimi, I., Hyun, J., & Ryu, B. (2024). The Influence of Solvent Choice on the Extraction of Bioactive Compounds from Asteraceae: A Comparative Review. *Foods*, *13*(19), 3151. https://www.mdpi.com/2304-8158/13/19/3151

Li, D., Tian, F., Chu, B., Duan, D., Sha, X., Lv, Y., Zhang, H., Lu, N., Liu, B., & Cui, T. (2015). Ab initio structure determination of n-diamond. *Scientific Reports*, *5*(1), 13447. https://doi.org/10.1038/srep13447

Li, H., Guo, P., Zhang, D., Chen, R., Zuo, X., Ke, P., Saito, H., & Wang, A. (2020). Influence of deposition temperature on the structure, optical and electrical properties of a-C films by DCMS. *Applied Surface Science*, *503*, 144310. https://doi.org/https://doi.org/10.1016/j.apsusc.2019.144310

Li, L., An, B., Lahiri, A., Wang, P., & Fang, Y. (2013). Doublet of D and 2D bands in graphene deposited with Ag nanoparticles by surface enhanced Raman spectroscopy. *Carbon*, *65*, 359-364. https://doi.org/https://doi.org/10.1016/j.carbon.2013.08.039

Li, M., Jiang, L., Sun, Y., Xiao, T., Xiang, P., & Tan, X. (2018). Silicon content influence on structure and photoluminescence properties of carbon rich hydrogenated amorphous silicon carbide thin films. *Journal of Alloys and Compounds*, *753*, 320-328.

Liang, Z., Ma, M., Zhou, Y., Tong, K., Zhang, Y., Li, P., Li, P., Shen, T., Wang, X., Zhang, W., Chen, S., Li, B., Liu, B., Wu, Y., He, J., & Zhao, Z. (2025). Amorphous carbon reinforced graphite combining high strength and superior electrical conductivity. *Carbon*, *244*, 120651. https://doi.org/https://doi.org/10.1016/j.carbon.2025.120651

Lin, S., Xie, D., Tang, Y., Wang, Y., Jing, F., Huang, N., & Leng, Y. (2021). Effect of nitrogen flow on the properties of carbon nitride films deposited by electron cyclotron resonance plasma-enhanced chemical vapor deposition. *Vacuum*, *189*, 110223. https://doi.org/https://doi.org/10.1016/j.vacuum.2021.110223

Liu, W.-J., Chang, Y.-H., Chiang, C.-C., Hsu, S.-T., Fern, C.-L., Chen, Y.-T., Ma, S.-S., Wang, W.-K., & Lin, S.-H. (2024). Influence of surface roughness and annealing on the structural, optical, electrical, and magnetic properties of

Co40Fe40Dy20 thin films deposited on glass substrate. *Ceramics International*, *50*(21, Part A), 40678-40689. https://doi.org/https://doi.org/10.1016/j.ceramint.2024.05.209

Maarof, S., Ali, A. A., & Hashim, A. M. (2019). Synthesis of Large-Area Single-Layer Graphene Using Refined Cooking Palm Oil on Copper Substrate by Spray Injector-Assisted CVD. *Nanoscale Research Letters*, *14*(1), 143. https://doi.org/10.1186/s11671-019-2976-0

Marton, M., Vojs, M., Zdravecká, E., Himmerlich, M., Haensel, T., Krischok, S., Kotlár, M., Michniak, P., Veselý, M., & Redhammer, R. (2013). Raman Spectroscopy of Amorphous Carbon Prepared by Pulsed Arc Discharge in Various Gas Mixtures. *Journal of Spectroscopy*, *2013*(1), 467079. https://doi.org/https://doi.org/10.1155/2013/467079

Mi, B., Chen, T., Zhang, J., Ma, X., Wang, J., Liu, P., Wang, H., & Li, W. (2024). Effect of N doping on Cr-doped amorphous carbon /CrN /Ti multilayer coatings on 316L stainless steel bipolar plate for PEMFC: First principles calculation, structure and performance. *International Journal of Hydrogen Energy*, *71*, 1303-1316. https://doi.org/https://doi.org/10.1016/j.ijhydene.2024.05.294

Minglei, W., Zhang, L., Wenqi, L., & Guoqiang, L. (2023). Plasma diagnosis of tetrahedral amorphous carbon films by filtered cathodic vacuum arc deposition. *Plasma Science and Technology*, *25*(6), 065506.

Mitra, S., Hamada, N., & Mitra, S. K. (2024). Experimental observation and characterization of amorphous carbon generated in graphene on gold nanoparticles. *RSC Advances*, *14*(35), 25307-25315.

Mohagheghpour, E., Rajabi, M., Gholamipour, R., Larijani, M. M., & Sheibani, S. (2016). Correlation study of structural, optical and electrical properties of amorphous carbon thin films prepared by ion beam sputtering deposition technique. *Applied Surface Science*, *360*, 52-58. https://doi.org/https://doi.org/10.1016/j.apsusc.2015.10.213

Moseenkov, S. I., Kuznetsov, V. L., Zolotarev, N. A., Kolesov, B. A., Prosvirin, I. P., Ishchenko, A. V., & Zavorin, A. V. (2023). Investigation of Amorphous Carbon in Nanostructured Carbon Materials (A Comparative Study by TEM, XPS, Raman Spectroscopy and XRD). *Materials*, *16*(3), 1112. https://www.mdpi.com/1996-1944/16/3/1112

Moubark, M., Moghny, T., Mousa, M., El-Bellihi, A.-H., & Awadallah, A. (2016).

Synthesis of Transparent Amorphous Carbon Thin Films from Cellulose Powder in Rice Straw. *Arabian Journal for Science and Engineering*, *42*. https://doi.org/10.1007/s13369-016-2273-5

Murahari, P., Fernandes, B. J., Kumar, K. D. A., Simon, R. F., & Ramesh, K. (2020). Carbon nitride for photovoltaic applications. *AIP Conference Proceedings*, *2265*(1). https://doi.org/10.1063/5.0016717

Mwangi, R. W., Mustafa, M., Kappel, N., Csambalik, L., & Szabó, A. (2024). Practical applications of spent mushroom compost in cultivation and disease control of selected vegetables species. *Journal of Material Cycles and Waste Management*, *26*(4), 1918-1933. https://doi.org/10.1007/s10163-024-01969-9

Nikolova, M. P., & Tzvetkov, I. (2025). Influence of Deposition Temperature on Microstructure and Properties of Tantalum Oxide Sputtered Coatings. *Materials*, *18*(9), 1895. https://www.mdpi.com/1996-1944/18/9/1895

Nurdiyanto, M. (2022). APPLICATIONS OF SCANNING ELECTRON MICROSCOPY-ENERGY DISPERSIVE X-RAY SPECTROSCOPY (SEM-EDS) IN EARTH SCIENCES.

Ohtake, N., Hiratsuka, M., Kanda, K., Akasaka, H., Tsujioka, M., Hirakuri, K., Hirata, A., Ohana, T., Inaba, H., & Kano, M. (2021). Properties and classification of diamond-like carbon films. *Materials*, *14*(2), 315.

Ono, S., Hwang, S.-H., Okumura, T., Yamashita, N., Kamataki, K., Kiyama, H., Itagaki, N., Koga, K., & Shiratani, M. (2024). Effects of carbon nanoparticle insertion on stress reduction in hydrogenated amorphous carbon films using plasma chemical vapor deposition. *Diamond and Related Materials*, *150*, 111654.

Orlando, A., Franceschini, F., Muscas, C., Pidkova, S., Bartoli, M., Rovere, M., & Tagliaferro, A. (2021). A comprehensive review on Raman spectroscopy applications. *Chemosensors*, *9*(9), 262.

Ouyang, D.-d., Hu, L.-b., Wang, G., Dai, B., Yu, F., & Zhang, L.-l. (2021). A review of biomass-derived graphene and graphene-like carbons for electrochemical energy storage and conversion. *New Carbon Materials*, *36*(2), 350-372. https://doi.org/https://doi.org/10.1016/S1872-5805(21)60024-0

Pamungkas, D. I., Mukarromah, M., Priyanto, B., Nakajima, H., Tunmee, S., & Darminto, D. (2019). Structural analysis and electrical properties of amorphous carbon thin films. Materials Science Forum,

Panickar, R., Sobhan, C. B., & Chakravorti, S. (2020). Chemical vapor deposition

synthesis of carbon spheres: Effects of temperature and hydrogen. *Vacuum*, *172*, 109108. https://doi.org/https://doi.org/10.1016/j.vacuum.2019.109108

Park, S. J., Kim, D., Baek, S. Y., Lee, C., Kim, J., Roh, S., Park, J., Kyung, S., & Choi, C. (2025). Nitrogen doped high selectivity amorphous carbon film for high aspect ratio etch process. *Thin Solid Films*, *809*, 140582. https://doi.org/https://doi.org/10.1016/j.tsf.2024.140582

Patsalas, P. (2011). Optical properties of amorphous carbons and their applications and perspectives in photonics. *Thin Solid Films*, *519*(12), 3990-3996. https://doi.org/https://doi.org/10.1016/j.tsf.2011.01.202

Phan, C.-W., & Sabaratnam, V. (2012). Potential uses of spent mushroom substrate and its associated lignocellulosic enzymes. *Applied Microbiology and Biotechnology*, *96*(4), 863-873. https://doi.org/10.1007/s00253-012-4446-9

Podder, J., Rusop, M., Soga, T., & Jimbo, T. (2005). Boron doped amorphous carbon thin films grown by r.f. PECVD under different partial pressure. *Diamond and Related Materials*, *14*(11), 1799-1804. https://doi.org/https://doi.org/10.1016/j.diamond.2005.07.020

Pradhan, D., & Sharon, M. (2007). Opto-electrical properties of amorphous carbon thin film deposited from natural precursor camphor. *Applied Surface Science*, *253*(17), 7004-7010.

Prasad, W., Wani, A. D., Khamrui, K., Hussain, S. A., & Khetra, Y. (2022). Green solvents, potential alternatives for petroleum based products in food processing industries. *Cleaner Chemical Engineering*, *3*, 100052. https://doi.org/https://doi.org/10.1016/j.clce.2022.100052

Priyanto, B., Asih, R., Ardiani, I. S., Laila, A. Z., Nadiyyah, K., Romadhon, B., Tunmee, S., Nakajima, H., & Cahyono, Y. (2021). Hydrogenated amorphous carbon films from palmyra sugar. *Journal of Renewable Materials*, *9*(6), 1087-1098.

Priyanto, B., Khambali, I., Ardiani, I. S., Nadhiyah, K., Laila, A. Z., Hasani, M. C., Romadhon, B., Asih, R., & Cahyono, Y. (2024). Nitrogen-Doped Amorphous Carbon Homojunction from Palmyra Sugar as a Renewable Solar Cell. *Journal of Renewable Materials*, *12*(1).

Priyanto, B., Saleh, M., Tunmee, S., Euaruksakul, C., Cahyono, Y., Triwikantoro, T., & Darminto, D. (2019). Fabrication of Amorphous Carbon Thin Film from CH4 Using PEVCD. *Materials Science Forum*, *966*, 95-99.

https://doi.org/10.4028/www.scientific.net/MSF.966.95

Purwandari, E., Asih, R., Sudarsono, Anggoro, D., Priyanto, B., Timuda, G. E., Baqiya, M. A., Santoso, I., Nakajima, H., Ramli, M. M., Subekti, A., & Darminto. (2025). Semiconducting biomass-based amorphous carbon films and their potential application in photovoltaic devices. *Materials Science in Semiconductor Processing*, *187*, 109122. https://doi.org/https://doi.org/10.1016/j.mssp.2024.109122

Rajanna, P. M., Lund, P. D., & Nasibulin, A. G. (2022). Hybrid heterojunction solar cells based on single-walled carbon nanotubes and amorphous silicon thin films. *Wiley Interdisciplinary Reviews: Energy and Environment*, *11*(1), e402.

Rana, D. S., Sharma, R., Awasthi, A., Singh, D., & Sharma, A. (2025). Biomass-derived phosphorus-doped nanocarbon: A metal-free electrode for high-performance supercapacitors. *Journal of Energy Storage*, *131*, 117586.

Rane, K., Adams, J. J., Thode, J. M., Leonard, B. M., Huo, J., & Goual, L. (2021). Multistep Fractionation of Coal and Application for Graphene Synthesis. *ACS Omega*, *6*(25), 16573-16583. https://doi.org/10.1021/acsomega.1c01614

Ray, S. C., Mbiombi, W., & Papakonstantinou, P. (2014). Electrical and electronic properties of nitrogen doped amorphous carbon (a-CNx) thin films. *Current Applied Physics*, *14*(12), 1845-1848. https://doi.org/https://doi.org/10.1016/j.cap.2014.10.016

Rivera, A. D., Hershkovitz, E., Panoutsopoulos, P., de Jesus Lopez, M. X., Simpson, B., Kim, H., Narayanan, R., Johnson, J., & Jones, K. S. (2025). Pulsed Laser Annealing of Deposited Amorphous Carbon Films. *C*, *11*(3), 60. https://www.mdpi.com/2311-5629/11/3/60

Robaiah, M., Asli, N. A., Abdul Rani, R., Abdullah, W. F. H., Khusaimi, Z., Azhan, H., Abdullah, S., & Rusop, M. (2023). A PMMA-assisted transfer method of waste cooking palm oil based multi-layered graphene from a nickel substrate onto a glass substrate for the development of a humidity sensor. *Journal of Materials Science: Materials in Electronics*, *34*(16), 1287. https://doi.org/10.1007/s10854-023-10591-8

Roberts, O., Lethole, N. L., & Mukumba, P. (2025). Insights into the structural, thermodynamic, electronic, and mechanical properties of CaMn2O4 polymorphs via density functional theory analysis. *Theoretical Chemistry Accounts*, *144*(5), 32. https://doi.org/10.1007/s00214-025-03185-6

Roy, A., Wang, S., & Komvopoulos, K. (2023). A review of plasma-assisted deposition methods for amorphous carbon thin and ultrathin films with a focus on the cathodic vacuum arc technique. *Journal of Materials Research*, *38*(3), 586-616.

Roy, D., Kanojia, S., Mukhopadhyay, K., & Eswara Prasad, N. (2021). Analysis of carbon-based nanomaterials using Raman spectroscopy: principles and case studies. *Bulletin of Materials Science*, *44*(1), 31.

Roy Das, A., Das, P., Bhattacharjee, S., & Saha, A. (2014). Chemical analysis of a wild edible mushroom: Pleurotus djamor (Rumph. ex Fr.) Boedijn. *23*, 161-166.

Rusli, L., & Jaludin, N. (2025). THE EFFECTS OF SPENT MUSHROOM COMPOST ON PLANT GROWTH PERFORMANCE AND SOIL PROPERTIES ON Amaranthus tricolor. *Journal of Academia*, *13*, 127-140. https://doi.org/10.24191/joa.v13i2.6884

Rusop, M., Omer, A., Adhikari, S., Adhikary, S., Uchida, H., Soga, T., Jimbo, T., & Umeno, M. (2006). Effects of annealing temperature on the optical, bonding, structural and electrical properties of nitrogenated amorphous carbon thin films grown by surface wave microwave plasma chemical vapor deposition. *Journal of Materials Science*, *41*, 537-547. https://doi.org/10.1007/s10853-005-2635-y

Saeed, M., Alshammari, Y., Majeed, S. A., & Al-Nasrallah, E. (2020). Chemical Vapour Deposition of Graphene—Synthesis, Characterisation, and Applications: A Review. *Molecules*, *25*(17).

Saleemi, A. S., Hafeez, M., Saeed, M., Abdullah, A., Rehman, M. A., & Lee, S. L. (2021). Substrate Impact on MR Characteristics of Carbon Nano Films Explored via AFM and Raman Analysis. *Materials (Basel)*, *14*(13). https://doi.org/10.3390/ma14133649

Salek, A. G., Le, P. Y., Partridge, J. G., Raeber, T. J., Haberl, B., Boehler, R., Murdoch, B. J., Bradby, J. E., Ratcliff, T., Elliman, R. G., McKenzie, D. R., & McCulloch, D. G. (2023). The structure and electronic properties of tetrahedrally bonded hydrogenated amorphous carbon. *Applied Physics Letters*, *122*(18). https://doi.org/10.1063/5.0147494

Saputri, D., Jan'ah, A., & Saraswati, T. (2020). Synthesis of carbon nanotubes (CNT) by chemical vapor deposition (CVD) using a biogas-based carbon precursor: a review. IOP Conference Series: Materials Science and Engineering,

Silva, S. R. P., Robertson, J., Amaratunga, G. A. J., Rafferty, B., Brown, L. M., Schwan, J., Franceschini, D. F., & Mariotto, G. (1997). Nitrogen modification of

hydrogenated amorphous carbon films. *Journal of applied physics*, *81*(6), 2626-2634. https://doi.org/10.1063/1.363927

Skowronski, L., Chodun, R., Trzcinski, M., & Zdunek, K. (2023). Optical Properties of Amorphous Carbon Thin Films Fabricated Using a High-Energy-Impulse Magnetron-Sputtering Technique. *Materials (Basel)*, *16*(21). https://doi.org/10.3390/ma16217049

Solovyev, A. A., Oskomov, K. V., Grenadyorov, A. S., & Maloney, P. D. (2018). Preparation of nickel-containing conductive amorphous carbon films by magnetron sputtering with negative high-voltage pulsed substrate bias. *Thin Solid Films*, *650*, 37-43. https://doi.org/https://doi.org/10.1016/j.tsf.2018.02.013

Song, Y., Han, C., Zhen, N., Wang, Y., Leng, Y., Wu, Z., Deng, Q., & Wen, F. (2024). Nitrogen-Doped Diamond-like Carbon Buffer Layer Enhances the Mechanical and Tribological Properties of Diamond-like Carbon Films Deposited on Nitrile Rubber Substrate. *Coatings*, *14*(4), 515. https://www.mdpi.com/2079-6412/14/4/515

Sportelli, M. C., Izzi, M., Volpe, A., Clemente, M., Picca, R. A., Ancona, A., Lugarà, P. M., Palazzo, G., & Cioffi, N. (2018). The Pros and Cons of the Use of Laser Ablation Synthesis for the Production of Silver Nano-Antimicrobials. *Antibiotics*, *7*(3), 67. https://www.mdpi.com/2079-6382/7/3/67

Sun, J., Tang, Y., Xu, X., Li, Z., & Su, F. (2022). Synthesis of Nitrogen-Doped Diamond-Like Carbon Films Produced by Plasma-Enhanced Chemical Vapor Deposition and their Tribocorrosion Behavior in Hanks' Solution. *Journal of Materials Engineering and Performance*, *31*(10), 8334-8345. https://doi.org/10.1007/s11665-022-06984-1

Tagkouli, D., Bekiaris, G., Pantazi, S., Anastasopoulou, M. E., Koutrotsios, G., Mallouchos, A., Zervakis, G. I., & Kalogeropoulos, N. (2021). Volatile Profiling of Pleurotus eryngii and Pleurotus ostreatus Mushrooms Cultivated on Agricultural and Agro-Industrial By-Products. *Foods*, *10*(6), 1287. https://www.mdpi.com/2304-8158/10/6/1287

Tali, S. A. S., Soleimani-Amiri, S., Sanaee, Z., & Mohajerzadeh, S. (2017). Nitrogen-doped amorphous carbon-silicon core-shell structures for high-power supercapacitor electrodes. *Scientific Reports*, *7*(1), 42425. https://doi.org/10.1038/srep42425

Thangaraj, B., Mumtaz, F., Abbas, Y., Anjum, D. H., Solomon, P. R., & Hassan, J. (2023). Synthesis of Graphene Oxide from Sugarcane Dry Leaves by Two-Stage Pyrolysis. *Molecules*, *28*(8), 3329. https://www.mdpi.com/1420-3049/28/8/3329

Toh, C.-T., Zhang, H., Lin, J., Mayorov, A. S., Wang, Y.-P., Orofeo, C. M., Ferry, D. B., Andersen, H., Kakenov, N., & Guo, Z. (2020). Synthesis and properties of free-standing monolayer amorphous carbon. *Nature*, *577*(7789), 199-203.

Torres, S., Frattini, G., Silva, L. I., Repetto, C. E., Aguirre, A., Gómez, B. J., & Dobry, A. (2024). Microstructure evolution of carbon films, grown by physical vapor deposition, when substrate temperature is increased. *Materials Chemistry and Physics*, *322*, 129529. https://doi.org/https://doi.org/10.1016/j.matchemphys.2024.129529

Torrisi, L., Torrisi, A., & Cutroneo, M. (2024). IR Pulsed Laser Ablation of Carbon Materials in High Vacuum. *Applied Sciences*, *14*(24), 11744. https://www.mdpi.com/2076-3417/14/24/11744

Tu, X., Qing, F., Liu, F., Shen, C., & Li, X. (2025). Synthesis of large-area uniform amorphous monolayer carbon with low dielectric constant and high thermal stability. *Carbon*, 120413.

Valcheva, E., Kirilov, K., Dikovska, A., & Milenov, T. (2023). Low temperature electrical transport in thin carbon films deposited on SiO2/Si substrates by pulsed laser deposition. Journal of Physics: Conference Series,

Wan-Mohtar, W., Halim-Lim, S. A., Kamarudin, N. Z., Rukayadi, Y., Abd Rahim, M. H., Jamaludin, A. A., & Ilham, Z. (2020). Fruiting-body-base flour from an Oyster mushroom waste in the development of antioxidative chicken patty. *J Food Sci*, *85*(10), 3124-3133. https://doi.org/10.1111/1750-3841.15402

Wang, J., Zhang, X., Wan, C., Vanacken, J., & Moshchalkov, V. V. (2013). Magnetotransport properties of undoped amorphous carbon films. *Carbon*, *59*, 278-282. https://doi.org/https://doi.org/10.1016/j.carbon.2013.03.019

Wang, P., Wang, D., Chen, C., Sun, L., Zhang, X., Guo, X., Yu, F., Cheng, X., Xie, X., & Zhao, X. (2024). Effect of Ar on Temperature and Flow Distribution in Monocrystalline Graphene Growth: Inert Gas Is Active. *ACS Omega*, *9*(52), 51146-51156. https://doi.org/10.1021/acsomega.4c06728

Wu, Z., Duan, W., Lambertz, A., Qiu, D., Pomaska, M., Yao, Z., Rau, U., Zhang, L., Liu, Z., & Ding, K. (2021). Low-resistivity p-type a-Si: H/AZO hole contact in

high-efficiency silicon heterojunction solar cells. *Applied Surface Science*, *542*, 148749.

Yan, Y., Nashath, F. Z., Chen, S., Manickam, S., Lim, S. S., Zhao, H., Lester, E., Wu, T., & Pang, C. H. (2020). Synthesis of graphene: Potential carbon precursors and approaches. *9*(1), 1284-1314. https://doi.org/doi:10.1515/ntrev-2020-0100 (Nanotechnology Reviews)

Yang, N., Yu, S., Macpherson, J. V., Einaga, Y., Zhao, H., Zhao, G., Swain, G. M., & Jiang, X. (2019). Conductive diamond: synthesis, properties, and electrochemical applications. *Chemical Society Reviews*, *48*(1), 157-204.

Yang, Q., He, S., Huang, R., Yu, M., Chen, C., Zheng, S., Yun, D., Zheng, L., & Cheng, Q. (2021). Research on the fabrication and anti-reflection performance of diamond-like carbon films. *Diamond and Related Materials*, *111*, 108184. https://doi.org/https://doi.org/10.1016/j.diamond.2020.108184

Yang, Y., Zhang, H., & Yan, Y. (2019). Synthesis of CNTs on stainless steel microfibrous composite by CVD: Effect of synthesis condition on carbon nanotube growth and structure. *Composites Part B: Engineering*, *160*, 369-383. https://doi.org/https://doi.org/10.1016/j.compositesb.2018.12.100

Yap, S.-S., Yow, H.-K., & Tou, T.-Y. (2009). Amorphous carbon–silicon heterojunctions by pulsed Nd:YAG laser deposition. *Thin Solid Films*, *517*(18), 5569-5572. https://doi.org/https://doi.org/10.1016/j.tsf.2009.02.144

Yi, X.-W., Zhang, Z., Liao, Z.-W., Dong, X.-J., You, J.-Y., & Su, G. (2022). T-carbon: Experiments, properties, potential applications and derivatives. *Nano Today*, *42*, 101346. https://doi.org/https://doi.org/10.1016/j.nantod.2021.101346

Yuan, R., Guo, Y., Gurgan, I., Siddique, N., Li, Y.-S., Jang, S., Noh, G. A., & Kim, S. H. (2025). Raman spectroscopy analysis of disordered and amorphous carbon materials: A review of empirical correlations. *Carbon*, *238*, 120214. https://doi.org/https://doi.org/10.1016/j.carbon.2025.120214

Zhang, C. C., Hartlaub, S., Petrovic, I., & Yilmaz, B. (2022b). Raman Spectroscopy Characterization of Amorphous Coke Generated in Industrial Processes. *ACS Omega*, *7*(3), 2565-2570. https://doi.org/10.1021/acsomega.1c03456

Zhang, S., Li, Z., Luo, K., He, J., Gao, Y., Soldatov, A. V., Benavides, V., Shi, K., Nie, A., & Zhang, B. (2022a). Discovery of carbon-based strongest and hardest amorphous material. *National Science Review*, *9*(1), nwab140.

Zhang, W. (2013). Revealing the 1 nm/s Extensibility of Nanoscale Amorphous Carbon

in a Scanning Electron Microscope. *Scanning*. https://doi.org/10.1002/sca.21059

Zhao, Q., Liu, X., Cui, L., & Ma, C. (2024). Extraction and bioactivities of the chemical composition from Pleurotus ostreatus: a review. *Journal of Future Foods*, *4*(2), 111-118. https://doi.org/https://doi.org/10.1016/j.jfutfo.2023.06.001

Zhou, T., Hu, W., Yang, Z., Li, J., & Zeng, X. (2023). Study on nutrients, non-volatile compounds, volatile compounds and antioxidant capacity of oyster mushroom cultivated with corn distillers' grains. *LWT*, *183*, 114967. https://doi.org/https://doi.org/10.1016/j.lwt.2023.114967

Zhu, J., Li, F., Liu, G., Liu, D., Li, Q., & Kan, E. (2018). Synthesis of Amorphous Carbon Film in Ethanol Inverse Diffusion Flames. *Nanomaterials*, *8*(9), 656. https://www.mdpi.com/2079-4991/8/9/656

Zhu, R., Tao, Q., Lian, M., Feng, X., Liu, J., Ye, M., Wang, X., Dong, S., Cui, T., & Zhu, P. (2019). Modulating Band Gap of Boron Doping in Amorphous Carbon Nano-Film. *Materials*, *12*(11), 1780. https://www.mdpi.com/1996-1944/12/11/1780

Zhuo, C., Richter, H., & Levendis, Y. (2018). Carbon Nanotube Production From Ethylene in CO2/N2 Environments. *Journal of Energy Resources Technology*, *140*. https://doi.org/10.1115/1.4039328

Zobir, S., Zainal, Z., Sarijo, S., & Rusop, M. (2011). Properties of Amorphous Carbon Microspheres Synthesised by Palm Oil-CVD Method. *AIP Conference Proceedings*, *1328*. https://doi.org/10.1063/1.3573721

Zoroddu, M. A., Aaseth, J., Crisponi, G., Medici, S., Peana, M., & Nurchi, V. M. (2019). The essential metals for humans: a brief overview. *Journal of inorganic biochemistry*, *195*, 120-129.

AUTHOR'S PROFILE

Amirah Radhianie Binti Rining had completed her Master's in Electrical Engineering at the Faculty of Electrical Engineering, Universiti Teknologi MARA (UiTM). She graduated with a Bachelor of Science in Biotechnology at the Institute of Biological Sciences, Universiti Malaya, in 2023. She was a research assistant under the FRGS-funded project from 2023 to 2024.

LIST OF PUBLICATIONS

Academic Journal (Scopus)

Radhianie-Rining, A., Ahmad, N., Muhammad-Sukki, F., & Wan-Mohtar, W. A. A. Q. I. (2025). Optical and Electrical Properties of Amorphous Carbon Thin Films Grown from Mushroom Waste Oil using Chemical Vapor Deposition (CVD). *PaperASIA*, *41*(3b), 113-120. https://doi.org/10.59953/paperasia.v41i3b.414

Radhianie-Rining, A., Pirdaus, N. A., Abd, W., Qadr, A., Wan-Mohtar, I., Muhammad-Sukki, F., & Ahmad, N. (2026). Influence of Deposition Temperature on Amorphous Carbon Thin Films from Mushroom Waste Oil using Chemical Vapor Deposition (CVD). *PaperASIA*, *41*(6b), 668–675. https://doi.org/10.59953/paperasia.v41i6b.968